AN ABSTRACT OF THE THESIS OF

Julia F. Cohen for the degree of Master of Science in Geology presented on September 9, 2011.

Title: Compositional Variations in Hydrothermal White Mica and Chlorite from Wall-Rock Alteration at the Ann-Mason Porphyry Copper Deposit, Nevada

Abstract approved:

John H. Dilles

The detection of subtle variations in mineral chemistry in zoned hydrothermal alteration associated with the formation of porphyry copper deposits by short-wave infrared spectroscopy and rock chemistry are potentially valuable vectoring tools for mineral exploration. In order to correctly interpret the data collected by these methods, results must be calibrated by mineral data. Hydrothermal white mica, illite and chlorite grains were sampled from the Ann-Mason porphyry copper deposit in the Yerington district, Nevada, a Middle Jurassic porphyry copper system extended and tilted ~ 90° to the west. Mineral compositions vary spatially and record interactions with chemically distinct hydrothermal fluids over a vertical distance of ~5 km and a lateral distance of ~2 km from the ore center. Data suggest short wave infrared spectroscopy and bulk rock geochemical sampling can detect changes in mineral chemistry related to ore deposit formation but both methods have limitations.

To relate short wave infrared spectroscopy to mineral compositions, spectra from rock samples were measured. Characteristic features commonly used to identify white mica, illite and chlorite were compared to chemical compositions of mineral grains from 34 samples were determined by electron microprobe analysis. Results demonstrate short wave infrared spectroscopy can be used to detect changes in the aluminum content of micas using the wavelength of the 2200 nm feature and may be used to map fluid pH gradients in rocks with muscovite or illite-bearing assemblages. The following compositional characteristics of white mica/illite were observed in the short wave

infrared spectra: (1) an increase in the wavelength of the Al-OH absorption at ca. 2200 nm that is positively correlated with Fe+Mg+Mn (apfu) content and negatively correlated with total Al (apfu) corresponding to Tschermak substitution in both muscovite and illite, and (2) a decrease the wavelength of the ca. 2200 nm absorption to values below 2193 nm attributed to an increase in Na content (apfu) and the presence of paragonite intergrown with muscovite. For this sample set, illite cannot be distinguished from muscovite using short wave infrared spectroscopy. The proportion of Fe:Mg in the octahedral site in chlorite could not be identified in short wave infrared spectra of rocks using the wavelength of the 2350 nm feature and may have been obscured by coexisting highly reflective clays and micas.

To compare trace metal gradients in rocks and minerals, trace metal concentrations of more than 600 altered rock samples, collected in a broad geochemical sampling campaign, were measured using inductively coupled plasma-mass spectrometry and inductively coupled plasma-atomic emission spectroscopy. Trace element contents of rocks were compared to trace metal contents of hydrothermal white mica, illite and chlorite determined by laser ablation-inductively coupled plasma-mass spectrometry from a set of 34 samples. Results show Cu, Mo, Te, Se, Bi, Sb, As, W, Sn, Li and Tl are enriched in rocks from the zone of potassic, sericitic and shallow-level advanced argillic alteration that represents the near-vertical pathway of the ore fluid from the mineralized zone (3.5 km depth) to the near the paleosurface (< 0.5 km). Of these elements, W, Sn and Tl enrichment in rock can be attributed, at least partially, to increased concentrations in muscovite and illite. Lithium enrichment can be attributed to increased concentrations in chlorite and more mafic, chlorite-rich wall-rock lithology at less than 1 km depth. Zinc, Mn, Co and Ni are depleted in altered rock above the ore zone and redistributed upward and laterally by both the magmatic hydrothermal fluid and by circulating sedimentary brines as verified by gradients in chlorite compositions from propylitic alteration. Copper is detected in chlorites but at concentrations (average 280 ppm) too low to contribute significantly to the observed Cu anomaly in rock (>1000 ppm). Chalcophile elements Mo, As, Te, Se, Bi are rarely detected in white mica/illite or chlorite in concentrations greater than 1 ppm and, in more than 50% of analyses, levels are below detection.

Compositional Variations in Hydrothermal White Micas and Chlorite from Wall-Rock Alteration at the Ann-Mason Porphyry Copper Deposit, Nevada

by
Julia F. Cohen

A THESIS

submitted to

Oregon State University

in partial fulfillment of
the requirements for the
degree of

Master of Science

Presented September 9, 2011
Commencement June 2012

Master of Science thesis of Julia F. Cohen presented on September 9, 2011

APPROVED:

Major Professor, representing Geology

Chair of the Department of Geoscience

Dean of the Graduate School

I understand that my thesis will become part of the permanent collection of Oregon State University libraries. My signature below authorizes release of my thesis to any reader upon request.

Julia F. Cohen, Author

ACKNOWLEDGEMENTS

I would like to thank my advisor, Dr. John Dilles, for presenting me this research opportunity and for his support, and patience, in the lab and in the field. I have learned and grown exponentially as scientist under his guidance and, without him, this project would not have been possible. I would also like to thank my committee members Dr. Adam Kent and Dr. Richard Tosdal for their time and advice, and my graduate school representative Dr. Kevin Gable, for his time and effort and for volunteering to be a part of this process. In addition, I am grateful to Scott Halley for his help interpreting the spectral data and for his general feedback and advice.

I would like to thank the industry-sponsors of the Footprints of Porphyry Copper Deposits grant: Barrick Gold, Teck, Imperial Metals Corp, BHP Billiton, Vale and Freeport for their financial support. Additional financial support for this research was provided by the USGS MRERP Footprints of Porphyry Copper Deposits grant and an SEG student research grant.

I am thankful to Dr. Frank Tepley and Dale Burns for their help using the electron microprobe and to Dr. Adam Kent, Alison Koleszar and Matt Loewen for their help on the laser. I would like to thank Tatiana Alva at UBC for her collaboration on this project and for her assistance using the TerraSpec SWIR mineral analyzer.

I would like to thank Federico Cernuschi and Stephanie Grocke for reading drafts and giving feedback and, to all the VIPERs, for being such a great group of scientists and friends. I would like to give a special thanks to my parents, Chuck and Kathryn Cohen, for their love and encouragement and for acting as outside editors. Last but not least, I would like to thank Adam Billings, my fiancée and best friend, for taking a leap and following me on this adventure and, hopefully, on many more to come.

CONTRIBUTION OF AUTHORS

Dr. John Dilles, Dr. Richard Tosdal and Dr. Scott Halley collected and described the set of samples analyzed for rock chemistry presented in Chapter 2. Scott Halley wrote a preliminary report on the findings from this sampling effort that was the basis for the rock chemistry section in Chapter 2.

TABLE OF CONTENTS

TABLE OF CONTENTS (Continued)

TABLE OF CONTENTS (Continued)

LIST OF FIGURES

LIST OF FIGURES (Continued)

LIST OF FIGURES (Continued)

LIST OF TABLES

LIST OF APPENDICES

LIST OF APPENDIX FIGURES

LIST OF APPENDIX TABLES

Compositional Variations in Hydrothermal White Micas and Chlorite from Wall-Rock Alteration at the Ann-Mason Porphyry Copper Deposit, Nevada

Chapter 1: Introduction and Geologic setting of the Yerington district, Nevada

1.1 Introduction

Porphyry-type deposits contribute greatly to the global economy, primarily in the metals Cu, Mo, and Au (Seedorff et al., 2005). Due to extensive exploration and the rarity of these deposits, most well exposed porphyry-copper (Cu) deposits have been discovered. To find new deposits, exploration methods must be extended to regions with poor-exposure and to areas of rugged terrain. The motivation for this project and other related research (Alva, 2011) is to better understand the science behind large-scale exploration methods. This research provides data that exploration geologists could use to improve exploration methods in order to detect porphyry-Cu mineralization kilometers from an ore body using the mineralogy of wall-rock alteration as evidence for the pathway of ore-forming fluids. This thesis documents gradients in short wave infrared (SWIR) spectral data and trace element compositions of altered rocks and provides mineral data to improve understanding of these gradients.

This thesis focuses on variations in the major and trace element compositions of white mica (muscovite, mixed muscovite-paragonite and pyrophyllite), illite and chlorite from hydrothermal alteration surrounding the Ann-Mason porphyry-Cu(Mo) deposit at in the Yerington district, Nevada. Due to Miocene to present normal faulting, extension and tilting, the Middle Jurassic Yerington batholith and the Ann-Mason deposit have been exposed in cross-section from the paleosurface to approximately 7 km depth (Proffett, 1977). The resulting exposures provide an ideal location to study the spatial distribution of trace elements and phyllosilicate chemistry surrounding a porphyry-Cu system. In addition, the petrology of the Yerington batholith (Dilles, 1987) and the nature of wall-rock alteration at the Ann-Mason deposit (Carten, 1986; Dilles and Einaudi, 1992; Lipske, 2002) have been studied in detail and a model for the origin and sequence of observed alteration assemblages has been developed based on field mapping, petrology, fluid inclusion data and stable isotopes (Dilles et al., 2000a).

The content of this thesis is divided into four chapters: (1) introduction and geologic setting of the Yerington district, Nevada, (2) comparison of short-wave infrared spectra to white micas, illite and chlorite compositions from hydrothermal alteration at the Ann-Mason porphyry copper deposit, Nevada, (3) trace metal zonation at the Ann-Mason porphyry copper deposit, Nevada and (4) conclusion.

1.2 Geologic setting of the Yerington district, Nevada

1.2.1 Location

The Yerington district and the town of Yerington are located in western-central Nevada, approx. 80 miles to the southeast of Reno, Nevada (Figure 1.1). The Yerington district lies in the western Great Basin portion of the Basin and Range province, which extends from the Sierra Nevada east to the Columbia Plateau and south from southern Idaho to northern Arizona Within the Yerington district is the Yerington batholith, a Middle Jurassic pluton that hosts at least four porphyry copper deposits, including Ann-Mason, and is associated with nearby copper skarn and iron oxide-copper-gold mineralization (Dilles and Proffett, 1995).

1.2.2 Geologic history

The oldest rocks that outcrop in the Yerington district are the Middle to early Late Triassic McConnell Canyon volcanics, a group of calc-alkaline andesites and rhyolites. These are overlain by a Late Triassic to Middle Jurassic regressive sedimentary sequence of carbonates, volcanoclastics and argillites with uppermost units of evaporite gypsum and eolian quartzite (Dilles and Wright, 1988). Arc magmatism developed along the edge of the continent in the Middle Jurassic (165 – 170 Ma), leading to the deposition of the Artesia Lake volcanics and virtually simultaneous emplacement of the Yerington batholith (168 – 169 Ma). The Fulstone Spring volcanics (167 Ma), overlie the Artesia Lake volcanics and are intruded by the later Shamrock batholith (165 – 166 Ma) (Dilles, 1987; Dilles and Wright, 1988; Proffett and Dilles, 1984; Proffett and Dilles, 2005). Additional research regarding the Mesozoic geology is reported in Dilles (1987) and Dilles and Wright (1988).

A major erosional unconformity separates the Mesozoic arc-related volcanic, sedimentary and intrusive rocks from the overlying Tertiary, Oligocene and Miocene, volcanics and intrusives (Proffett and Dilles, 1984). The Tertiary deposits are uncomfortably overlain by Quaternary alluvium and landside sediments, which are the youngest deposits in the region (Proffett and Dilles, 1984). Detailed description of the Cenozoic units and structure can be found in Proffett and Proffett (1976), Proffett (1977) and Dilles and Gans (1995).

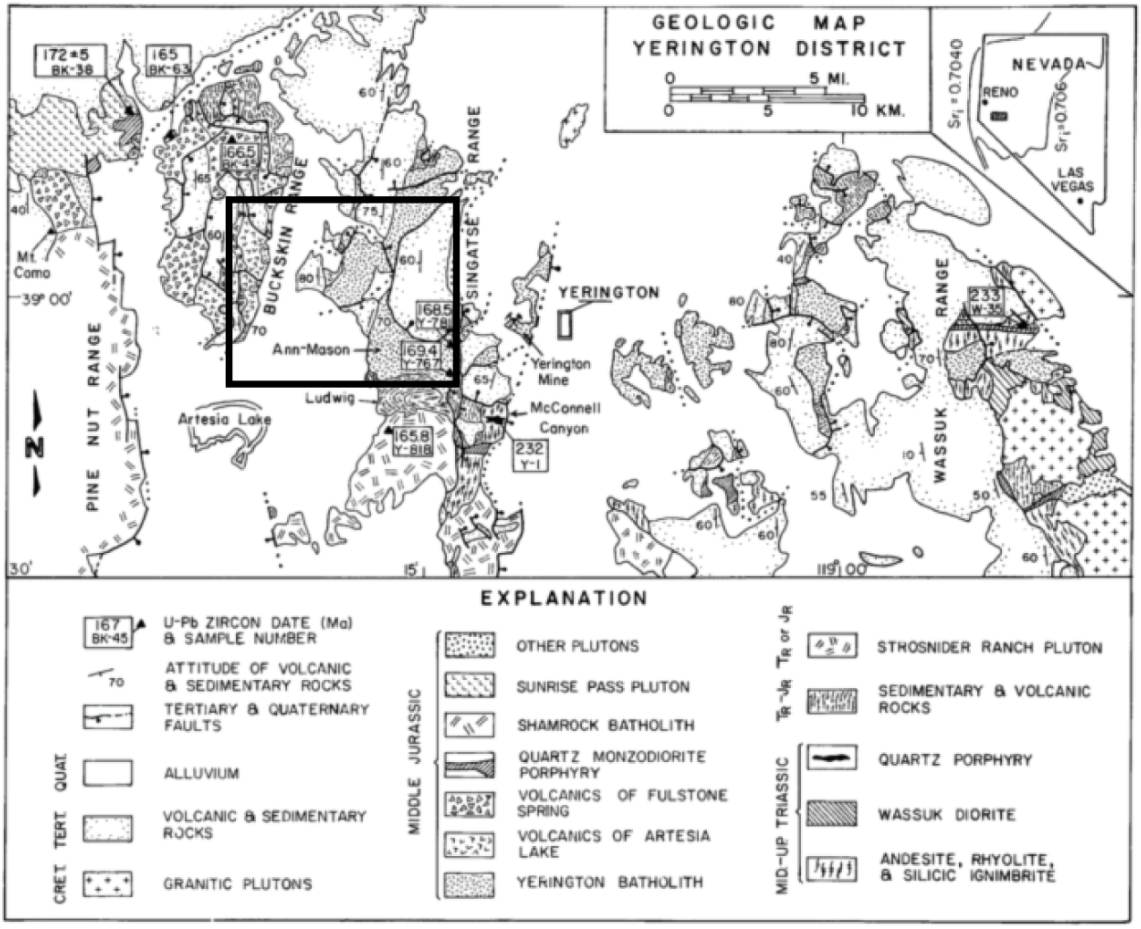

Figure 1.1. Location and simplified geologic map of the Yerington district, Nevada. (from Dilles and Wright, 1988, based on Proffett and Dilles, 1984). Black rectangle outlines study area.

1.2.3 Structure

The Yerington district underwent significant tilting as a result of Basin and Range extension along steeply dipping normal faults, beginning in the Miocene and continuing through the present. Movement along faults accommodated more than 100 percent east-west extension and tilted fault blocks 60-90° W (Proffett, 1977; Proffett and Dilles, 1984). As a result, a structural cross section through the Yerington batholith and overlying volcanics is preserved and exposed from the surface to 1 km paleodepth in the more westerly Buckskin Range and from 1 to 7 km paleodepth in the more easterly Singatse Range. The structural history of the region is documented in Proffett (1977) and geologic map of the region has been published in Proffett and Dilles (1984).

1.2.4 Rock units

Two major units host the majority of the hydrothermal alteration associated with the formation of the Ann-Mason porphyry-Cu(Mo) deposit, the Yerington batholith and the overlying Artesia Lake volcanics. The Yerington batholith is a shallowly emplaced (top at <1 km) composite pluton with three main intrusive units whose volumes decrease and lithologies become more silicic with time. Details regarding the petrology of the Yerington batholith are published in Dilles (1987). All the intrusive lithologies have alkali-calcic chemistry and consist of the same general group of minerals: plagioclase, K-feldspar, quartz, hornblende, biotite, magnetite, sphene, apatite and zircon in varying proportions. Lithologies include the early McLeod Hill hornblende quartz monzodiorite, which is intruded by the Bear pluton, a compositionally zoned intrusion from hornblende quartz monzonite to a border of granite. The Luhr Hill porphyritic granite intrudes the older units of the batholith and, at the Ann-Mason deposit, forms a cupola at approximately 3.5 km beneath the paleosurface (Dilles and Einaudi, 1992). A granite porphyry dike swarm centered on the cupola extends upward toward the paleosurface. The ore zone at Ann-Mason is positioned on the dike swarm at the top of the cupola. Hydrothermal alteration is also focused along the dikes which act as permeable zones for fluid flow (Dilles, 1987).

The Yerington batholith directly intrudes the overlying Artesia Lake volcanics, an approximately 1 km thick group of andesite, dacite and minor basalt flows, breccias, rhyolite tuffs, tuffaceous sediments and shallow intrusions, which are similar in composition and age to the batholith and likely cogenetic (Dilles, 1987; Lipske and Dilles, 2000). The Artesia Lake volcanics are overlain by the Fulstone Spring volcanics, a subaerial volcanic sequence consisting of latitic to dacitic lava flows and rhyolitic to dacitic ignimbrites and breccias, which outcrop in the Buckskin Range. Deposition of the Fulstone Spring volcanics postdates the period of pervasive hydrothermal alteration associated with the emplacement of the Yerington batholith but these rocks are weakly altered principally to a feldspar-stable sericite-hematite-chlorite assemblage typical of propylitic alteration in Buckskin Range and likely formed by late low temperature sedimentary brines (Lipske, 2002).

1.2.5 Model for observed sequence of hydrothermal alteration and mineralization

In the Yerington district and at the Ann-Mason deposit there is evidence for two main types of coexisting hydrothermal fluids, one with magmatic origin and one derived from formation waters trapped within the Triassic-Jurassic sedimentary sequence intruded by the Yerington batholith. Wall-rock alteration in the Ann-Mason fault block is described in detail in Dilles and Einaudi (1992). A summary of and model for the observed sequence of alteration and mineralization in the Yerington district is proposed in Dilles et al. (2000) and summarized below.

Magmatic hydrothermal fluids, formed during the crystallization of the Luhr Hill granite, are responsible for the deposition of the Ann-Mason Cu(Mo) sulfide deposit and potassic, sericitic and advanced argillic alteration in the overlying intrusive and volcanic units. The Luhr granite was water-rich (5 wt. %) and strongly oxidized (NNO buffer + 2 to 3 log units) with abundant sulfate (>1000 ppm) and reached water saturation at approximately 50% crystallization according to petrologic evidence (Dilles, 1987; Dilles and Proffett, 1995; Streck and Dilles, 1998). The resultant magmatic fluid phase, containing abundant Cl, K, Na, Fe, S and Cu (Dilles and Proffett, 1995), was released along with porphyry dikes due to or overpressuring and tectonic fracturing of the overlying wall rock. Based on the orientation of the dikes, position of the ore body, and

distribution of related hydrothermal alteration, the ore-forming fluid traveled along a near vertical path toward the paleosurface (Dilles et al., 2000).

Potassic, sericitic and advanced argillic alteration types were formed by interactions between wall rock and fluids with a magmatic component based on mineral assemblages, fluid inclusions, stable isotope data. Near the origin, these fluids were high salinity (30-60 wt % NaCl equivalent) and high water to rock ratios and temperatures (<400 - 700° C) resulted in potassic alteration (biotite±K-feldspar) and mineralization (bornite±chalcopyrite±magnetite) focused along the central dike swarm (Dilles and Einaudi, 1992).

Advanced argillic alteration (pyrophyllite-quartz-alunite-pyrite) formed contemporaneously with potassic alteration near the paleosurface and predates some episodes of sericitic alteration as indicated by cross-cutting relationships (Lipske, 2002). Advanced argillic alteration could be a result of low-density vapor phase that separated from the early high temperature magmatic brine due to depressurization of the fluid phase and brine-vapor immiscibility during ascent (Bodnar et al, 1985). Alternatively, the magmatic fluid phase may not have separated and, instead, ascended as a volatile-rich fluid phase toward the paleosurface. This vapor or low-density fluid phase mixed with local ground water to form low temperature, high K^+/H^+ fluids responsible for the observed advanced argillic assemblages (Lipske, 2002).

Sericitic alteration forms as selvages on quartz-pyrite±chalcopyrite D-veins (Gustafson and Hunt, 1975) and ranges in intensity from proximal pervasive quartz-muscovite-pyrite±chalcopyrite assemblage (strong sericitic alteration) laterally to feldspar stable chlorite-muscovite±pyrite±hematite assemblage (sericitic-chloritic alteration) (Dilles and Einaudi, 1992). Sericitic alteration forms a funnel-shaped halo extending from the top of the batholith cupola toward the paleosurface along the axis of the granite porphyry dike swarm and cuts potassic alteration in and above the ore zone, indicating some episodes must postdate potassic alteration and ore deposition. Data from oxygen, hydrogen and sulfur isotopes indicate the formation fluid for sericitic alteration is about half magmatically-derived and sulfides (pyrite±chalcopyrite) have a magmatic source (Dilles et al., 1992; Streck and Dilles, 1998). In the model by Dilles et al. (2000), sericitic alteration may have initially formed in an intermediate position between potassic

and advanced argillic alteration and become more pervasive as the Luhr Hill granite crystallized and cooled producing lower temperature fluids which did not cross the brine-vapor immiscibility field. These fluids mixed with groundwater to form low salinity, low temperature fluids with high K^+/H^+ ratios as seen in fluid inclusions (Dilles and Einaudi, 1992).

Abundant sodic-calcic alteration in the Yerington district is characterized by the conversion of K-feldspar to oligoclase, albite or local epidote and the addition of actinolite, epidote and sphene. Numerous studies suggest this alteration was caused by a high salinity (30 – 40 wt % NaCl equivalent), moderate temperature (250 to 400° C), fluid derived from trapped pore waters within the sedimentary section (Carten, 1987; Dilles and Einaudi, 1992). The Yerington batholith intruded a Triassic-Jurassic regressive sedimentary sequence with an evaporate layer that would have contained large volumes of high salinity pore fluids (Dilles et al., 2000). These fluids were heated by the intrusion and traveled from the contact aureole at 2 - 6 km paleodepth, through the batholith laterally for several kilometers and then upward outside the main flow path of the magmatic plume. As the magmatic fluids waned, non-magmatic fluids moved inward and, in many places, superimposed sodic-calcic alteration atop magmatic hydrothermal alteration. This cycle repeated at least five times as recorded by geologists in the Yerington mine (Proffett, 1979). In the late stages, the non-magmatic fluids cooled or mixed with a small proportion of magmatic fluid to cause sodic alteration (albite-chlorite±sericite) that overprints the ore zone and occurs with sericitic alteration at intermediate depths (1-3 km) (Dilles and Einaudi, 1992; Dilles et al., 2000).

Propylitic alteration (actinolite-epidote-chlorite), caused by lower temperature (~300° C) circulating sedimentary brines, is found near the periphery of the system at intermediate depths <1 to 4 km (Dilles et al., 2000). Chloritic alteration characterized by the addition of chlorite, hematite, K-feldspar and magnetite with relict feldspar may also be attributed to the sedimentary brines. This alteration is associated with Fe-oxide-Cu-Au mineralization and is common in the Buckskin Range where is cuts earlier sericitic and advanced argillic alteration (Lipske, 2002).

1.2.6 Summary

In summary, the Yerington district in western Nevada contains several porphyry centers including the Ann-Mason porphyry Cu(Mo) deposit, Cu skarn deposits and Fe-oxide-Cu-Au vein and lode deposits associated with the emplacement of the Yerington batholith. Miocene to present day faulting and extension has exposed the batholith system from paleosurface to ~ 7 km paleodepth and tilted the section ~90° W. The resulting exposures provide an ideal location to study the spatial distribution of trace elements and phyllosilicate chemistry surrounding a porphyry-copper system. Alteration in the district can be attributed to two fluids of different origins: (1) a magmatic fluid phase responsible for Cu(Mo) sulfide mineralization that decreases in temperature and salinity over time forming a vertical zone of potassic, sericitic alteration and shallow advanced argillic alteration and (2) a circulating saline brine derived from trapped formation waters that caused for sodic-calcic, propylitic, sodic and chloritic alteration and Fe-oxide-Cu-Au deposits.

1.3 References

Alva, T. R., 2011, Variations in hydrothermal muscovite and chlorite composition in the Highland Valley porphyry Cu-Mo district, British Columbia, Canada [M.S.: University of British Columbia, Canada].

Bodnar, R. J., Burnham, C. W., and Sterner, S. M., 1985, Synthetic fluid inclusions in natural quartz. III Determination of phase equilibrium properties in the system H2O-NaCl to 1000 C AND 1500 bars: Geochimica et Cosmochimica Acta, v. 49, p. 1871-1873.

Carten, R., 1986, Sodium-calcium metasomatism; chemical, temporal, and spatial relationships at the Yerington, Nevada, porphyry copper deposit: Economic Geology, v. 81, no. 6, p. 1495.

Dilles, J. H., 2005, Isotopic evidence for the multiple ources of lead in porphyry Cu-Mo and base metal lode ores at Butte, Montana: Abstracts with Programs, Geological Society of America, v. 37, p. 315.

Dilles, J. H., and Einaudi, M., 1992, Wall-rock alteration and hydrothermal flow paths about the Ann-Mason porphyry copper deposit, Nevada; a 6-km vertical reconstruction: Economic Geology, v. 87, no. 8, p. 1963.

Dilles, J. H., and Proffett, J. M., 1995, Metallogenesis of the Yerington Batholith, Nevada: Arizona Geological Society Digest, v. 20, p. 306-315.

Dilles, J. H., Solomon, G., Taylor, H., and Einaudi, M., 1992, Oxygen and hydrogen isotope characteristics of hydrothermal alteration at the Ann-Mason porphyry copper deposit, Yerington, Nevada: Economic Geology, v. 87, no. 1, p. 44.

Dilles, J. H., Einaudi, M. T., Proffett, J. M., and Barton, M. D., 2000, Overview of the Yerington porphyry copper district: magmatic and non-magmatic sources of hydrothermal fluids, their flow paths, alteration affects on rocks, and Cu-Mo-Fe-Au ores: Society of Economic Geologist Guidebook Series, v. 32, p. 55-66.

Dilles, J. H., 1987, Petrology of the Yerington Batholith, Nevada; evidence for evolution of porphyry copper ore fluids: Economic Geology, v. 82, no. 7, p. 1750.

Dilles, J. H., and Gans, P. B., 1995, The chronology of Cenozoic volcanism and deformation in the Yerington area, western Basin and Range and Walker Lane: Geological Society of America Bulletin, v. 107, no. 4, p. 474-486.

Dilles, J. H., and Wright, J. E., 1988, The chronology of early Mesozoic arc magmatism in the Yerington District of western Nevada and its regional implications: Geological Society of America Bulletin, v. 100, no. 5, p. 644-652.

Gustafson, L., and Hunt, J., 1975, The porphyry copper deposit at El Salvador, Chile: Economic Geology, v. 70, no. 5, p. 857.

Lipske, J., and Dilles, J., 2000, Advanced argillic and sericitic alteration in the subvolcanic environment of Yerington Porphyry Copper System, Buckskin Range, Nevada: Part I. Contrasting Styles of Intrusion-Associated Hydrothermal Systems, v. 32, p. 91-99.

Lipske, J., 2002, Advanced argillic and sericitic alteration in the Buckskin Range, Nevada: a product of ascending magmatic fluids from the deeper yerington porphyry copper environment [M.S.: Oregon State University].

Proffett, J. M., 1977, Cenozoic geology of the Yerington District, Nevada, and implications for nature and origin of Basin and Range faulting: Geological Society of America Bulletin, v. 88, no. 2, p. 247-266.

-, 1979, Ore deposits of the western United States: a summary: Nevada Bureau of Mines, IAGOD 5th Quadrennial Symposium, Geology Report 33, Proceedings, v. 11, p. 13-32.

Proffett, J. M., and Dilles, J. D., 1984, Geologic map of the Yerington District, Nevada, Nevada Bureau of Mines and Geology.

Proffett, J. M., and Proffett, B. H., 1976, Stratigraphy of the Tertiary ash-flow tuffs in te Yerington Dictrict, Nevada: Nevada Bureau of Mines and Geology, Report, no. 27.

Seedorff, E., Dilles, J. H., Proffett, J. M., Jr., Einaudi, M. T., Zurcher, L., Stavast, W. J. A., Johnson, D. A., and Barton, M. D., 2005, Porphyry deposits; characteristics and origin of hypogene features: Economic Geology 100th Anniversary Volume, p. 251-298.

Streck, M., and Dilles, J., 1998, Sulfur evolution of oxidized arc magmas as recorded in apatite from a porphyry copper batholith: Geology, v. 26, no. 6, p. 523-526.

Chapter 2: Comparison of short-wave infrared spectra to white mica, illite and chlorite compositions from hydrothermal alteration at the Ann-Mason porphyry copper deposit, Nevada

2.1 Abstract

The detection of subtle compositional variations within hydrothermal phyllosilicates from zoned alteration associated with the formation of porphyry-type ore deposits by short wave infrared spectroscopy may be a valuable vectoring tool for mineral exploration. Short wave infrared spectra from rock samples were compared with chemical compositions of mineral grains determined by electron microprobe analysis in order to correlate spectral characteristics with variations in mineral composition. These results demonstrate SWIR spectroscopy can be used to detect changes in the phengitic component of micas using the wavelength of the ca. 2200 nm feature and may be used to map fluid pH gradients in rocks with muscovite or illite-bearing assemblages.

Muscovite, illite, paragonite, pyrophyllite and chlorite grains from thirty-four rock samples were selected from hydrothermal wall-rock alteration representing the near-vertical pathway of magmatic hydrothermal fluids from paleosurface to ~3.5 km depth. Hydrothermal alteration types sampled range from advanced argillic, to sericitic (muscovite, muscovite-chlorite±feldspar, muscovite±illite-feldspar), illitic, illitic-chloritic, and propylitic (chlorite-epidote-actinolite) associated with the formation of the Ann-Mason porphyry Cu(Mo) deposit in the Yerington district, Nevada. The following compositional characteristics determined by electron microprobe analysis for white mica/illite were observed in the short wave infrared spectra: (1) an increase in the wavelength of the Al-OH absorption at ca. 2200 nm that is positively correlated with Fe+Mg+Mn content corresponding to Tschermak substitution in both muscovite and illite, and (2) a decrease the wavelength of the ca. 2200 nm absorption to values below 2193 nm attributed to an increase in Na concentration from paragonitic substitution in muscovite. For this sample set, illite cannot be distinguished from muscovite using short wave infrared spectroscopy. Chlorite compositional variations could not be identified in short wave infrared spectra of rocks and were likely obscured by coexisting highly reflective clays and micas.

2.2 Introduction

This study measures major element compositions of muscovite, illite, intergrown muscovite and paragonite, pyrophyllite and chlorite from the hydrothermal alteration surrounding the Ann-Mason porphyry copper deposit in the Yerington district, Nevada. Compositional variations are compared to corresponding short wave infrared (SWIR) spectra to determine if SWIR spectroscopy can be used to map compositional variations in hydrothermal white mica and chlorite. An increase in the wavelength of the Al-OH absorption band at ca. 2200 nm in muscovite and illite has been attributed to the Tschermak substitution [$(Al^{3+})^{vi} + (Al^{3+})^{iv}$ <-> $(Fe^{2+}$ or $Mg^{2+})^{vi} + (Si^{4+})^{iv}$] and a decrease in the wavelength of the Al-OH absorption band to values below 2193 nm is caused by the presence of paragonite (Duke, 1994). Illite has been previously identified (Hauff et al., 1989) by a deep H_2O absorption at ~1900 nm. Previous researchers (e.g. Duke, 1994; Yang et al., 2000) have suggested that geologists may use SWIR spectroscopy to identify zoned hydrothermal alteration, which, in combination with other exploration techniques, can be used as a vector for ore deposit exploration. This study tests this hypothesis using samples from wall-rock alteration surrounding the Ann-Mason porphyry-Cu deposit at Yerington, Nevada.

2.2.1 Background

Hydrothermal alteration associated with the formation of porphyry-type ore deposits is spatially and temporally zoned with respect to the ore body. Numerous studies have documented the geochemical and mineralogical features of these zones and noted their importance as both indicators of the physicochemical environment of formation and potential vectors for ore exploration (Dilles and Einaudi, 1992; Gustafson and Hunt, 1975; Lowell and Guilbert, 1970; Meyer and Hemley, 1967; Rose, 1970). Hydrothermal phyllosilicates such as muscovite, illite and chlorite are essential minerals for identifying and understanding many key alteration zones. Since the stability of individual minerals and mineral assemblages is based on physiochemical parameters, such as rock and fluid composition, temperature, pressure, and pH, the presence and composition of phyllosilicate and clay species in hydrothermal mineral assemblages can be used to hypothesize boundary conditions of formation.

Identifying hydrothermal white mica and clay species in hand sample using common field tools, such as a hand lens, is extremely difficult. The term "sericite" is commonly used as field term to refer to fine-grained white mica minerals (Meyer and Hemley, 1967). Since most field studies cannot identify individual species. Although the chlorite group of minerals can commonly be identified by hand lens, specific chlorite compositional end-members that might distinguish alteration types are difficult to determine by common field methods.

Short-wave infrared (SWIR) spectroscopy is used to record the infrared absorption spectrum that corresponds to cation-OH and H_2O bond energies characteristic of mineral structures. The spectra can be used to identify hydrous minerals, including white mica and chlorite (Thompson et al., 1999). The development of portable SWIR spectrometers has made field mapping of white mica, clay and chlorite species inexpensive and efficient. This has led to renewed interest in the phyllosilicate and clay minerals as indicator minerals for alteration zones.

Infrared (IR) spectroscopy was developed in the early 1950's when commercial spectrometers became available. The importance of the technique in identifying the energies/wavelengths of the OH fundamental modes of vibration was apparent early on and significant research was dedicated to understanding the crystalline structure and cationic composition of phyllosilicates (Serratosa and Bradley, 1958; Stubican and Rustum, 1961; Tuddenham and Lyon, 1960). In 1963, Vedder and McDonald identified the combination OH stretch and OH in-plane bend absorption band in phyllosilicates occurring near 2200 nm. Later, Vedder (1964) related this combination band to the Al-OH bond. This band is significant to remote sensing because it lies in the SWIR (1300 – 2500 nm) portion of the electromagnetic spectrum not absorbed by atmospheric gases and, therefore, useful in remote sensing and field applications (Martinez-Alonso, 2000).

Several authors recognized the importance of IR spectroscopy in the identification of alteration related to ore deposits (Hunt and Ashley, 1979). A pioneering study by Swayze (1997) demonstrated IR spectral data, including the location of the ca. 2200 nm band, could be used to detect compositional variations in muscovite in alteration at Cuprite, Nevada. Post and Noble (1993), in a study comparing near infrared (NIR) spectra of micas to x-ray florescence (XRF) analyses of muscovite, saw a direct

correlation between Al_2O_3 (wt %) in muscovite and the position of the ca. 2200 absorption band. Duke (1994) confirmed the increase in the wavelength of the 2200 nm feature correlated with the Fe+Mg (apfu) component in muscovite using electron microprobe analyses (EMPA) and recognized the potential importance of SWIR spectrometry in mapping the Tschermak substitution in metamorphic terrains. The Tschermak substitution is the coupled substitution in the octahedral (vi) site of Al^{3+} by Fe^{2+} and/or Mg^{2+}, and in the tetrahedral (iv) site, of Al^{3+} by Si^{4+}. First described in chlorite (Tschermak, 1890, 1891), it has since been recognized in muscovite/illite, biotite, amphibole, talc and clinopyroxene (Deer et al., 1993).

The development of the portable SWIR spectrometer provided a tool for identifying variations in hydrous mineral compositions in the field and its potential for mapping alteration was quickly recognized (Merry and Pontual, 1999; Pontual et al., 1995). Portable SWIR spectrometers have been used to help define alteration zones in a variety of ore deposit environments (Hauff, 2002; Herrmann et al., 2001; Herrmann et al., 2009; Jones et al., 2005; Lipske, 2002; Lipske and Dilles, 2000; Sun et al., 2001; Yang et al., 2001). Although SWIR spectroscopy has been used to study alteration related to epithermal, Carlin-type gold and volcanogenic massive sulfide deposits, alteration related to porphyry-type deposits has been sparsely studied (Changyun et al., 2005; Di Tommaso and Rubinstein, 2007).

Most of studies where SWIR spectroscopy is used to identify hydrothermal minerals and alteration zones related to ore deposits have calibrated their results with x-ray diffraction (XRD) or x-ray fluorescence (XRF) (Martinez-Alonso, 2000; Sun et al., 2001). Both of these methods require monomineralic separates, which are difficult to obtain from samples with fine-grained white micas mixed with quartz. In addition, XRD does not determine quantitative mineral compositions but measures the D-spacing to define the crystal structure. In order to derive mineral compositions, D-spacing values must be independently calibrated to chemical composition. These methods are less reliable in mineral identification than electron microprobe analysis (EMPA). Alternatively, EMPA determines quantitative chemical composition of minerals in situ and is a commonly used and well-calibrated method.

2.2.2 Study area

The region surrounding the Ann-Mason deposit in the Yerington district, Nevada, was chosen as a field site for this study. At Yerington, a middle Jurassic batholith hosting several porphyry copper centers has been tilted ~ 90° to the west by Basin and Range extension exposing a crustal cross section from ~ 1 - 7 km paleodepth (Proffett, 1977a; Proffett and Dilles, 1984). The Ann-Mason porphyry copper system at Yerington, NV has good exposure from ~1 – 6 km paleodepth and has been well-studied (see Chap. 1), ideal for detailed research.

The oldest rocks that outcrop in the Ann-Mason fault block, Blue Hill fault block and Buckskin Range portions of the Yerington district are Middle to Early Late Triassic calc-alkaline andesites and rhyolites of the McConnell Canyon volcanics. These are overlain by a sedimentary sequence of carbonates, volcanoclastics, and argillites with uppermost units of evaporate gypsum and eolian quartzite deposited during the Late Triassic to Early Jurassic (Dilles and Wright, 1988). Arc magmatism developed along the edge of the continent in the Middle Jurassic (165 – 170 Ma) leading to the deposition of the Artesia Lake volcanics and virtually simultaneous emplacement of the Yerington batholith (168 – 169 Ma) and the subsequent deposition of the Fulstone volcanics (167 Ma) and the intrusion of the Shamrock batholith (165 – 166 Ma) (Dilles and Wright, 1988). A major unconformity separates the Mesozoic arc-related volcanics and the younger sedimentary and intrusive rocks from the Tertiary, Oligocene and Miocene (Proffett and Dilles, 1984). Detailed description regarding the Cenozoic units and structure can be found in Proffett (1977) and (Dilles and Gans, 1995). The Tertiary deposits are uncomfortably overlain by Quaternary alluvium and landside sediments, the youngest deposits in the region (Proffett and Dilles, 1984).

The lithologies sampled for this study include all phases of the Yerington batholith and several samples from the Artesia volcanics. The Yerington batholith is a composite pluton with three main intrusive lithologies whose volumes decrease, grain-sizes increase, and compositions become more siliceous with time. These units include the McLeod Hill quartz monzodiorite (oldest), to the Bear quartz monzonite, to the Luhr Hill granite (youngest) (Dilles, 1987). Sampling focused on the granite porphyry dikes, associated with ore deposition, that originate at ~3 – 6 km paleodepth and stem upward

from the Luhr Hill granite intrusion. The mineralogy [plag-Ksp-qtz-biot-hbl-(mgt)-(sph)] is similar in all units although the proportions, textures and grain sizes vary (Dilles, 1987). The Artesia Lake volcanics is a series of andesitic lava flows, ignimbrites, breccias, and sandstones thought to be the cogenetic extrusive equivalent of the Yerington batholith due to chemical, isotopic and hydrothermal alteration evidence (Dilles,1987; Dilles and Wright, 1988). These rocks are commonly altered to pyrophyllite or muscovite, alunite, quartz-rich assemblages that once contained abundant pyrite, suggested by limonite minerals and boxwork structures on weathered surfaces. Primary textures in these rocks have been mostly obliterated by alteration in northern Blue Hill and central Buckskin Range exposures (Lipske, 2002).

Table 2.1. Mineral abbreviations

Ab	albite	Dick	dickite	Olg	oligoclase
Act	actinolite	Ep	epidote	Py	pyrite
Alun	alunite	Fsp	feldspar	Pyroph	pyrophyllite
Ans	andesine	Hem	hematite	Rt	rutile
And	andalusite	Ill	illite	Smec	smectite
Ba	barite	Kaol	kaolinite	Ser	sericite
Biot	biotite	Ksp	potassium feldspar	Sph	sphene
Calc	calcite	Mgt	magnetite	Tp	topaz
Chl	chlorite	Musc	muscovite		

2.3 Methods

2.3.1 Geologic mapping and sampling

Thirty-four surface samples and five drill core samples were selected for analysis from the Yerington District, Nevada. Sample locations are shown in Figure 2.1 and a table of sample coordinates, lithologies and mineral assemblages is available in Appendix A. Mineral abbreviations are given in Table 2.1. Sample selection focused on the Blue Hill fault block where the portion of the hydrothermal system from directly above the Ann-Mason porphyry copper ore body upward to the subvolcanic environment is exposed (~3.5 – 0.5 km paleodepth). A wide variety of alteration types and assemblages are found in this region and include “D” veins (Gustafson and Hunt, 1975) with 1 cm to 1 m wide sericitic (quartz-muscovite to muscovite-feldspar) selvages, chlorite-muscovite-

hematite alteration and alteration with advanced argillic index minerals, such as pyrophyllite and alunite, associated with the upper portions of the system. The northern region of the Blue Hill fault block and the southwestern part of the Ann-Mason fault block have abundant propylitic (actinolite-epidote-chlorite) and sodic-calcic (albite-actinolite-epidote) alteration formed by circulating saline brines of sedimentary origin (Dilles and Einaudi, 1992).

Trenches were mapped in the Blue Hill fault block to document spatial and temporal relationships in hydrothermal alteration and mineralization and record the orientation of veins, contacts and faults. Trench mapping in the Blue Hill fault block was done by Anaconda method (Einaudi, 1977) at approximately 1:500 scale. Selected trenches were positioned along an E-W traverse along the strike of several porphyry dikes in the center of the main dike swarm in the Blue Hill fault block. This traverse was selected to record variations in alteration, veins and mineralization moving vertically east to west through the Ann-Mason porphyry copper system. Trenches were oriented approximately perpendicular to dikes, veins and other structures (approx. N30°E). A digitalized example of trench mapping is available in Appendix C. Hydrothermal alteration, mineralization and veins were mapped on a large scale (1:4,800) at Ann-Mason (Dilles and Einaudi, 1992), the Blue Hill fault block (1:12,000, J.H. Dilles, unpub.) and Buckskin Range by Lipske (2002) (1:4,800) using the Anaconda method.

2.3.2 Petrography

Twenty-seven polished thin sections (30 – 100 μm thick) and eight chip samples in resin mounts were examined using an Olympus BX-60 petrographic microscope to document mineralogy and alteration assemblages. Photomicrographs of alteration assemblages and textures were taken using a microscope-mounted Nixon digital camera (DXM1200) and ACT-1 image software.

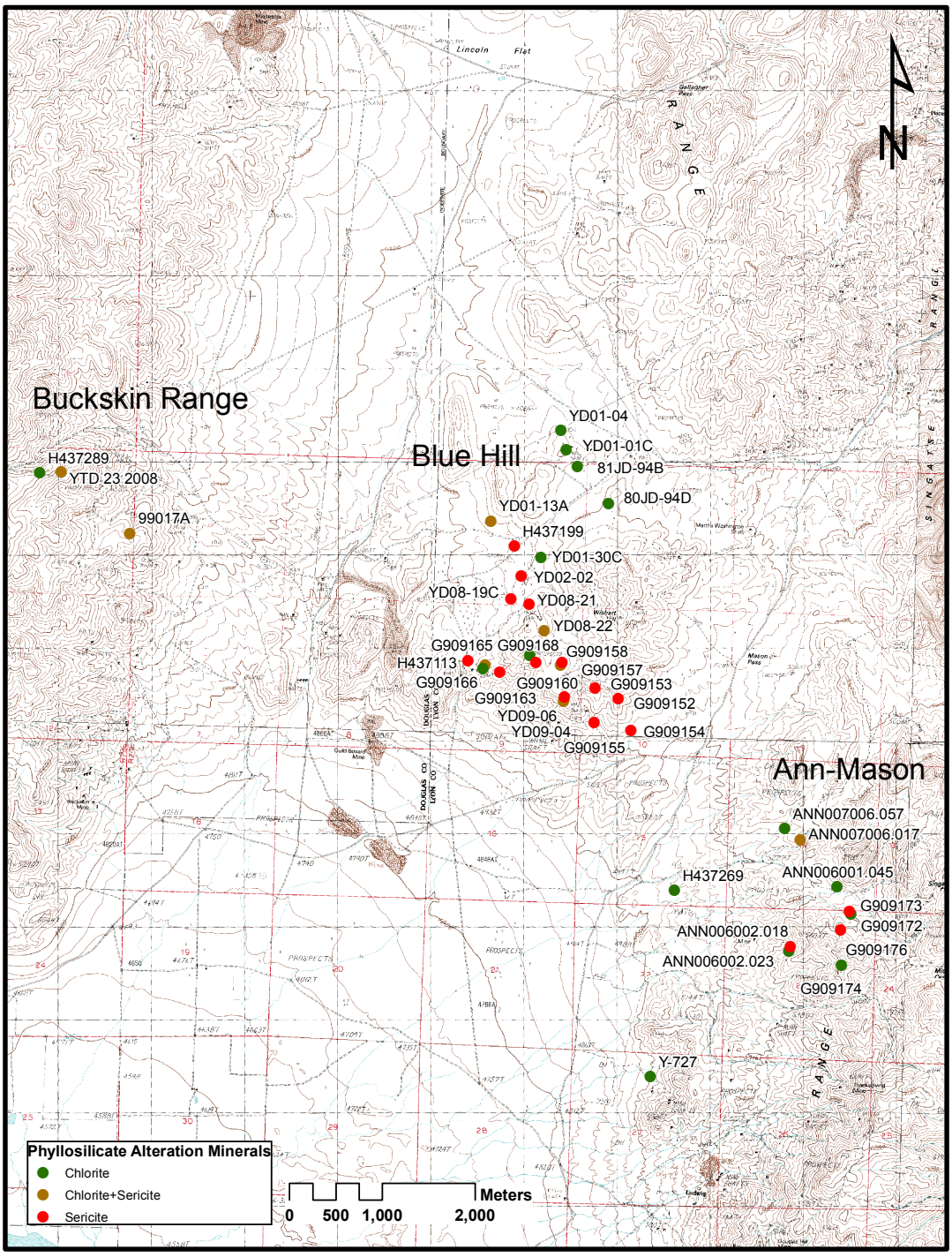

Figure 2.1. Sample location map. Colors represent the combination of phyllosilicate alteration minerals from each sample. Thirty-four samples were collected for mineral analyses. General regions (Buckskin Range, Blue Hill fault block and Ann-Mason fault block) are labeled.

2.3.3 Electron microprobe analysis

Major element compositions of muscovite, illite, paragonite, pyrophyllite and chlorite from a suite of 35 samples were collected using a CAMECA SX-100 electron microprobe at Oregon State University. Analyses were conducted using a 15 kV accelerating voltage, 30 nA beam current and 5 μm beam diameter with counting times between 10 – 30 seconds. Raw data were corrected using a stoichiometric PAP correction model (Pouchou and Pichoir, 1984) to a suite of natural and synthetic standards by microprobe software, which also provides estimates of lower limit of detection for each element. Details on standards and limits of detection can be found in Appendix B. In addition, high-resolution backscatter electron images of minerals were taken. The names and compositions of the white micas and clays investigated in this study are shown in Table 2.2 and the names and compositional ranges for chlorite end members are given in Table 2.3.

Table 2.2. White mica and clay names and general formulas

Mineral	**Formula**[1]
Muscovite	$KAl_2{}^{vi}Al^{ivs.}i_3O_{10}(OH)_2$
Paragonite	$NaAl_2{}^{vi}Al^{ivs.}i_3O_{10}(OH)_2$
Illite	$K_{0.6\text{-}0.8}Al_2{}^{vi}Al_{0.6\text{-}0.8}{}^{ivs.}i_{3.4\text{-}3.2}O_{10}(OH)_2$
Pyrophyllite	$Al_2Si_4O_{10}(OH)_2$
Kaolinite	$Al_2Si_2O_5(OH)_4$

[1] formulae are half-unit from Deer et al. (1992) and Bailey (1984)

Table 2.3. Chlorite mineral group names and stoichiometry

General Chlorite Formula: $(R^{3+}R^{2+})_6{}^{vi}(Si_{4-x}Al_x)^{iv}O_{10}(OH)_8$; $R^{3+}=Al,Fe^{3+}$, $R^{2+}=Fe^{2+},Mg,Mn$

Chlorite Group Mineral [1]	**Fe/(Fe+Mg+Mn)**	**Si (apfu)**[2]
Sheridanite	0.0-0.25	2.40-2.75
Clinochlore	0.0-0.25	2.75-3.10
Penninite	<0.25	3.10-4.0
Ripidolite	0.26-0.75	2.40-2.75
Brunsvigite	0.26-0.75	2.75-3.10
Diabanite	0.26-0.75	3.10-4.0
Thuringite	0.76-1.0	2.40-2.75
Chamosite	0.76-1.0	2.75-4.0

[1] division from Foster (1960)
[2] apfu = atoms per formula unit

2.3.4 Short-wave infrared spectroscopy

Short wave infrared (SWIR) spectra record the vibrational energy of molecular bonds within the 1300 – 2500 nm region of the electromagnetic spectrum and are plotted as reflection (percent) versus wavelength (nm). SWIR spectroscopy is particularly sensitive to -OH, $-NH_4$, $-CO_3$ radicals, H_2O molecules and cation-OH bonds such as Al-OH, Mg-OH and Fe-OH, which are present in phyllosilicates and clays. Careful analysis of the position and shape of absorption features of molecular bonds in SWIR spectra can be used to identify most mineral species and compositional variations in phyllosilicates (Thompson et al., 1999).

Spectroscopic data were collected for all samples using an Analytical Spectral Devices, Inc. TerraSpec™ short-wave infrared (SWIR) spectroscopic mineral analyzer. Sample spectra were measured by placing hand samples of rocks on a ~1 cm diameter silica glass window above a light source for approx. 30-60 s. The light source was calibrated with a white plate standard approximately every 20 samples. Raw spectra were imported into The Spectral Geologist V.7.0.1 software™ for viewing and extraction of numeric parameters such as the wavelength, width and depth of specific absorption features. Spectra were interpreted by comparing the unknown spectra to reference spectra from The Spectral Geologist™ viewer software and the USGS spectral library (Clark et al., 2007).

For white micas and clays, the Al-OH absorption at ca. 2200 nm and the molecular H_2O absorption at ca. 1910 nm are critical features for identification. For chlorites, the position of the ca. 2250 nm (Fe-OH) and ca. 2350 nm (Mg-OH) absorptions and the spectral slope from 1400 to 1900 nm have been used to identify the Fe:Mg content of chlorite species (Thompson et al., 1999). Table 2.4 outlines the characteristic features for white mica, clay, and chlorite minerals common to this study and the approximate position of their Al-OH absorption. Examples of reference spectra for white micas/clays and chlorites are shown in Figure 2.2 and Figure 2.3, respectively. Characteristic SWIR features and reference spectra are from Clark et al. (2007) and Merry and Pontual (1999). Additional details on SWIR spectroscopy and analysis can be found in Thompson et al. (1999). Spectral data used in this study is presented in Appendix E.

Table 2.4. Characteristic SWIR spectral features for phyllosilicate minerals

Mineral	Characteristic SWIR absorption features	Wavelength of Al-OH absorption (ca. 2200 nm)
Muscovite	sharp features at 1408, 1910, 2200, 2348 and 2442 nm	2198-2208
Paragonite	similar to muscovite	2185-2193
Phengitic Muscovite	similar to muscovite, slight shoulder on right side of 2200 nm feature	2208-2215
Illite	similar to muscovite except might have deeper 1910 nm absorption	2206-2210
Pyrophyllite	very sharp absorptions at 2168, 1388 nm	2168
Kaolinite	doublet centered at 1400, 2200 nm	2206-2209
Chamosite (Fe-rich chlorite)	major features at 2260 nm (symmetric), 2350 nm (asymmetric); steeply ascending hull from 1400 – 1900 nm	-
Clinochlore (Mg-rich chlorite)	similar to chamosite except major features at 2250 nm and 2330-2340 nm; gently ascending or flat hull from 1400-1900 nm	-

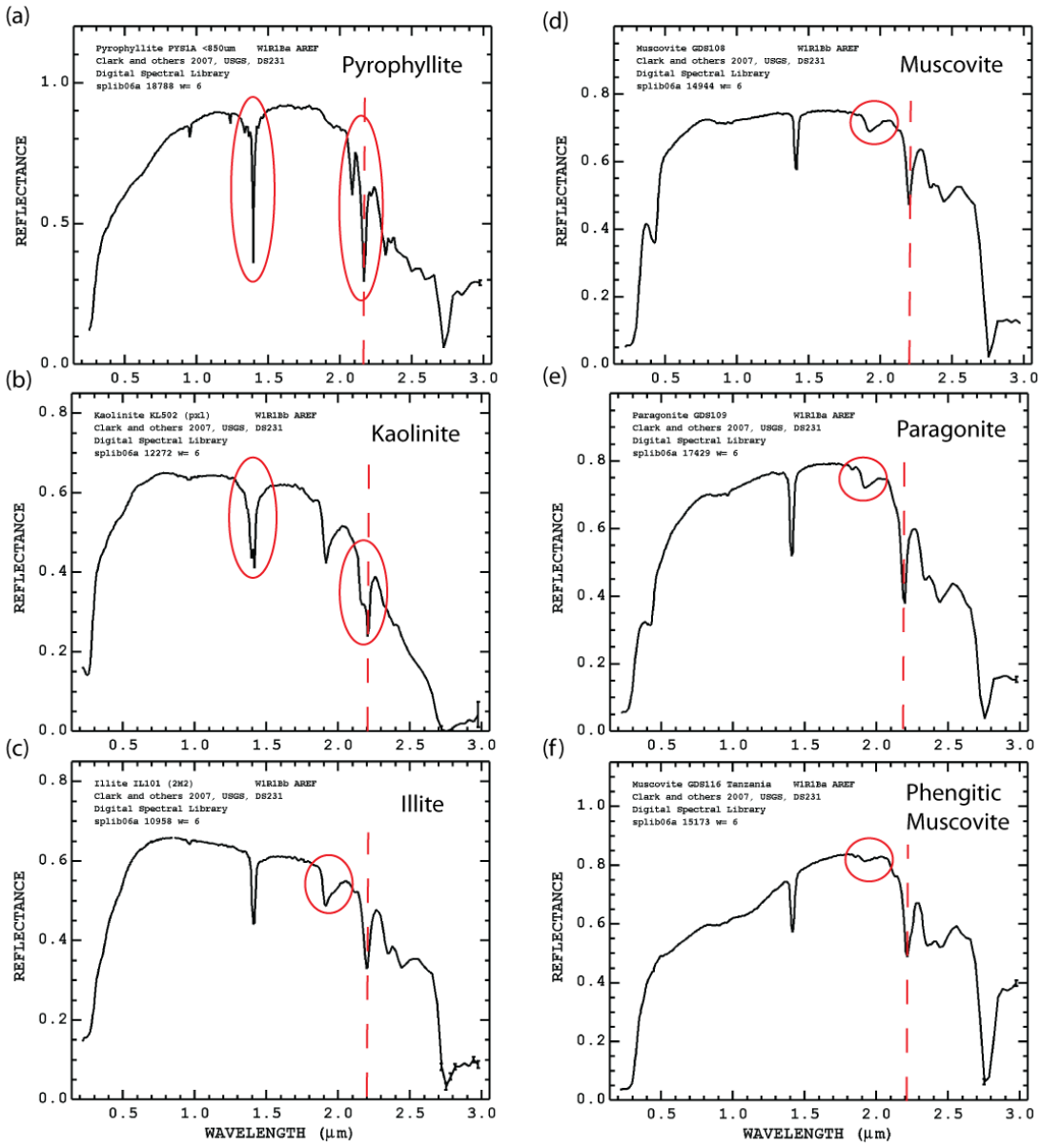

Figure 2.2. SWIR reference spectra for white mica, illite and kaolinite from USGS spectral library (Clark et al., 2007): (a) pyrophyllite, (b) kaolinite, (c) illite, (d) muscovite, (e) paragonite and (f) phengitic muscovite. Red circles highlight the characteristic features in pyrophyllite and kaolinite and the H_2O absorption feature (ca. 1900 nm) in illite, muscovite, paragonite and phengitic muscovite. Red dashed lines mark the position of the Al-OH absorption feature (ca. 2200 nm) in each spectrum, which subtly shifts from shorter wavelength in pyrophyllite and paragonite to intermediate wavelengths in muscovite and longer wavelengths in illite and phengitic muscovite (see Table 4).

2.4 Results

2.4.1 Hydrothermal alteration

In this study, alteration types are used as framework for interpreting compositional variations in hydrothermal minerals. The identification of hydrothermal alteration assemblages in porphyry systems aids in the interpretation of the physiochemical conditions of hydrothermal alteration including pressure, temperature, pH and fluid geochemistry (e.g. Meyer and Hemley, 1967; Seedorff et al., 2005; Sillitoe, 2010). Nomenclature is based on Meyer and Hemley (1967), Dilles and Einaudi (1992) and Seedorff et al. (2005).

Five general groups of alteration are identified; advanced argillic (moderate temperature), sericitic, illitic, illitic-chloritic, and propylitic. Of the many assemblages at Ann-Mason, potassic, sodic-calcic and sodic alteration types described in Dilles and Einaudi (1992) were not studied. The sericitic group is further subdivided into sericitic, weak sericitic and sericitic-chloritic (Table 2.5). Representative photomicrographs of hydrothermal alteration mineral assemblages can be found in Figure 2.3. Alteration minerals (e.g. epidote) and mineral groups (e.g. sericite) were initially identified by hand lens in the field and lab. Sample mineralogy was refined with petrography, SWIR spectroscopy, XRD and EMPA. Petrographic observations, such as textural evidence in transmitted and reflected light of thin sections and rock chips in polished mounts, are used to argue the groups of alteration minerals in Table 2.5 formed synchronously and likely in equilibrium. Measured SWIR and XRD spectra were used to identify certain unique mineral phases such as pyrophyllite and topaz. EMPA compositions were used to differentiate muscovite, illite and pyrophyllite.

Table 2.5. Hydrothermal alteration mineral assemblages

Alteration Type	Alteration Subtype	Key Minerals	Added or Re-crystallized Minerals	Relict Minerals[1]
Advanced Argillic	-	Pyroph or Alun	Qtz+Pyroph or Alun±Musc (+Rt+Py±Tp±Ba)[2]	
Sericitic	Strong Sericitic	Musc	Ser+Qtz (+Py or Hem+Rt+Tm±Cp)	
	Sericitic-Chloritic	Chl+Musc ±[Fsp][4]	Chl+Musc (+Hem[a] or Py[b]+Rt±Calc)	Ab±Ksp±Biot (±Mgt±Sph)
	Weak Sericitic	Musc+[Fsp]	Musc±Ill (+Py+Rt±Cp)	Ab±Ksp(±Sph)
Intermediate Argillic	Illitic	Ill+[Fsp]	Ill(+Py+Rt)	Ab+Ksp(±Sph)
	Illitic-Chloritic	Chl+Ill +[Fsp]	Chl+Ill(+Py+Rt)	Ab+Ksp+Ep +Biot(+Sph)
Propylitic	-	Chl+[Fsp]	Chl±Act±Ep±Ab (±Calc±Ser±Hem+Rt±Cp)	Olg/Ans+Ksp ±Hbl±Biot (+Mgt+Sph)

[1] igneous quartz and accessory apatite and zircon are present as relict minerals in all assemblages
[2] ( ) indicates trace phase
[3] a or b letter indicates iron trace phase (a=hematite; b=pyrite)
[4] [ ] indicate relict minerals useful in identifying and interpreting certain alteration types

Although the hypogene sulfide is presented in Table 2.5, only samples from drill core contain hypogene sulfides (pyrite and chalcopyrite). In surface samples, sulfides have been oxidized and replaced by supergene phases such as goethite, jarosite, glassy limonite or other amorphous limonite, local earthy red hematite and various Mn±Cu oxides (pyrolusite, tenorite and “copper wad”).

Figure 2.3. Photomicrographs of hydrothermal alteration assemblages in cross-polarized light. Thin sections in a, b, c, e, f are 100 μm thick, d is 30 μm thick. (a) Advanced argillic alteration (H437113), radiating sheaves of pyrophyllite with quartz. (b) Weak sericitic alteration (G909152), muscovite pseudomorphs of hydrothermal biotite (replacing hornblende), groundmass replaced by muscovite and quartz, relict albite phenocrysts. (c) Illitic alteration (G909163), illite veinlet cutting partially altered igneous plagioclase phenocryst. (d) Sericitic-chloritic alteration (YD08-22), muscovite replacing plagioclase phenocryst (5 vol.% remaining), fine-grained muscovite and chlorite in groundmass. (e) Illitic-chloritic (G909158), illite replacing plagioclase phenocryst (20 vol.% remaining), chlorite and epidote replacing biotite, relict albite and K-feldspar. (f) Propylitic (G909172), chlorite partially replacing igneous “book” biotite, feldspar stable.

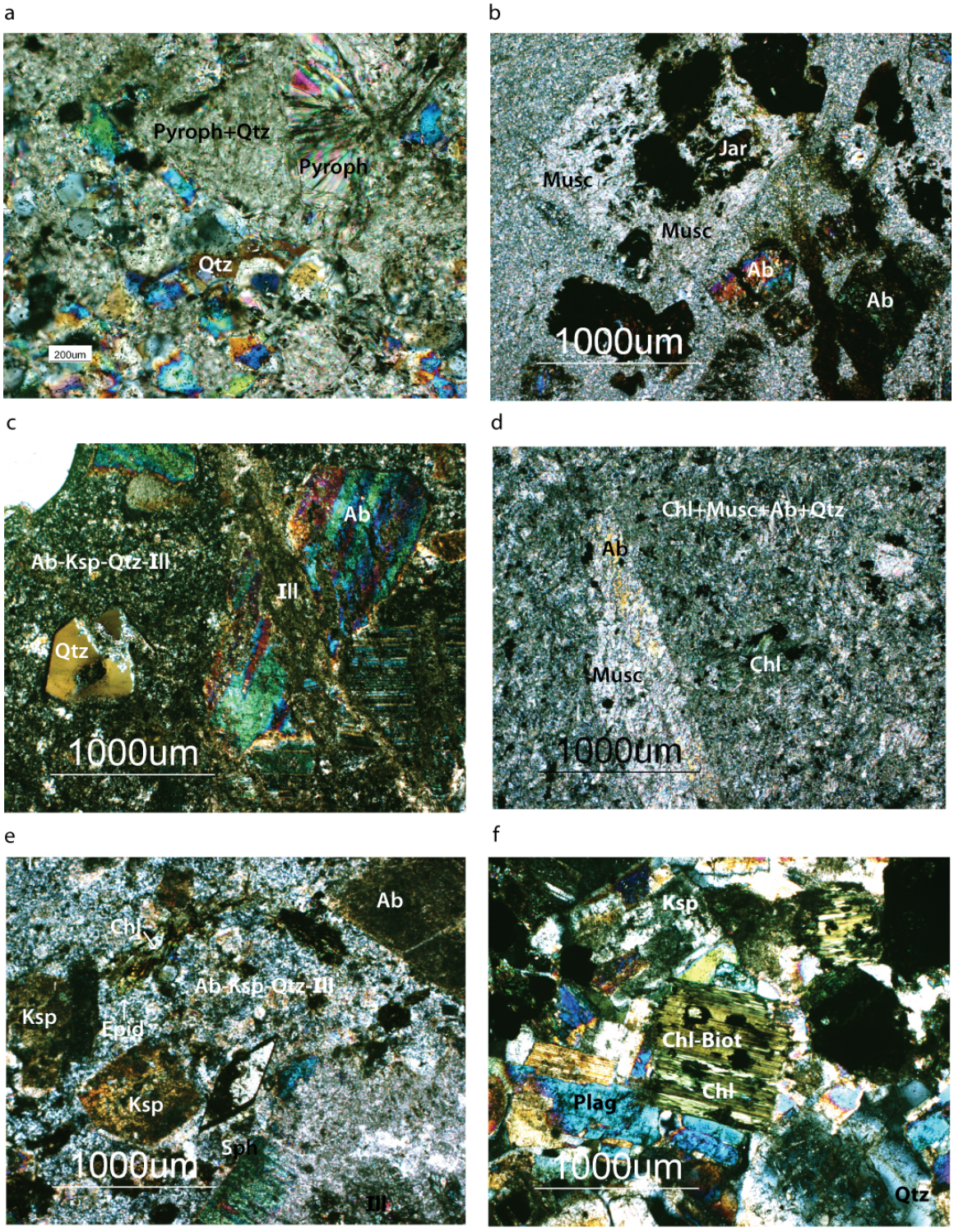

Figure 2.3. Photomicrographs of hydrothermal alteration assemblages in cross-polarized light.

2.4.1.1 Advanced argillic

Advanced argillic alteration in the Blue Hill fault block is similar to the advanced argillic assemblages found in the Buckskin Range and defined by Lipske (2002). As in the Buckskin Range, advanced argillic alteration is defined by the presence of pyrophyllite or alunite and is texturally destructive, commonly composed of subhedral medium to coarse-grained (10-100 μm dia.) quartz (10-90 vol. %); euhedral coarse-grained (50 – 1000 μm long) muscovite (10-75 vol. %) and coarse-grained (100-1000 μm long) pyrophyllite (Figure 2.3a). Mica often forms sheaves of intergrown radiating crystals. Lipske (2002) demonstrated that some mica with this texture contains cores of pyrophyllite and are muscovite pseudomorphs earlier pyrophyllite. Other minerals identified in advanced argillic alteration include topaz, barite, alunite, huangite [$Ca_{0.5}Al_3(SO_4)_2(OH)_6$ or Ca-alunite], rutile, specular hematite and clays (dickite, halloysite). Although the surface exposures have been oxidized and weathered, disseminated pyrite (up to 10 vol. %) with rare chalcopyrite (>50:1 py:cp) is inferred based on Fe-oxide pseudomorphs of sulfides, goethite-lined boxwork cavities and supergene goethite, jarosite, chrysocolla and turquoise.

Advanced argillic alteration primarily occurs along steeply to gently dipping faults, joints and permeable rock units in the Artesia Lake volcanics in the upper kilometer of the hydrothermal system. Exposures of this environment occur in the Buckskin Range and western portions of the Blue Hill fault block. Advanced argillic alteration did not affect the middle Jurassic Fulstone Springs volcanics that overlie the Artesia Lake volcanics (Lipske, 2002; Lipske and Dilles, 2000). Advanced argillic alteration occurs as cm- to m-scale inner selvages along "D" veins (i.e. Gustafson and Hunt, 1975) or forms massive dm-scale quartz-alunite±pyrophyllite zones. In all cases, advanced argillic alteration is enclosed within outer selvages of sericitic alteration.

2.4.1.2 Sericitic

Sericitic alteration occurs throughout the upper parts of the hydrothermal system in the Yerington District and has been mapped in the Buckskin Range (Lipske, 2002), in the central and western portions of the Blue Hill fault block and in the western portion of Ann-Mason (Dilles and Einaudi, 1992; Dilles et al., 2000b). In this study, sericitic

alteration is subdivided based on the stability of feldspar and the presence of chlorite. These subdivisions are described below and their spatial relationships documented in trench maps (Appendix C).

2.4.1.2.1 Strong sericitic

Strong sericitic alteration is texturally destructive. All igneous phases are replaced by subhedral granular medium to coarse-grained (10-100 μm dia.) quartz (~ 50-75 vol %), euhedral coarse-grained (100-500 μm long) muscovite (~ 25-50 vol %), pyrite (~5 vol %, >50:1 py:cp), often tourmaline (3-5 vol %) and minor rutile. This alteration occurs proximal to "D" veins (Gustafson and Hunt, 1972) in 1 cm to 1 m wide selvages. At Blue Hill, as noted at Ann-Mason in Dilles and Einaudi (1992) and illustrated in Dilles et al. (2000), "D" veins and selvage widths increase from narrow (1-2 mm) to wide (1-2 m) moving upward or westward, away from the ore zone.

2.4.1.2.2 Weak sericitic

The distinction between strong and weak sericitic alteration is based on the stability of feldspar. In strong sericitic alteration, all feldspar has been converted to muscovite but in weak sericitic alteration, some plagioclase and K-feldspar remains (10-70 vol. %). In weak sericitic alteration, rock texture is preserved but all mafic phases have been altered to medium to coarse-grained muscovite, pyrite and rutile, as seen in Figure 2.3b. Calcic plagioclase feldspar and, often k-feldspar, have been converted to albite, as a result of sodic alteration that typically predates sericitic alteration (Carten, 1986; Dilles and Einaudi, 1992). Feldspar phenocrysts have been partially altered to muscovite and quartz, and the groundmass of granite porphyries has been altered to muscovite, quartz, pyrite and rutile with relic feldspar. Texturally, muscovite pseudomorphs igneous "book" or hydrothermal "shreddy" biotite or occurs as randomly oriented sheaves (10-100 μm long), often with a radiating texture with intergrown anhedral quartz and rutile. Goethite and jarosite occur in fractures and supergene veinlets and as fracture coating, primarily on relic feldspar phenocrysts.

Weak sericitic alteration is often found as a outer selvage on "D" veins (0.5 – 5 m) with inner strong sericitic selvages (Dilles et al., 2000b). Figure 2.4 is a photograph

of thin section #G909173 from the "Discovery Trench" at Ann-Mason (Dilles et al., 2000, Figure 12) showing an example of the spatial relationship between a thin (~ 2 mm) "D" vein with a narrow inner strong sericitic selvage and outer weak sericitic selvage. Weak sericitic alteration is common in the central portion of the Blue Hill fault block. At Ann-Mason, the high level albite-sericite (A-2) alteration mapped by Dilles and Einaudi (1992) includes chlorite-poor zones that would be termed weak sericitic here.

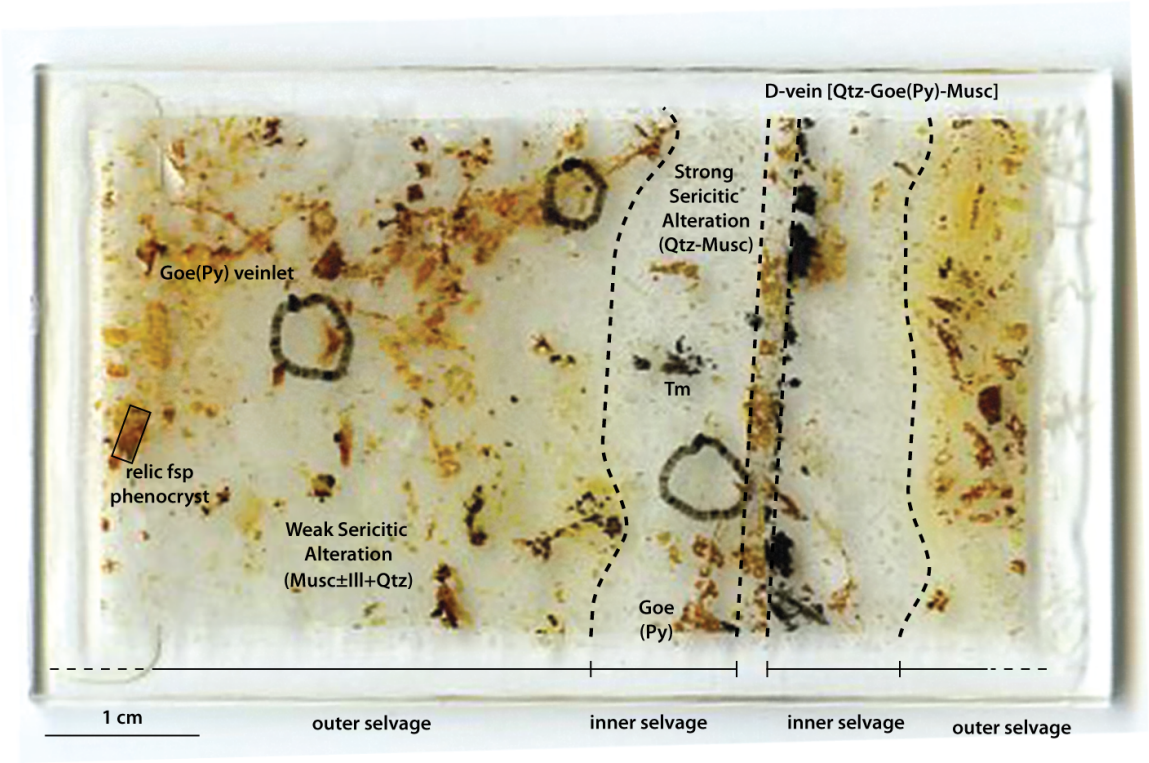

Figure 2.4. Photograph of a thin section from sample G909173 from the Ann-Mason "Discovery Trench" (Dilles et al., 2000) showing the spatial relationship between "D" veins and strong and weak sericitic selvages. This is a thin (~ 2 mm) D-vein typical of the D-vein morphology found near the ore zone.

2.4.1.2.3 Sericitic-chloritic

In sericitic-chloritic alteration, rock texture is preserved but mafic phases have been altered to chlorite, muscovite, quartz, minor rutile and hematite or locally pyrite. Chlorite (15-40 vol %) and muscovite (20-30 vol %) are fine to medium-grained (10-200 μm long) and often occur as intergrown sheaves with interstitial anhedral quartz (20-30 vol %), as shown in Figure 2.3d. In some samples, hematite (5-10 vol %) occurs as

specular hematite either in veins with quartz or disseminated in the groundmass. Plagioclase is commonly dusted by <25% sericite (musc ± illite). Feldspar is stable in all but one sample (YD01-13A) in which all feldspar has been replaced by quartz and muscovite.

At Blue Hill, sericitic-chloritic alteration with hematite predominantly occurs in the Artesia Lake andesite lavas as an outer selvage on "D" veins and enveloping sericitic and locally advanced argillic alteration inner selvages. Lipske (2002) described similar alteration with in the Buckskin Range as "sericite-hematite-chlorite alteration". Sericitic-chloritic alteration with pyrite is found in granite porphyry samples from Ann-Mason drill core. At Ann Mason, Dilles and Einaudi (1992) described similar "albite-chlorite±sericite" (A2) alteration.

2.4.1.3 Intermediate Argillic

2.4.1.3.1 Illitic

Illitic alteration is similar to weak sericitic alteration except all white micas are illite, on the basis of composition by EMPA. In addition, feldspar stability is greater than in sericitic alteration with 50 – 90 vol% feldspar relict in thin section. Illite occurs as randomly oriented sheaves replacing feldspar and, locally, biotite and is often finer-grained (10-50 μm) than muscovite (Figure 2.8). Illite also occurs as inner selvages on very thin (0.1-0.2 mm wide) pyrite + minor quartz veinlets or very thin (0.1-0.2 mm wide) veinlets (Figure 2.3c).

2.4.1.3.2 Illitic-Chloritic

In illitic-chloritic alteration, rock texture is preserved. Hornblende and biotite have been partially or fully altered to chlorite, rutile and minor pyrite, as shown in Figure 2.3e. Calcic plagioclase has been converted to albite and partially replaced (~70% relict) by fine-grained (5-50 μm dia.) illite. K-feldspar is stable or partially altered to albite. The groundmass of granite porphyries contains relic feldspar and is partially altered to either illite or muscovite and quartz. Epidote (5-10 %), related to a separate, and likely earlier, propylitic or sodic-calcic hydrothermal event, replaces plagioclase phenocrysts or groundmass in porphyry dikes.

Illitic-chloritic alteration is relatively weak and has not been previously documented at Yerington and its origin in porphyry Cu systems is poorly understood (Dilles, J. H., manuscript). At Blue Hill and Ann-Mason, illitic-chloritic alteration occurs proximal to illitic alteration along the flanks of main mineralized porphyry dike zones and illitic zone. Both the illitic and illitic-chloritic alteration zones are lower temperature and therefore likely post-date muscovite-bearing sericitic alteration, but this relationship can only be inferred by the range of their temperature stability and has not been demonstrated via cross-cutting age relationships.

2.4.1.4 Propylitic

Propylitic alteration refers to weakly altered rocks with added actinolite, epidote, calcite, and chlorite and relict plagioclase, K-feldspar, and magnetite. Rock texture is preserved and mafic phases are partially to fully replaced by chlorite (3-20 vol %) and/or actinolite (0-20 vol %), trace rutile, magnetite, hematite and locally pyrite (Figure 2.3f). Plagioclase is commonly dusted by sericite of unknown composition or partially replaced by epidote (up to 10 vol %) or calcite and is partially converted to albite. K-feldspar is generally fresh, or rarely dusted with sericite.

Propylitic alteration is concentrated in the northwestern part of Blue Hill and in the southwestern part of Ann-Mason and primarily found in lithologies of the Yerington batholith. Propylitic alteration corresponds to propylitic (PA) alteration of Dilles and Einaudi (1992) and follows the broad definition of Meyer and Hemley (1967). Previous studies have demonstrated that propylitic and sodic-calcic alteration are closely associated and the result of alteration by hypersaline sedimentary brines that circulated through the Yerington batholith during porphyry copper deposit formation (Carten, 1986; Dilles and Einaudi, 1992; Dilles et al., 1992, 2000) (see Chapter 1 for more detail).

2.4.2 Mineral compositions

2.4.2.1 White mica and Illite

White micas and clay mineral compositions determined by EMPA include pyrophyllite, muscovite and phengitic muscovite, paragonite, and illite according to definitions by Deer et al., (1992). A summary of mineral compositions by EMPA is displayed in Table 2.7 and all EMPA data is presented in Appendix D. Illite is a potassium-deficient clay compared to muscovite, and defined by interlayer cation (K+Na+2Ca) site occupancy of between 0.6-0.8 atoms per formula unit (apfu) (Bailey, 1984). Illite compositions are solid solution between muscovite and pyrophyllite end members. EMPA data in percent oxide for micas and clays were recalculated to atoms per formula unit on the basis of a sum cationic charge of 11 equivalent to $O_{10}(OH,F,Cl)_2$ anions. All iron was calculated as Fe^{2+} (Newman, 1987). The observed compositional range is $(K_{0.03\text{-}1.05}Na_{0.01\text{-}0.88})(Fe_{0.0\text{-}0.56}\ Mg_{0.0\text{-}0.44}\ Al_{1.52\text{-}2.09})^{vi}(Si_{2.92\text{-}3.38}Al_{0.62\text{-}1.09})^{iv}O_{10}(OH)_2$. The interlayer cation site occupancy (K+Na+2Ca) ranges from 0.59 to 1.06 apfu. In the octahedral site, Fe+Mg+Mn content ranges from 0.0 to 0.68 apfu.

Compositional variations in white mica and illite can be described by four substitution mechanisms illustrated by arrows in Figure 2.5; (1) phengitic or Tschermak substitution $[(Al^{3+})^{vi} + (Al^{3+})^{iv} <-> (Fe^{2+} \text{ or } Mg^{2+})^{vi} + (Si^{4+})^{iv}]$, (2) direct $(Fe^{3+})^{vi} <-> (Al^{3+})^{vi}$ substitution, (3) illitic substitution $[(K^{+})^{\text{interlayer cation site}} + (Al^{3+})^{iv} <-> (Si^{4+})^{iv} + [\ ]^{\text{interlayer cation site}}]$, (4) $Na^{+} <-> K^{+}$ exchange in the interlayer cation site.

The two arrows Figure 2.5a illustrate the slope of two substitutions; (1) phengitic substitution and (2) $Fe^{3+} <-> Al^{3+}$ substitution. Data lie between these two trends suggesting a substitution by both Fe^{2+} and Fe^{3+}. The mole fraction of $Fe^{3+}/(Fe^{TOT}+Mg+Mn)$ can be estimated using the slope of a line fitted thru the data (Figure 2.5a). Using a least-squares regression method with a y-intercept at zero, as shown by the dashed line on Figure 2.5a, the data can be represented by the equation:

$$(5) \qquad y = -0.6981x;\ R = 0.93$$

If $Fe^{3+}/(Fe^{TOT}+Mg+Mn) = 1$, then the slope (m) = -1.0; if $Fe^{3+}/(Fe^{TOT}+Mg+Mn) = 0$, then m = -0.5. Therefore if m = -0.6981, $Fe^{3+}/(Fe^{TOT}+Mg+Mn) = 0.3962$ and indicates ~ 40% contribution of Fe^{3+} to measured Fe+Mg+Mn (apfu) contents.

Minerals where Al^{vi} and Al^{iv} have been replaced by $Fe(Mg)^{vi}$ and Si^{iv} are termed phengitic. For this study, micas termed "phengitic muscovite" have greater than 0.2 apfu Fe+Mg+Mn. Both muscovite from sericitic-chloritic and illite from intermediate argillic alteration are more phengitic than muscovite from sericitic and advanced argillic alteration. Muscovite in altered samples with chlorite present has the highest $Fe^{3+}/(Fe^{TOT}+Mg^{2+}+Mn^{2+})$ values (Figure 2.5a).

Table 2.7. Representative analyses of muscovite, illite, paragonite-muscovite and pyrophyllite by EMPA

Mineral	Muscovite	Paragonite-Muscovite	Muscovite	Illite	Illite	Muscovite	Muscovite	Pyrophyllite
Alteration Type	Strong Sericitic	Strong Sericitic	Weak Sericitic	Illitic	Illitic-chloritic	Sericitic-Chloritic	Sericitic-Chloritic	Advanced Argillic
Lithology	Granite porphyry	Artesia Lake andesite	Granite porphyry	Granite porphyry	Granite porphyry	Granite porphyry	Artesia Lake andesite	Granite porphyry
Sample #	ANN006002.018	H437199	G909160	G909163	G909158	ANN007006.017	YD01-13A	H437113
# of grains (# of analyses)	3(15)	4(22)	2(9)	2(10)	1(6)	2(8)	3(16)	2(9)
Region	Ann-Mason Drill Core	Western Blue Hill	Western Blue Hill	Western Blue Hill	Central Blue Hill	Ann-Mason Drill Core	Western Blue Hill	Western Blue Hill
SiO_2	47.48	47.81	47.56	49.12	50.17	45.39	46.32	66.78
TiO_2	0.51	<0.02	0.15	0.14	0.08	0.06	0.05	<0.02
Al_2O_3	35.91	40.60	34.15	29.88	29.86	31.06	33.92	26.91
FeO	0.66	<0.07	0.68	3.11	2.59	4.59	3.43	<0.07
MnO	0.01	<0.06	<0.06	<0.06	<0.06	<0.06	<0.07	<0.06
MgO	1.52	0.05	2.00	2.62	2.69	2.20	1.13	<0.03
CaO	0.01	<0.02	<0.02	<0.02	<0.02	<0.02	0.00	0.12
Na_2O	0.27	5.02	0.35	0.12	0.14	0.15	0.46	0.11
K_2O	10.94	1.72	9.00	8.68	7.85	11.42	10.00	<0.06
F	0.21	0.19	<0.13	0.47	0.18	<0.13	0.36	<0.13
Cl	0.01	<0.03	<0.03	<0.03	<0.03	<0.03	<0.04	<0.05
Total	97.58	95.53	94.15	94.35	93.72	95.19	95.77	94.29
H_2O	4.52	4.63	4.44	4.25	4.39	4.30	4.31	4.92
Total	102.01	100.08	98.54	98.40	98.02	99.42	99.93	99.19
Structural Formulas - based on 11 O equivalents								
Si	3.078	3.026	3.160	3.287	3.346	3.106	3.203	4.000
Al(iv)	0.922	0.974	0.840	0.713	0.654	0.894	0.797	0.000
Al(vi)	1.822	2.055	1.834	1.643	1.693	1.613	1.689	1.970
Fe	0.036	0.000	0.038	0.174	0.144	0.265	0.207	0.000
Mn	0.001	0.000	0.000	0.000	0.000	0.000	0.000	0.000
Mg	0.147	0.005	0.199	0.261	0.267	0.224	0.162	0.001
Na	0.034	0.616	0.045	0.015	0.018	0.020	0.016	0.014
K	0.904	0.139	0.763	0.741	0.668	0.998	0.904	0.000
Al(total)	2.743	3.028	2.674	2.357	2.347	2.507	2.486	1.922
Fe+Mg+Mn	0.183	0.005	0.236	0.436	0.412	0.489	0.371	0.001
K+Na+Ca	0.939	0.756	0.808	0.757	0.687	1.018	0.924	0.023
K/(K+Na+Ca)	0.963	0.184	0.944	0.979	0.973	0.980	0.978	0.000
Mg/(Mg+Fe+Mn)	0.802	1.000	0.840	0.600	0.649	0.458	0.438	1.000

* Values below the limit of detection are represented as < x where x = average limit of detection given in Appendix B.

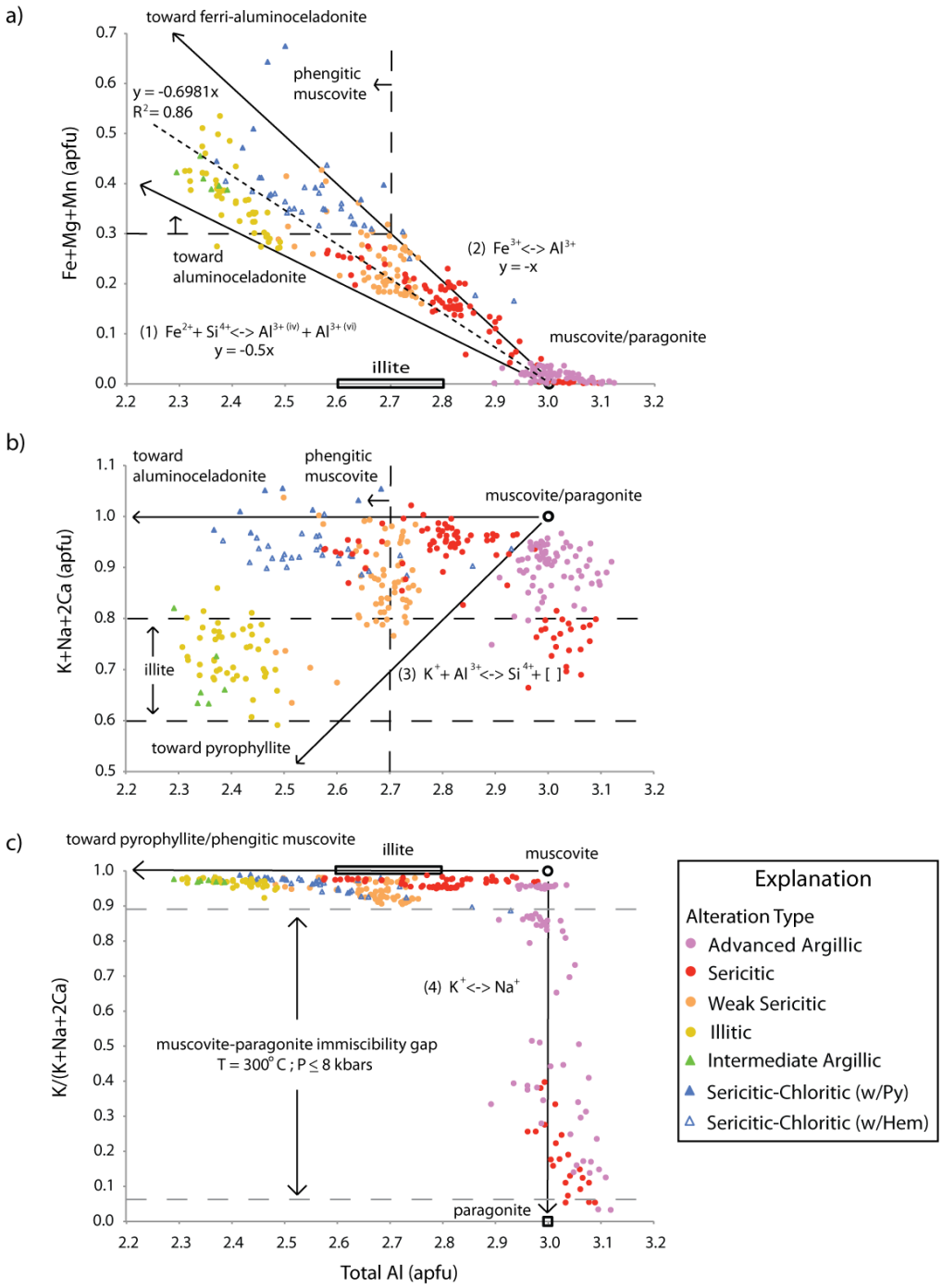

Figure 2.5. Compositional variations in white mica: A) Al (apfu) vs. Fe+Mg+Mn (apfu), B) Al (apfu) vs. K+Na+2Ca (apfu) and C) Al (apfu) vs. atomic K/(K+Na+2Ca). The colors and shapes represent hydrothermal alteration mineral types and subtypes outlined in Table 2.5. Open symbols represent samples with hematite as the primary Fe trace phase. Arrows represent compositional vectors for main substitution mechanisms and black open symbols represent end-member compositions.

In phengitic muscovite and illite, the proportion of Fe:Mg in the octahedral site as demonstrated by [Mg/(Mg+Fe+Mn)] variation. Hematite-bearing samples (open triangles) generally have a greater proportion of iron [Mg/(Mg+Fe+Mn) < 0.5] than sulfide-bearing samples, as shown in Figure 2.6. This is likely the result of hematite buffering the iron oxide (FeO) activity at a higher level during this alteration compared to sulfide-bearing samples.

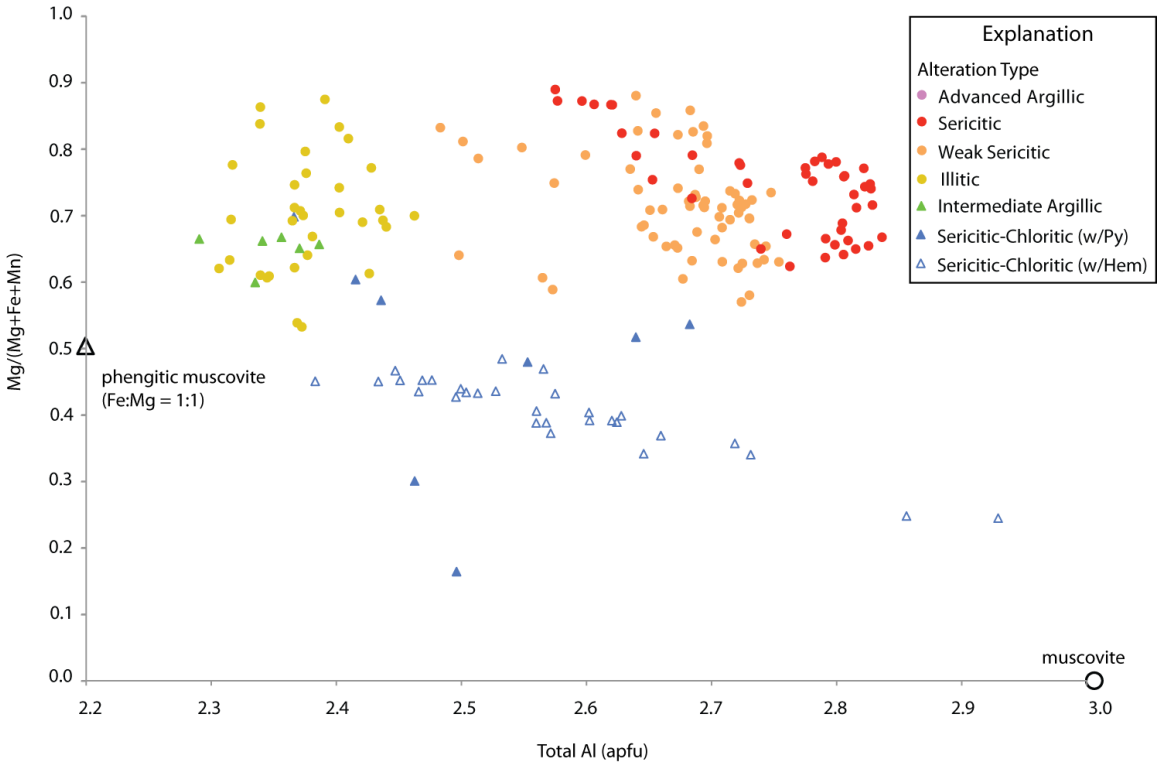

Figure 2.6. Total Al (apfu) vs. atomic Mg/(Mg+Fe+Mn) plot for muscovite and illite analyses with >0.1 apfu Fe+Mg+Mn.

Figure 2.5b allows comparison between (3) illitic substitution and (1) phengitic substitution. Illitic substitution will decrease the K+Na+2Ca (apfu) and total Al (apfu) content in a 1:1 atomic ratio, as illustrated by the arrow extending from muscovite towards pyrophyllite. Phengitic substitution, illustrated by the horizontal arrow, will decrease the total Al but does not affect the K+Na+2Ca (apfu) content.

Illite is found in samples from intermediate argillic alteration and in several samples from weak sericitic alteration that also contain muscovite. In most cases,

coarser-grained muscovite or chlorite replaces hornblende or hydrothermal biotite whereas finer-grained illite replaces plagioclase and K-feldspar. Notably, illite and muscovite are present in several samples without any discernable difference in their morphology or grain size (G909152). As shown in Figure 2.7, although the mean grain size for muscovite is greater than that of illite, however, there is substantial overlap and grain size cannot be used to distinguish the two minerals. None of the hydrothermal illite grains measured correspond to the <5 um definition of illite commonly used for diagenetic clays in sedimentary rocks (Bailey, 1984).

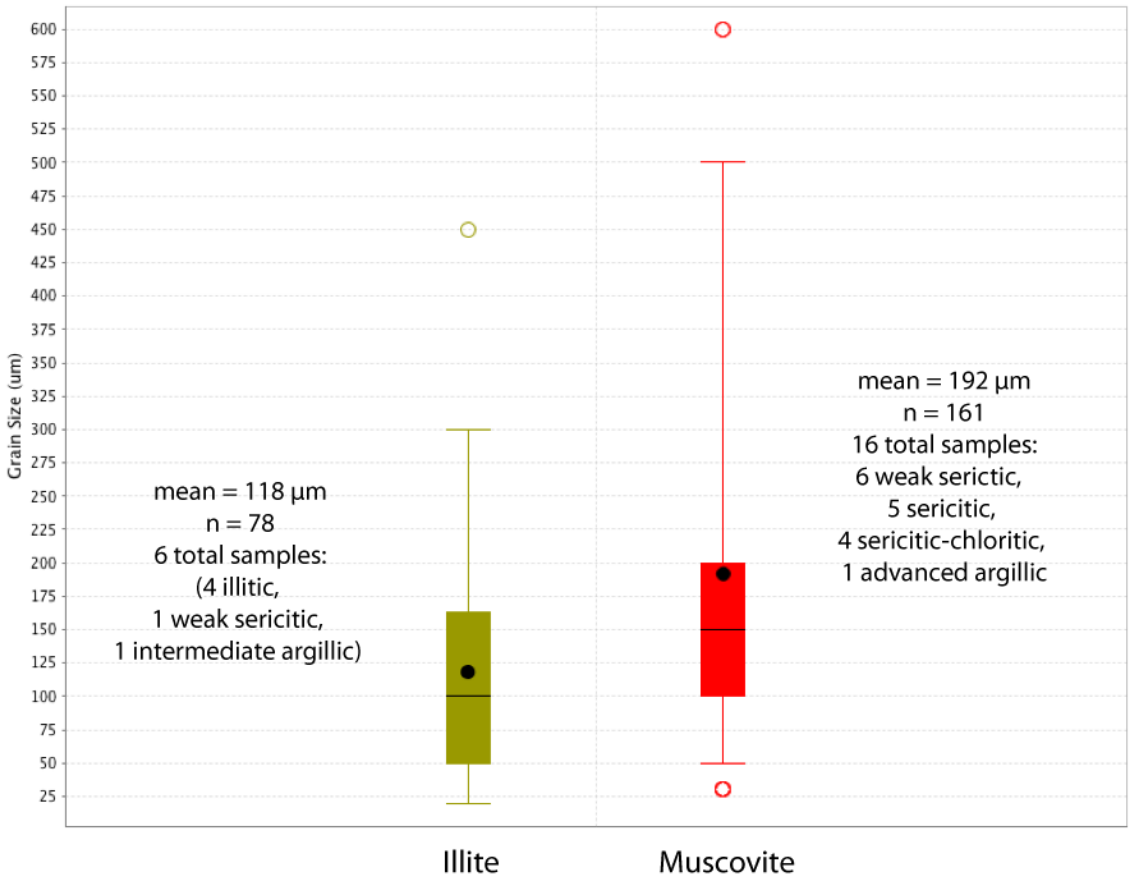

Figure 2.7. Box and whisker (Turkey) plots of grain sizes (µm) for illite and muscovite. The black dots are the mean values. The box represents the middle 50% of the data, which is split by a line that represents the median. The whiskers are the 5% and 95% values and open circles represent outliers.

In (3) Na-K substitution, Na^+ substitutes for K^+ in the interlayer cation site and the proportion of potassium in the interlayer cation site [K/(K+Na+2Ca)] can be used as a measure of Na-K substitution, as in Figure 2.5c. Although the K/(K+Na+Ca) ranges from 0.0 – 0.99, the majority of the variation comes from two samples of Artesia Lake andesite lavas (YD02-02 and H437199) with intense advanced argillic or sericitic alteration in northern portion of the Blue Hill fault block. In sample YD02-02, the BSE image shows darker, Na-rich mica that appears to be replacing the lighter more K-rich mica along grain boundaries as shown in Figure 2.8a. Sample H437199 does not show the same replacement textures (Figure 2.8b). There is an immiscibility gap between muscovite and paragonite that widens as temperature decreases. Guidotti et al. (1994) measured the composition of natural muscovite-paragonite pairs using EMPA to determine the P-T-X limits of the binary muscovite-paragonite solvus. According to their model, at T = 300° C and P ≤ 8 kbars, muscovite can contain up to ~ 11 mol % paragonite whereas paragonite can contain up to 6 mol % muscovite (Guidotti et al., 1994, Fig. 2). Intermediate compositions from K/(K+Na+2Ca) = 0.15 to 0.68, found by EMPA (Figure 2.8) and illustrated in Figure 2.5c, are more likely physical mixtures rather than a true solid-solution of paragonite and muscovite components in mica.

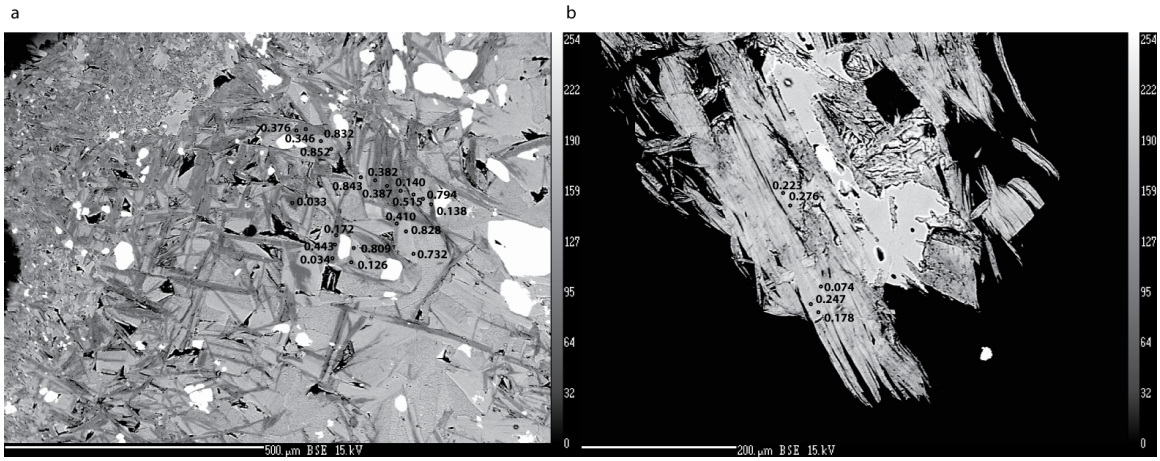

Figure 2.8. BSE images of samples with paragonite and muscovite. Dots represent EMPA spots and numbers are K/(K+Na+2Ca) proportion at spot. (a) YD02-02, Na-rich mica (dark colored elongate crystals) appears to be have replaced the dominate sheets of coarse K-rich mica (lighter color) along cleavages, fractures and grain boundaries. (a) H43199, coarse tabular white mica has composition by EMPA between paragonite and muscovite [0.01 – 0.3 K/(K+Na+2Ca)].

2.4.2.2 Chlorite

Most chlorites compositions are brunsvigite or ripidolite whereas a few fall into the sheridanite and clinochlore fields based on the compositional divisions outlines in Foster (1962) (Figure 2.9a). Chlorite analyses have been recalculated on an atomic basis to a cation charge of 14 or $O_{10}(OH)_8$ anions. All iron was assumed to be Fe^{2+} (Foster, 1962; (Newman, 1987). The chlorite compositional range is $(Al_{0.94\text{-}1.62}Fe_{0.78\text{-}2.47}Mg_{2.0\text{-}4.02})(Si_{2.48\text{-}3.02}Al_{0.98\text{-}1.52})O_{10}(OH)_8$. Tetrahedral cation composition ranges from $(Si_{3..02}Al_{0.98})$ to $(Si_{2.48}Al_{1.52})$. The sum of the octahedral sites (sum oct) ranges from 5.60 to 6.06 apfu. Mg/(Mg+Fe+Mn) content ranges from 0.45 to 0.84 and octahedral Al ranges from Al^{vi}/(sum oct) = 0.16 to 0.28 apfu. A summary of chlorite compositions is presented in Table 2.8 and all chlorite analyses can be found in Appendix C.

Chlorite compositional variations can be described by two types of substitution: (1) phengitic or Tschermak substitution [$Al^{3+,vi} + Al^{3+,iv}$ <-> $(Fe^{2+}$ or $Mg^{2+})^{vi} + (Si^{4+})^{iv}$] (Figure 2.9b), and (2) octahedral Fe^{2+} <-> $Mg^{2+}(Mn^{2+})$ substitution (Figure 2.9a). Ideal chlorite has no K, Na or Ca in the interlayer cation site, but minor amounts of K+Na+2Ca (apfu) in chlorite were observed in the Yerington samples. Elevated K+Na+2Ca (apfu)

content is likely due to <1 μm-scale interlayering of white mica (K and/or Na) or actinolite (Ca) within the dominantly chlorite sheet structure, similar to the 10 Å mica packets found randomly interlayered with stacks of chlorite described in Carrillo-Rosua et al., (2009). Chlorites with K+Na+2Ca > 0.02 apfu were considered to be mixed with muscovite or actinolite and are excluded from the chlorite analyses.

Generally, chlorites from muscovite- or illite-bearing assemblages have higher Al contents and a greater proportion of octahedral Al (>0.20 Al^{vi}/sum oct) than chlorites from propylitic alteration (Figure 2.9b), although there are exceptions to this trend. Chlorites from sericitic-chloritic alteration with pyrite as the dominant Fe trace phase have lower atomic Al^{vi}/(sum oct) values than chlorite from sericitic-chloritic alteration with hematite. The Fe/(Fe+Mg+Mn) content of chlorites should be correlated with the presence of hematite as shown for white mica/illite data in the previous section. The data in Figure 2.9a do not show this trend. Although most Fe-rich chlorites come from samples that also contain hematite, Mg-rich chlorites are also associated with samples that are hematite-bearing.

Table 2.8. Representative analyses of chlorite by EMPA

Alteration type	Intermediate Argilic	Intermediate Argilic	Sericitic-Chloritic (+Py)	Sericitic-Chloritic (+Hem)	Propylitic	Propylitic	Propylitic	Propylitic
Lithology	Granite porphyry	Granite porphyry	Granite porphyry	Artesia Lake andesite	McLeod quartz monzodiorite	Granite porphyry	McLeod quartz monzodiorite	Bear quartz monzonite
Sample #	G909158	YD09-04	ANN007006.017	YD01-13A	ANN006001.045	G909168	G909174	YD01-04
# of grains (# of analyses)	2(11)	3(17)	3(12)	3(25)	3(16)	3(13)	2(15)	3(27)
Region	Central Blue Hill	Central Blue Hill	Ann-Mason Drill Core	Northern Blue Hill	Ann-Mason Drill Core	Western Blue Hill	Ann-Mason	Northern Blue Hill
SiO_2	28.97	32.43	28.03	24.23	28.23	27.77	27.53	28.137
TiO_2	0.04	0.03	0.05	0.02	0.04	0.05	<0.02	<0.02
Al_2O_3	20.34	20.28	19.49	24.02	20.74	19.64	19.84	20.194
FeO	16.90	13.35	15.44	26.04	14.92	20.62	21.05	18.924
MnO	0.38	0.26	0.06	0.23	0.06	0.45	0.20	0.175
MgO	20.91	22.10	23.73	13.75	24.32	19.11	19.91	21.876
CaO	0.04	0.36	<0.02	<0.02	<0.02	<0.02	0.03	<0.02
Na_2O	<0.05	0.21	<0.05	<0.05	<0.05	<0.05	<0.05	<0.05
K_2O	0.27	0.32	<0.06	<0.06	<0.06	<0.06	<0.06	<0.06
F	<0.13	0.29	0.27	<0.13	<0.13	<0.13	<0.13	0.016
Cl	<0.03	<0.03	<0.03	<0.03	<0.03	<0.03	<0.03	<0.03
Total	88.07	89.66	87.25	88.47	88.70	87.87	88.85	89.452
H_2O	11.93	12.39	11.80	11.41	12.11	11.67	11.76	12.006
Total	99.96	101.93	98.93	99.87	100.74	99.53	100.58	101.426
Structural Formulas - based on 14 O equilvalents								
Si	2.897	3.098	2.815	2.541	2.778	2.848	2.797	2.737
Al(iv)	1.103	0.902	1.185	1.459	1.222	1.152	1.203	1.263
Al(vi)	1.295	1.383	1.122	1.510	1.183	1.221	1.173	1.052
Fe	1.415	1.070	1.297	2.285	1.228	1.769	1.789	1.539
Mn	0.032	0.021	0.007	0.021	0.006	0.039	0.018	0.014
Mg	3.119	3.158	3.552	2.150	3.567	2.920	3.016	3.172
K	0.035	0.039	-	-	-	-	-	-
Al(total)	2.398	2.285	2.307	2.969	2.406	2.373	2.375	2.315
Fe+Mg+Mn	4.566	4.249	4.856	4.455	4.801	4.728	4.822	4.726
Mg/(Mg+Fe+Mn)	0.683	0.743	0.732	0.483	0.743	0.618	0.625	0.671
Al(vi)/(sum Oct)	0.219	0.241	0.188	0.253	0.197	0.205	0.195	0.182

* Values below the limit of detection are represented as < x where x = average limit of detection given in Appendix B.

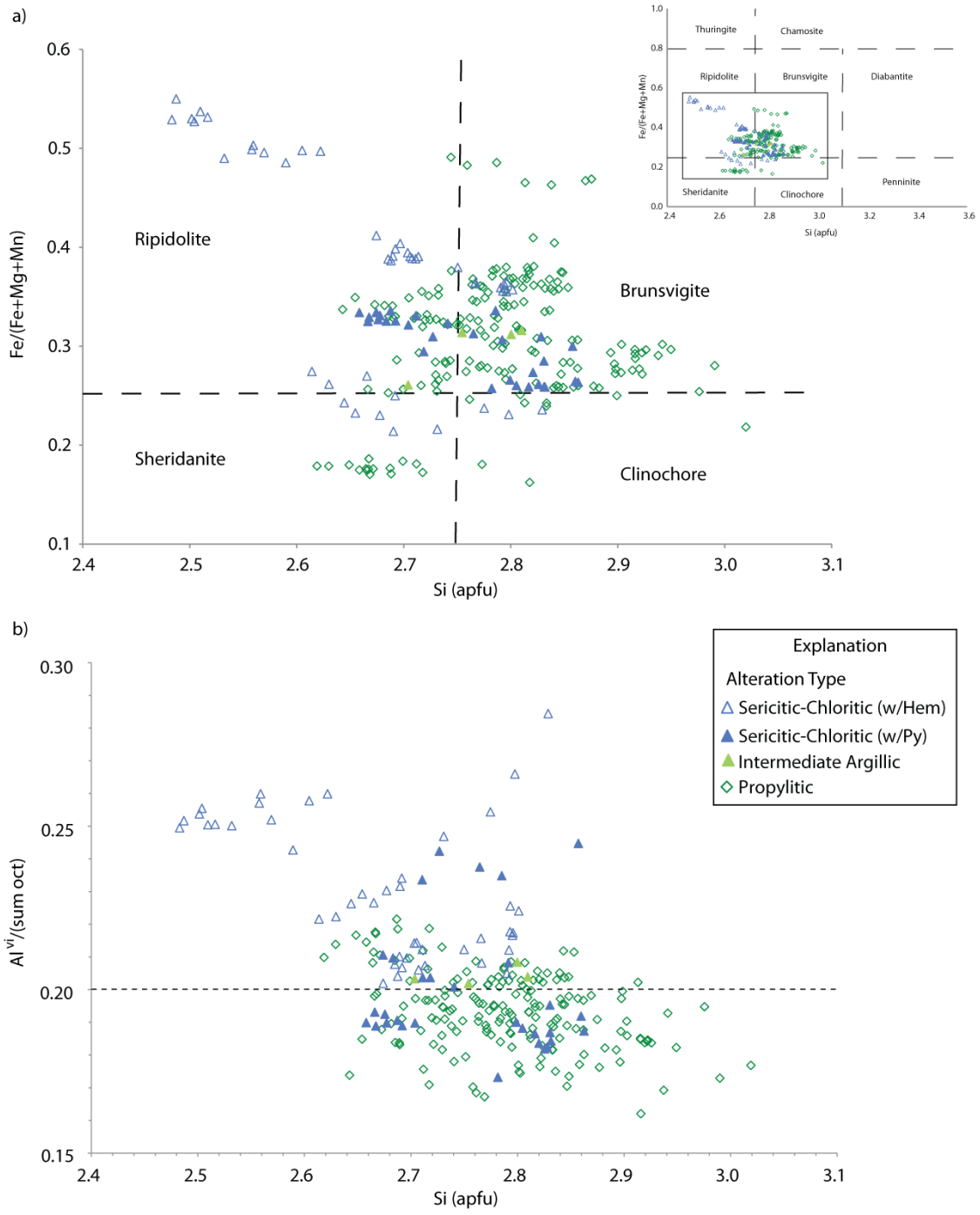

Figure 2.9. Compositional variation in chlorites: a) Si (apfu) vs. atomic Fe/(Fe+Mg+Mn), inset shows full range of possible chlorite compositions. Dashed lines represent chlorite species divisions according to Foster (1967). b) Si (apfu) vs. atomic Al^{vi}/(sum oct). The colors and shapes in represent hydrothermal alteration assemblages as in Table 2.5.

2.4.3 Short-wave infrared spectroscopy

The wide range of white mica species (muscovite, phengitic muscovite, illite, paragonite and pyrophyllite) detected by EMPA is reflected in the SWIR spectral data. Figure 2.10 shows spectra from samples containing white mica compositional end-members: muscovite, pyrophyllite, paragonite and illite. There is a significant difference in the scale of sampling by EMPA compared to SWIR spectroscopy. While each EMPA spot represents a ~5 µm diameter and deep spot on one mineral grain in a thin section or mounted rock chip, whereas the TerraSpec™ instrument analyses an ~1 cm diameter on the surface of a hand sample and inevitably contains multiple mineral phases not necessarily sampled by EMPA.

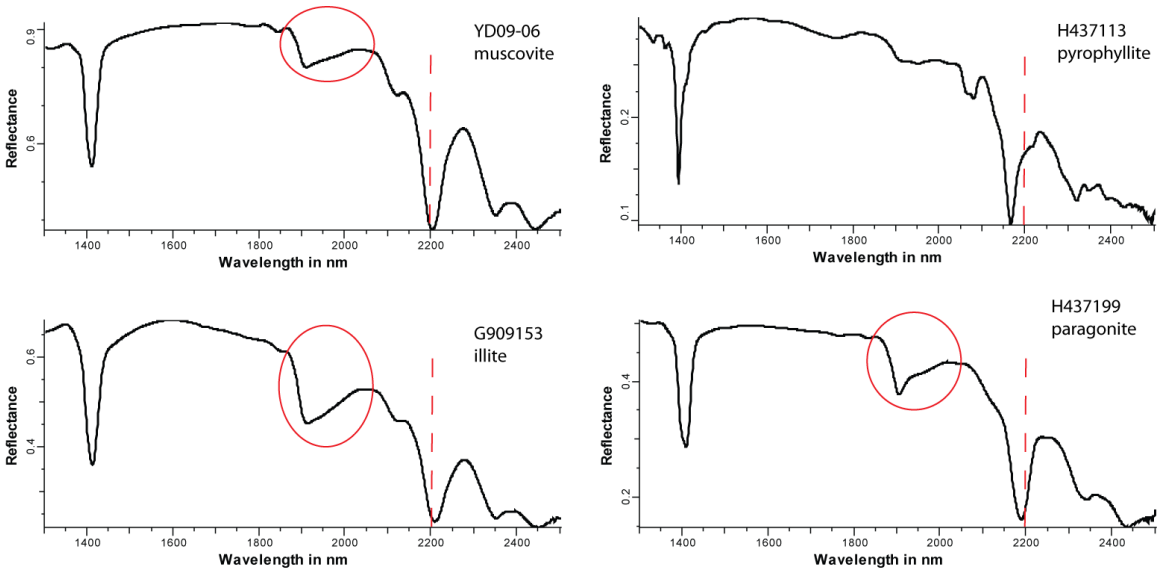

Figure 2.10. SWIR spectra from samples with end-member white mica/clay compositions as determined by analysis with EMPA: a) muscovite, b) pyrophyllite, c) ilite and d) paragonite. Red dashed lines mark position of ca. 2200 nm and red circles highlight ca. 1900 nm absorption feature.

Only samples identified as “sericite” or “pyrophyllite”, without any distinct kaolinite mineral SWIR features, are presented. The term “sericite” was used as a blanket term for white mica and illite in initial mineral determinations using TerraSpec™ software. The presence of minor amounts of clay minerals, such as kaolinite and

montmorillonite of very low temperature hydrothermal or supergene origin, complicate the interpretation of SWIR spectra. These clay minerals are present in many samples and have strong IR absorptions that obscure the hypogene white mica signature. Samples where kaolinite was identified by the doublets centered near ca. 1400 nm and ca. 2200 nm are excluded from the discussion section since the presence of kaolinite shifts the ca. 2200 nm absorption to the typical kaolinite value between 2206-2209 nm. Samples with deep ca. 1900 nm absorptions but no doublets were considered as "sericite" and included. Of the 25 samples analyzed, six (~ 25%) were identified by SWIR as "kaolinite", "sericite-kaolinite", or "epidote-kaolinite" and excluded from the data set.

Spectra from chlorite-bearing samples are shown in Figure 2.11. Due to the low-reflectivity of chlorite and its relatively low abundance relative to other alteration minerals (such as sericite, epidote and actinolite), chlorite-only spectra are rare (5% of samples). Chlorite was detected by SWIR spectroscopy in eight of twenty chlorite-bearing samples (40%) and almost always in combination with more reflective minerals such as sericite and kaolinite that obscure chlorite spectra.

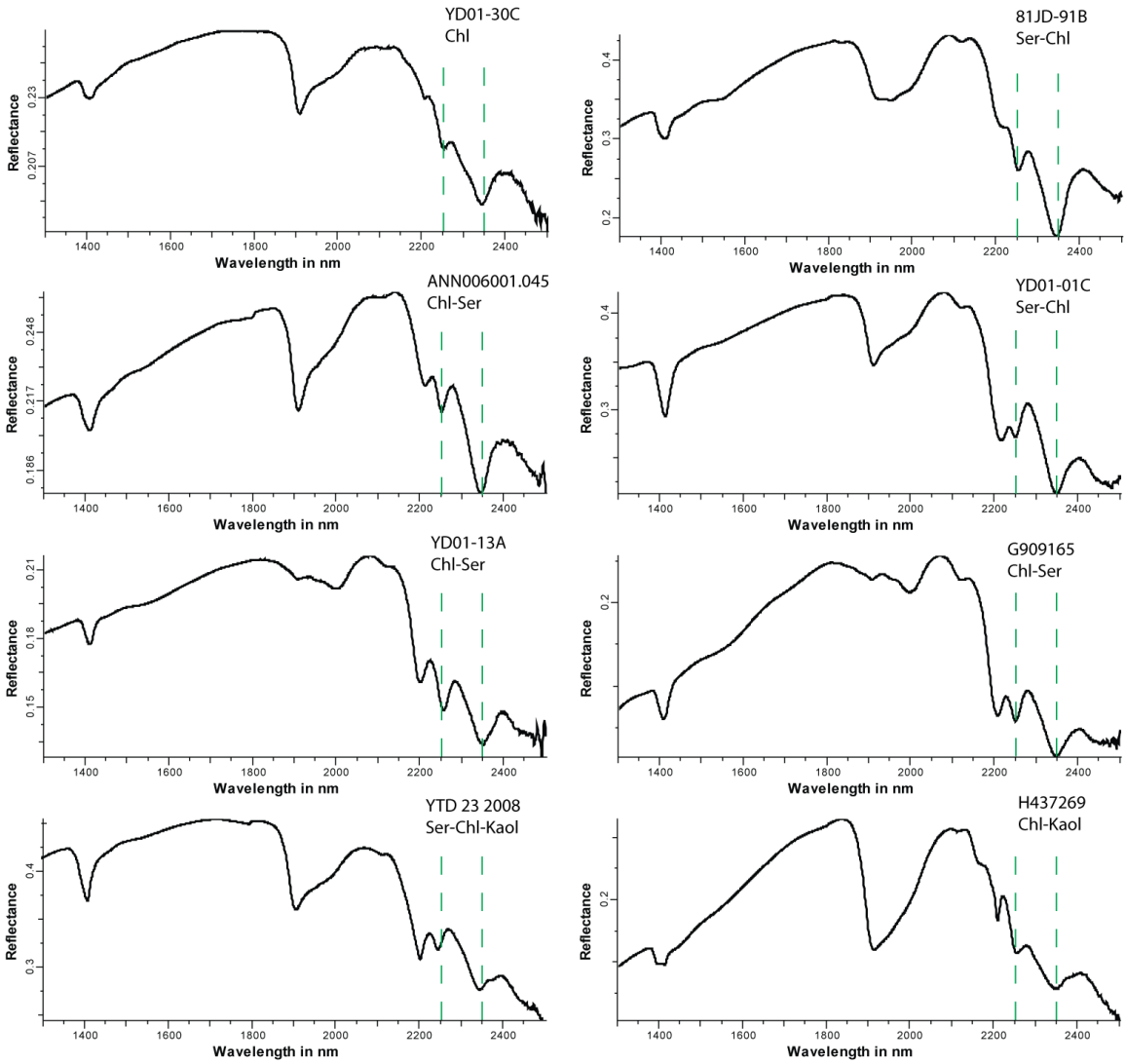

Figure 2.11. SWIR spectra from chlorite-bearing samples. Due to the low reflectivity of chlorite, most spectra are mixtures with sericite and/or kaolinite. Green dashed lines illustrate position of ca. 2250 nm and ca. 2350 nm.

2.5 Discussion

2.5.1 Comparison of SWIR spectra and mineral composition

2.5.1.2 White Mica and Illite

Fe+Mg+Mn (apfu) content in muscovite and illite, an indictor of phengitic substitution, is positively correlated (R=0.87) with wavelength of the ca. 2200 nm absorption in the SWIR spectra of samples identified as “sericite” (Figure 2.12). The

increase is linear and can be described using a least-squares regression method by the equation (2):

$$(2) \qquad y = 0.0172x - 37.6;\ R=0.87$$

where y = Fe+Mg+Mn (apfu), x = wavelength of the 2200 feature (nm).

For pure Al-muscovite, 2193 nm is the lowest wavelength commonly observed for the w2200 absorption (S. Halley, per. comm., 2011). When this value is set for the x-axis intercept, the equation for the correlation of phengite component with the w2200 absorption changes slightly to:

$$(3) \qquad y = 0.0223x - 49;\ R=0.83$$

Using equation (3), the approximate phengitic component of a white mica can be estimated using the measured wavelength of the 2200 nm feature.

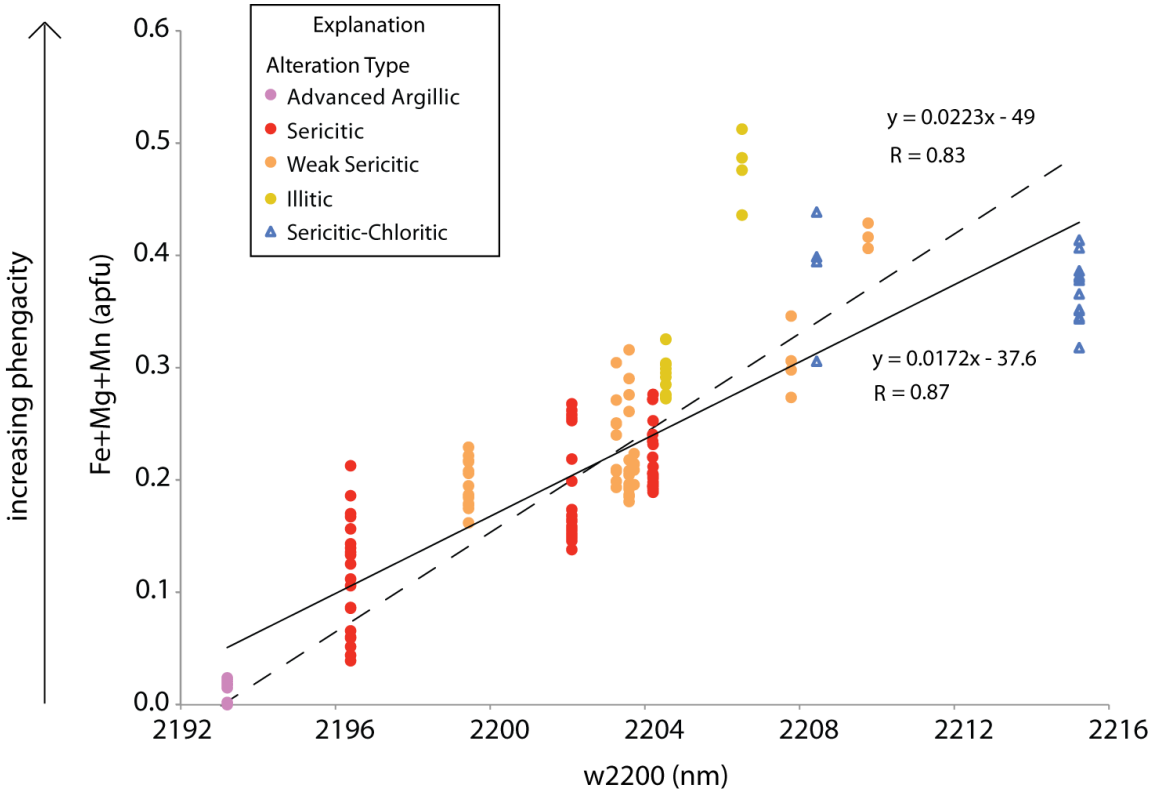

Figure 2.12. Fe+Mg+Mn (apfu) of muscovite and illite ("sericite") plotted against the wavelength of the ca. 2200 absorption (nm). The solid line represents the equation (eq. 2) derived by least squares linear regression. The dashed line represents linear regression equation adjusted to intersect the x-axis at s 2193 nm (eq. 3), the lowest common value for muscovite.

The relationship between atomic Fe+Mg+Mn and wavelength of the 2200 feature is also shown schematically in Figure 2.13. SWIR spectra are stacked according to the average atoms of Fe+Mg+Mn (apfu) in the white mica or illite ("sericite") in the sample.

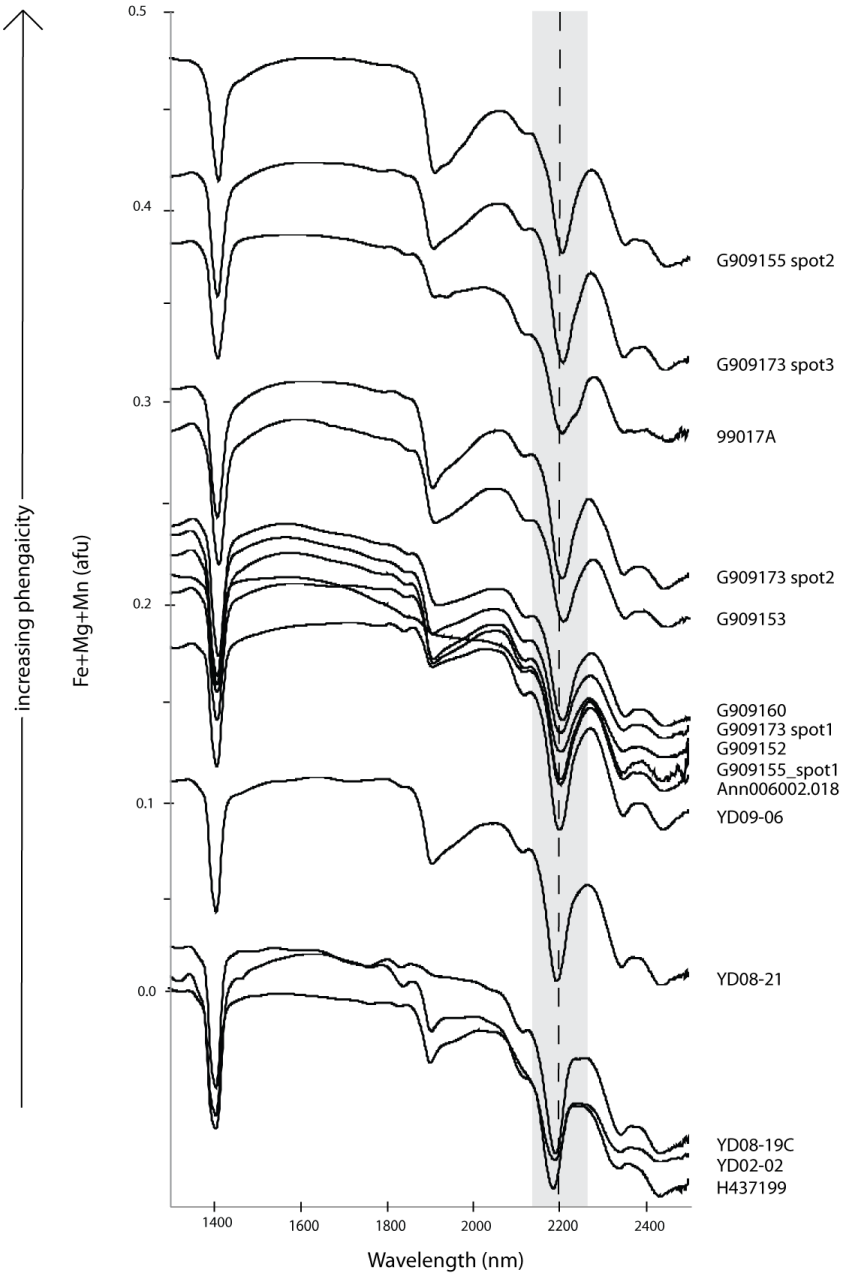

Figure 2.13. SWIR spectra from samples identified as "sericite" arranged by Fe+Mg+Mn (apfu) content demonstrating the shift in the wavelength of the ca. 2200 nm absorption feature with increasing phengitic component. The shaded area highlights ca. 2200 nm feature.

There is also a shift in the wavelength of the Al-OH absorption (ca. 2200 nm) associated with Na for K substitution in mica as shown in Figure 2.14a. End member paragonite has a w2200 value at ca. 2187 nm. As the proportion of muscovite in the sample decreases from X_{musc}=1.0 to X_{musc}=0.0, the wavelength of the ca. 2200 nm absorption feature decreases from 2193 to 2187 nm.

For this data set, illite and muscovite cannot be readily distinguished by SWIR spectroscopy. Illite has been identified as having a deeper H_2O absorption at ca. 1900 nm (Hauff et al., 1989; Davies, 2003). In Figure 2.14b, K+Na+2Ca (apfu) content is plotted against the depth of the ca. 1900 nm absorption (hqd1900). There is a weak correlation between K+Na+2Ca (apfu) content and the depth of the H_2O absorption (R= - 0.31). Figure 2.15 shows the SWIR spectra of "sericite" samples in a stacked plot arranged according to their K+Na+2Ca (apfu) content with muscovite at the top and illite at the bottom. Although all of the illite spectra have deep ca. 1900 nm absorptions, more than 50% of the muscovite spectra, as determined by EMPA, also have deep 1900 nm absorptions. This observation suggests the depth of the ca. 1900 nm absorption is not diagnostic of illite.

The absorption band at ca. 1900 nm, in combination with a sharp band at ca. 1400 nm, has been attributed to the presence of "undissociated water molecules in the mineral structure (i.e. water of hydration or water trapped in the lattice)" (Hunt and Salisbury, 1970). By definition, illite has no structural water and is a non-expandable clay (Deer et al., 1992). For this reason, a deeper absorption at ca. 1900 nm would not necessarily be predicted. Illite is often found with interlayered smectite, which is expandable and contains structural water. The presence of smectite in illite samples may account for the empirical derivation correlating a deeper ca. 1900 nm peak with illite (Hauff et al., 1989).

Due to the difference in sampling scale by EMPA and SWIR, the deep absorptions ca.1900 nm seen in samples with muscovite or illite is likely due to the presence of late low-temperature clay phases such as montmorillinite, smectite or halloysite clays. Although SWIR spectra were carefully screened to exclude samples with kaolinite, there is still the possibility of contamination by inconspicuous clay minerals. All clay minerals are highly reflective and can be detected in minute amounts by SWIR spectroscopy. Since these are natural samples from weathered exposures at the

earth' surface, the possible contamination of samples by clay species provides an example of realistic field sample variability.

There is a positive correlation (R=0.56) between the width of the ca. 2200 nm absorption feature and the interlayer cation site occupancy in atoms of K+Na+2Ca (Figure 2.14c). In previous studies, sharper absorption features at ca. 1400 and ca. 2200 nm are attributed to minerals with more ordered crystal structures (Kruse and Hauff, 1991; Pontual et al., 1995). Muscovite is generally slightly coarser-grained (Figure 2.7) and forms at higher temperature than illite (Figure 2.17). Therefore, the narrower peak would be hypothesized for muscovite. Our data show the opposite trend.

Figure 2.15 shows the SWIR spectra of "sericite" samples in a stacked plot arranged according to their K+Na+2Ca (apfu) content with muscovite at the top and illite at the bottom. Although all of the illite spectra have deep ca. 1900 nm absorptions, more than 50% of the muscovite spectra, as determined by EMPA, also have deep 1900 nm absorptions.

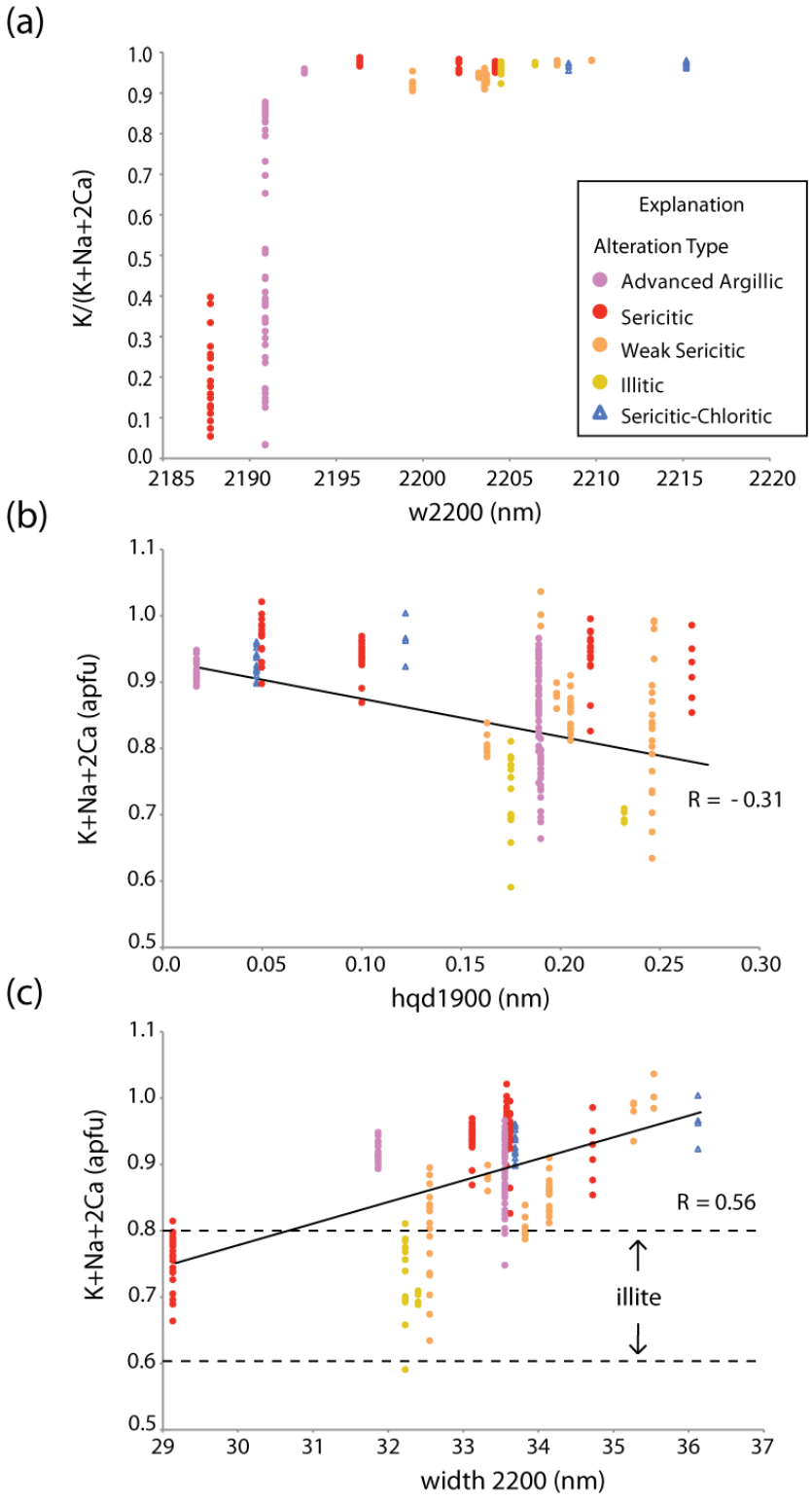

Figure 2.14. Compositional variations in white mica plotted against SWIR spectra absorption features: (a) w2200 vs. atomic K/(K+Na+2Ca), (b) hqd1900 vs. K+Na+2Ca (apfu) and (c) width 2200 vs. K+Na+2Ca (apfu).

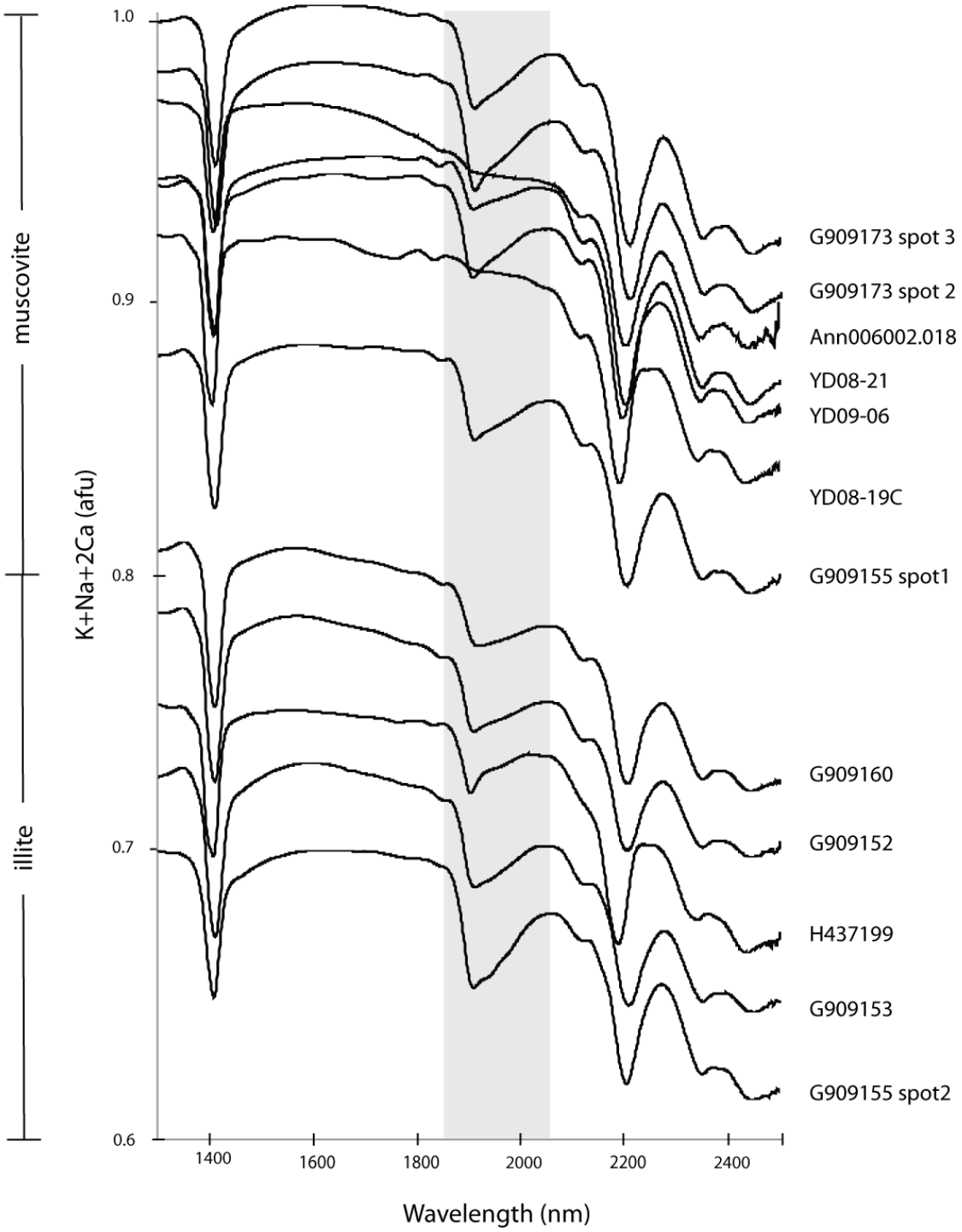

Figure 2.15. SWIR spectra from samples identified as "sericite" plotted according to the K+Na+2Ca (apfu) content. The shaded area highlights the 1900 nm feature. Samples with < 0.8 apfu are classified as illite. The depth of the ca. 1900 nm feature is an unreliable indicator of K+Na+2Ca (apfu) content.

2.5.1.2 Chlorite

The position of the ca. 2350 nm wavelength in the SWIR spectra of chlorite samples has been shown to decrease with increasing Fe content (Thompson et al., 1999). In this data set, there is poor linear correlation between in the wavelength of the ca. 2350 nm feature and the atomic Fe/(Fe+Mg+Mn) content (R=0.2). This is likely because most of spectra are mixtures of chlorite with sericite and/or kaolinite. Since chlorite is a dark mineral with low reflectivity, it is difficult to detect in low volumes (50-30 vol %) by SWIR spectroscopy. Sericite is highly reflective and has an absorption feature at ca. 2348 nm similar in size and shape to the Fe-OH and Mg-OH absorption features in chlorite (Table 2.4). It is likely the presence of sericite obscures the position of the ca. 2350 nm absorption related to chlorite composition.

There may be a relationship between aluminum and the wavelength of the 2350 nm feature since samples from sericitic-chloritic alteration have higher Al contents and lie on the right side of the graph with higher wavelengths of the 2350 nm feature. Alternatively, this is could also be due to interference of the chlorite spectra by sericite, which would be abundant in these samples. A different set of samples with greater proportions of chlorite and, without sericite or clays, is needed to further explore this hypothesis.

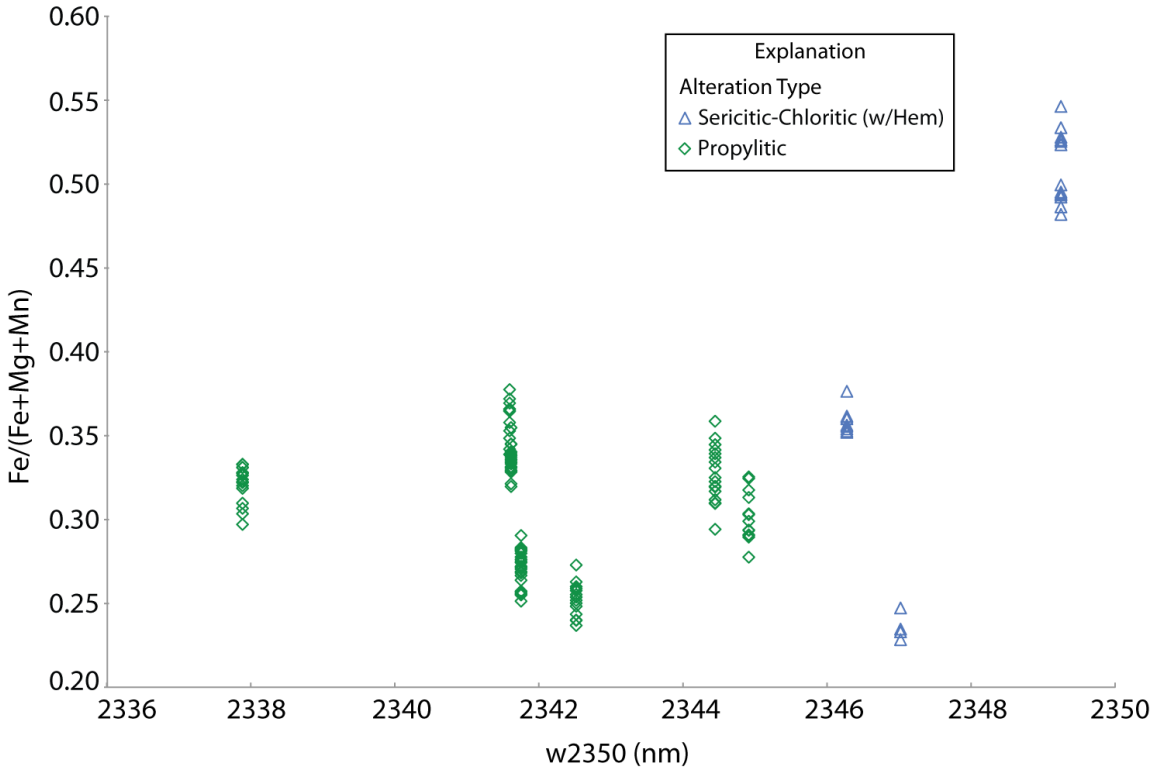

Figure 2.16. Mg/(Mg+Mn+Fe) plotted versus the wavelength of the 2350 feature (w2350) in chlorite spectra. There is no correlation (R=0.20) between the wavelength of the 2350 nm feature and atomic Mg/(Mg+Mn+Fe).

2.5.2 Conditions of Formation

Hydrothermal alteration assemblages identified in this study are plotted on the phase diagram for the K2O-Al2O3-SiO2-KCl-HCl-H2O system at 1.0 kb pressure with quartz present (Figure 2.17). Assemblages are plotted according to key alteration minerals in the system (Table 2.4) and, using this diagram, approximate temperatures and pH ($mKCl+K^+/mHCl+H^+$) conditions of formation are estimated (Figure 2.17). The inferences regarding formation conditions presented below are intentionally broad since they are based on only the stability of minerals containing both potassium and aluminum. There are many other factors that influence the stability of alteration minerals not considered here including changes in pressure and fluid geochemistry.

Based on the occurrence of pyrophyllite and the mixed pyrophyllite-muscovite assemblages, advanced argillic alteration from the western to northwestern portion of the Blue Hill fault block likely formed at moderate temperature between 280-400 °C at low

activity ratio of K^+/H^+ activity, i.e. at acidic conditions. Muscovite is stable at similar temperatures but higher K^+/H^+ values than pyrophyllite, which indicates less acidic formation conditions for sericitic alteration (Figure 2.17).

Weak sericitic alteration and sericitic-chloritic alteration, where feldspar is relic, may form at the same time and temperature as strong sericitic alteration with pervasive quartz-muscovite replacement but further from main fluid flow paths represented by "D" veins based on the field observations. The fluid to rock ratio is lower further from the vein allowing a higher buffering capacity by plagioclase and K-feldspar and, therefore, higher K^+/H^+ conditions (Dilles et al., 2000). The sample of sericitic-chloritic alteration without relic feldspar (YD01-13A, Appendix A) is hosted in the Artesia Lake andesite. This is a more mafic unit (~51 wt% SiO2 in Artesia Lake basalt) than the rocks of the Yerington batholith (~58 – 69 wt% SiO2) (Dilles, 1987) with higher proportions of mafic minerals more likely to alter to chlorite-muscovite mixtures by alteration by acidic fluids.

According to Reyes (1990), illite is stable from 220 to 310° C. Based on the lower temperature stability of illite compared to muscovite, illitic and illitic-chloritic alteration events where illite is the primary alteration mineral must represent cooler younger hydrothermal alteration events than the adjacent sericitic alteration. Illitic and illitic-chloritic alteration have assemblages with illite and relict K-feldspar that plot along the border between the illite and K-feldspar stability fields (Figure 2.17). These alteration types form at a lower fluid to rock ratio (higher K^+/H^+) and occur at lower temperatures than neighboring sericitic alteration.

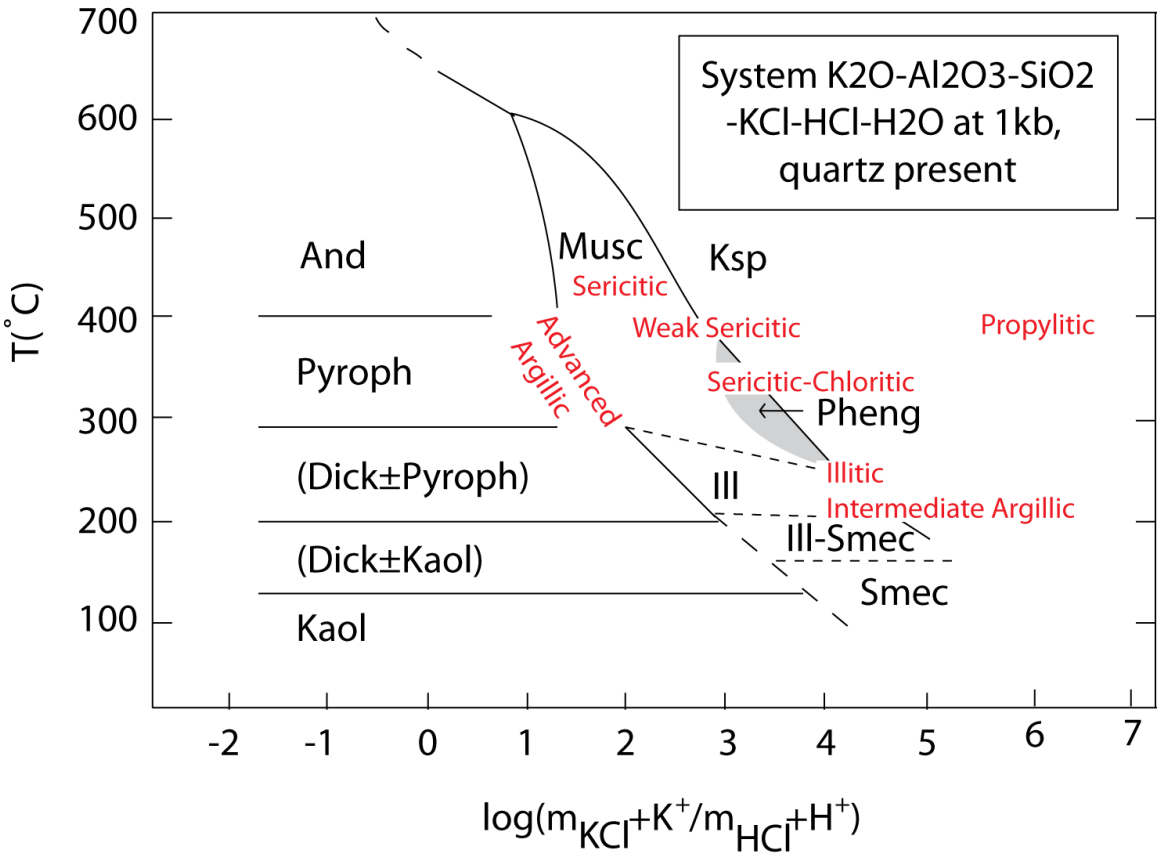

Figure 2.17. Phase diagram for the K2O-Al2O3-SiO2-KCl-HCl-H2O system at 1.0 kbar with quartz present with hydrothermal alteration assemblages plotted as a function of K^+/H^+ versus temperature (°C). Modified from Hemley (1959) and Dilles et al., (in press).

Chlorite from sericitic-chloritic alteration with hematite (muscovite-chlorite-hematite) is generally more aluminous than similarly altered samples with pyrite or chlorite from propylitic alteration (Figure 2.9). Samples from muscovite -chlorite-hematite assemblage were collected from exposures of the upper portion of the hydrothermal system above ~ 1 km paleodepth while samples with muscovite -chlorite-pyrite were collected from deeper portions of the system in drill core and western Ann-Mason, closer to the ore body and the path of the magmatic hydrothermal plume (Dilles et al., 2000). The aluminum content of chlorite increases with alteration by low pH fluids (addition of H^+) as shown by the reaction of clinochlore (Mg-rich chlorite) to sudoite (Al-rich chlorite) in equation (4).

(4) $2Mg_5Al^{vi}(Al^{iv}Si_3)O_{10}(OH)_8$ (clinochlore) + $16H^+$ <-> $Mg_2Al_3{}^{vi}(Al^{iv}Si_3)O_{10}(OH)_8$ (sudoite) + SiO_2 + $8Mg^{2+}$ + $12H_2O$

Chlorites with higher aluminum contents from the muscovite-chlorite-hematite assemblage likely formed by interaction of late-stage lower temperature and lower pH fluids of similar composition but higher pH do the presence of phengitic muscovite that formed nearby sericitic alteration. This is further evidence for a magmatic-hydrothermal origin for sericite-chlorite-hematite alteration as proposed in Dilles et al. (2000) and Lipske (2002). The lower Al content of samples from sericitic-chloritic alteration with pyrite may be related to their position relative to the ore body and the pathway of magmatic-hydrothermal fluids. The presence of phengitic muscovite and pyrite in these samples suggest they were also formed by interaction with magmatically-derived fluids but the lower Al content suggests these fluids were higher temperature and, therefore, slightly higher pH. This may relate to the relative position of these samples since fluids closer to the ore body would be higher temperature.

2.5.3 Mapping of pH gradients using SWIR

White mica and chlorite mineral compositions become more aluminous through alteration with acidic fluids (addition of H^+) also shown in Figure 2.17 where the proportion of Al in the mineral structure increases with decreasing K^+/H^+ ratios and as illustrated by the reaction of phengitic muscovite to muscovite (5):

(5) $2K(Fe,Mg)_{0.5}Al_{1.5}{}^{vi}Al_{0.5}{}^{iv}Si_{3.5}O_{10}(OH)_2$ (phengitic muscovite) + 8H+ + Al_2O_3 <-> $2KAl_2{}^{vi}Al^{iv}Si_3O_{10}(OH)_2$ (muscovite) + $(Fe,Mg)^{2+}$ + SiO_2 + $5H_2O$

Results from this study demonstrate SWIR spectroscopy can be used to identify changes in the total Al (apfu) content of muscovite, which correlates to increasing Fe+Mg+Mn (apfu) through to the Tschermak substitution, using the wavelength of the 2200 nm feature. Since aluminum content can be related to the pH of formation fluids,

SWIR spectroscopy may be used to map fluid pH gradients in rocks from sericitic alteration (muscovite-bearing assemblages).

2.6 Conclusion

Muscovite, illite, paragonite, pyrophyllite and chlorite from the Yerington district, Nevada were analyzed for major element compositions using EMPA and compared to corresponding SWIR spectra to determine if SWIR spectroscopy can be used to map compositional variations in hydrothermal white mica and chlorite. Results show the increase in the wavelength of the Al-OH absorption band at ~2200 nm in muscovite and illite can be attributed to the Tschermak substitution and a decrease in the wavelength of the Al-OH absorption band to values below 2193 nm caused by the presence of paragonite. Although illite has been previously identified by a deep H_2O absorption at ~1900 nm, our study finds this feature is not unique to illite and >50% of samples with muscovite also have a similar feature. Since neither illite nor muscovite contain structural water, the deep absorption at ca. 1900 nm seen in the SWIR spectra likely indicates the presence another clay mineral, such a smectite or montmorillonite. Chlorite compositional variations could not be identified in short wave infrared spectra of rocks and were likely obscured by coexisting highly reflective clays and micas. The results of this demonstrate SWIR spectroscopy can be used to identify fluid pH gradients in rocks from sericitic alteration (muscovite-bearing assemblages) by using the wavelength of the 2200 nm feature to detect increases in the aluminum content of micas caused by alteration with acidic fluids (addition of H^+). This study strengthens the hypotheses presented by previous researchers (e.g. Duke, 1994; Yang et al., 2000) and may assist field geologists using SWIR spectroscopy in identifying zoned hydrothermal alteration, which, in combination with other exploration techniques, can be used as a vector for ore deposit exploration.

2.7 References

Bailey, S., 1984, Micas, Chelsea, Mineralogical Society of America, Reviews in Mineralogy.

Carrillo-Rosua, J., Morales-Ruano, S., Esteban-Arispe, I., and Hach-Ali, P. F., 2009, Significance of Phyllosilicate Mineralogy and Mineral Chemistry in an Epithermal Environment. Insights from the Palai-Islica Au-Cu Deposit (Almeria, Se Spain): Clays Clay Miner., v. 57, no. 1, p. 1.

Carten, R., 1986, Sodium-calcium metasomatism; chemical, temporal, and spatial relationships at the Yerington, Nevada, porphyry copper deposit: Economic Geology, v. 81, no. 6, p. 1495.

Changyun, L., Ge, Z., and Chunhua, Y., 2005, Application of SWIR reflectance spectroscopy to the Pulang porphyry copper deposit, Yunnan, China: Mineral Deposits (Kuangchuang Dizhi), v. 24, no. 6, p. 621-637.

Clark, R. N., Swayze, G. A., Wise, R. A., Livo, K. E., Hoefen, T. M., Kokaly, R. F., and Sutley, S. J., 2007, USGS digital spectral library splib06a, Reston, U. S. Geological Survey, U. S. Geological Survey Data Series.

Deer, W. A., Howie, R. A., and Zussman, J., 1992, An introduction to the rock-forming minerals, Essex, Pearson Education Limited.

Di Tommaso, I., and Rubinstein, N., 2007, Hydrothermal alteration mapping using ASTER data in the Infiernillo porphyry deposit, Argentina: Ore Geology Reviews, v. 32, no. 1-2, p. 275-290.

Dilles, J. H., and Einaudi, M., 1992, Wall-rock alteration and hydrothermal flow paths about the Ann-Mason porphyry copper deposit, Nevada; a 6-km vertical reconstruction: Economic Geology, v. 87, no. 8, p. 1963.

Dilles, J. D., Proffett, J. M., and Einaudi, M. T., 2000, Magmatic and hydrothermal features of the Yerington batholith with emphasis on the porphyry Cu(Mo) deposit in the Ann-Mason area: Society of Economic Geologist Guidebook Series, v. 32, p. 67-89.

Dilles, J. H., 1987, Petrology of the Yerington Batholith, Nevada; evidence for evolution of porphyry copper ore fluids: Economic Geology, v. 82, no. 7, p. 1750.

Dilles, J. H., and Gans, P. B., 1995, The chronology of Cenozoic volcanism and deformation in the Yerington area, western Basin and Range and Walker Lane: Geological Society of America Bulletin, v. 107, no. 4, p. 474-486.

Dilles, J. H., and Wright, J. E., 1988, The chronology of early Mesozoic arc magmatism in the Yerington District of western Nevada and its regional implications: Geological Society of America Bulletin, v. 100, no. 5, p. 644-652.

Duke, E., 1994, Near infrared spectra of muscovite, Tschermak substitution, and metamorphic reaction progress: Implications for remote sensing: Geology, v. 22, no. 7, p. 621.

Einaudi, M., 1977, Petrogenesis of copper-bearing skarn at Mason Vally Mine, Yerington District, Nevada: Economic Geology, v. 72, no. 5, p. 769-795.

Gustafson, L., and Hunt, J., 1975, The porphyry copper deposit at El Salvador, Chile: Economic Geology, v. 70, no. 5, p. 857.

Hauff, P., 2002, Identification of illite polytype zoning in disseminated gold deposits using reflectance spectroscopy and X-ray diffraction-potential for mapping with imaging: Geoscience and Remote Sensing.

Hauff, P. L., Kruse, F. A., and Madrid, R. J., 1989, Gold Exploration Using Illite Polytypes Defined By X-Ray Diffraction and Reflectance Spectroscopy: World Gold, p. 76-82.

Herrmann, W., Blake, M., Doyle, M., Huston, D., Kamprad, J., Merry, N., and Pontual, S., 2001, Short wavelength infrared (SWIR) spectral analysis of hydrothermal alteration zones associated with base metal sulfide deposits at Rosebery and Western Tharsis, Tasmania, and Highway-Reward, Queensland: Economic Geology, v. 96, no. 5, p. 939.

Herrmann, W., Green, G. R., Barton, M. D., and Davidson, G. J., 2009, Lithogeochemical and stable isotopic insights into submarine genesis of pyrophyllite-altered facies at the Boco Prospect, western Tasmania: Economic Geology, v. 104, no. 6, p. 775.

Hunt, G. R., and Ashley, R. P., 1979, Spectra of altered rocks in the visible and near infrared: Economic Geology, v. 74, no. 7, p. 1613.

Jones, S., Herrmann, W., and Gemmell, J. B., 2005, Short Wavelength Infrared Spectral Characteristics of the HW Horizon: Implications for Exploration in the Myra Falls Volcanic-Hosted Massive Sulfide Camp, Vancouver Island, British Columbia, Canada: Economic Geology, v. 100, no. 2, p. 273.

Kruse, F. A., and Hauff, P. L., 1991, Identification of illite polytype zoning in disseminated gold deposits using reflectance spectroscopy and X-ray diffraction-potential for mapping with imaging spectrometers: Geoscience and Remote Sensing, IEEE Transactions on, v. 29, no. 1, p. 101-104.

Lipske, J., 2002, Advanced argillic and sericitic alteration in the Buckskin Range, Nevada: a product of ascending magmatic fluids from the deeper yerington porphyry copper environment [M.S.: Oregon State University].

Lipske, J., and Dilles, J., 2000, Advanced argillic and sericitic alteration in the subvolcanic environment of Yerington Porphyry Copper System, Buckskin Range, Nevada: Part I. Contrasting Styles of Intrusion-Associated Hydrothermal Systems, v. 32, p. 91-99.

Lowell, J., and Guilbert, J., 1970, Lateral and vertical alteration-mineral zoning in porphyry ore deposits: Economic Geology, v. 65, no. 4, p. 373-408.

Martinez-Alonso, S., 2000, Study of the infrared spectra of phyllosilicates through direct measurements, quantum mechanical modeling, and analysis of AVIRIS imaging spectrometer data: Relationships with environment of mineralization [PhD: University of Colorado, p. 1-232].

Merry, N., and Pontual, S., 1999, Rapid alteration mapping using portable infrared spectrometers: PACRIM '99 Bali, Indonesia, p. 693-698.

Meyer, C., and Hemley, J. J., 1967, Wall Rock Alteration: Geochemistry of Hydrothermal Ore Deposits (Book), p. 166-235.

Newman, A., 1987, Chemistry of Clays and Clay Minerals, New York, John Wiley & Sons, Mineralogical Society Monograph.

Paulick, H., and Bach, W., 2006, Phyllosilicate alteration mineral assemblages in the active subsea-floor Pacmanus hydrothermal system, Papua New Guinea, ODP Leg 193: Economic Geology, v. 101, no. 3, p. 633.

Pontual, S., Merry, N., and Cocks, T., 1995, Field-based alteration mapping using the PIMA: PACRIM Congress 1995 : Auckland, New Zealand, 19-22 November 1995 : proceedings of the 1995 PACRIM Congress.

Post, J. L., and Noble, P. N., 1993, The near-infrared combination band frequencies of dioctahedral smectites, micas, and illites: Clay Clay Miner, v. 41, p. 639-639.

Pouchou, L. J., and Pichoir, F., 1984, New model quantitative x-ray microanalysis, Application to the analysis of homogeneous samples: Research in Aerospace, v. 3, p. 13-38.

Proffett, J. M., 1977, Cenozoic geology of the Yerington District, Nevada, and implications for nature and origin of Basin and Range faulting: Geological Society of America Bulletin, v. 88, no. 2, p. 247-266.

Proffett, J. M., and Dilles, J. D., 1984, Geologic map of the Yerington District, Nevada, Nevada Bureau of Mines and Geology.

Rose, A. W., 1970, Zonal relations of wallrock alteration and sulfide distribution at porphyry copper deposits: Economic Geology, v. 65, no. 8, p. 920.

Seedorff, E., Dilles, J. H., Proffett, J. M., Jr., Einaudi, M. T., Zurcher, L., Stavast, W. J. A., Johnson, D. A., and Barton, M. D., 2005, Porphyry deposits; characteristics and origin of hypogene features: Economic Geology 100th Anniversary Volume, p. 251-298.

Serratosa, J. M., and Bradley, W. F., 1958, Determination of the orientation of OH bond axes in layer silicates by infrared absorption: The Journal of Physical Chemistry, v. 62, no. 10, p. 1164-1167.

Stubican, V., and Rustum, R., 1961, Isomorphous substitution and infra-red spectra of the layer lattice silicates: American Mineralogist, v. 46, p. 32-51.

Sun, Y., Seccombe, P. K., and Yang, K., 2001, Application of short-wave infrared spectroscopy to define alteration zones associated with the Elura zinc-lead-silver deposit, NSW, Australia: Journal of Geochemical Exploration, v. 73, no. 1, p. 11-26.

Swayze, G. A., 1997, The hydrothermal and structural history of the Cuprite mining district, southwestern Nevada; an integrated geological and geophysical approach [Doctoral: University of Colorado, Boulder].

Thompson, A. J. B., Hauff, P. L., and Robitaille, A. J., 1999, Alteration Mapping in Exploration: Application of Short-Wave Infrared (SWIR) Spectroscopy: SEG Newsletter, v. 39, p. 1-13.

Tschermak, G., 1890, Die chloritgruppe, I. Theil, Sitzungsber.: Akad. Wiss. Wien, Math-naturwiss, Kl., v. 1, no. 99, p. 174-278.

-, 1891, Die chloritgruppe, II. Theil, Sitzungsber.: Akad. Wiss. Wien, Math-naturwiss, Kl., v. 1, no. 100, p. 29-107.

Tuddenham, W., and Lyon, R., 1960, Infrared techniques in the identification and measurement of minerals: Analytical Chemistry, v. 32, no. 12, p. 1630-1634.

Vedder, W., 1964, Correlations between infrared spectrum and chemical composition of mica: The American Mineralogist, v. 49, no. May-June, p. 736-768.

Vedder, W., and McDonald, R., 1963, Vibrations of the OH ions in muscovite: The Journal of Chemical Physics, v. 38, p. 1583.

Yang, K., Browne, P., Huntington, J., and Walshe, J., 2001, Characterising the hydrothermal alteration of the Broadlands-Ohaaki geothermal system, New Zealand, using short-wave infrared spectroscopy: Journal of Volcanology and geothermal research, v. 106, no. 1-2, p. 53-65.

Chapter 3: Trace metal zonation at the Ann-Mason porphyry copper deposit, Nevada

Julia F. Cohen[1], John H. Dilles[2], Scott Halley[3] and Richard Tosdal[4]

3.1 Abstract

Trace metal zonation patterns in wall-rock alteration related to the formation of porphyry-Cu deposits have been used in ore exploration for almost a century. Modern ICP-MS and ICP-AES analyses can detect concentrations of less abundant trace metals (e.g. Te, Se, Bi) at levels below crustal abundance (<0.1 ppm) and subtle changes in wall-rock zones can now be mapped.

In order to verify trace metal gradients measured in altered rock are related to ore fluids, mineral hosts must be determined. Trace metal concentrations in altered rock from exposures surrounding the Ann-Mason porphyry-Cu(Mo) deposit in the Yerington district, Nevada are measured using inductively coupled plasma-mass spectrometry and atomic emission spectroscopy (ICP-MS/AES) with 4-acid digest. Results are compared to trace element contents of hydrothermal white mica, illite and chlorite determined by laser ablation-inductively coupled plasma-mass spectrometry (LA-ICP-MS). This is an ideal location for this study since the vertical and lateral position relative to the ore center is easily constrained as the Yerington district has been tilted ~90°W by Basin and Range extension exposing a cross-section through a porphyry-Cu deposit from the volcanic surface environment to 7 km paleodepth.

Copper, Mo, Te, Se, Bi, Sb, As, W, Sn, Li and Tl are enriched rocks from the zone of potassic, sericitic and shallow-level advanced argillic alteration that represents the near-vertical pathway of magmatic fluid from the ore zone (3.5 km depth) to the

---

[1] M.Sc. Candidate, Department of Geosciences, Oregon State University, Corvallis, OR
[2] Professor, Department of Geosciences, Oregon State University, Corvallis, OR
[2] Professor, Department of Geosciences, Oregon State University, Corvallis, OR
[3] Mineral Mapping, Inc.
[4] Mineral Deposit Research Unit, University of British Columbia, Vancouver, B.C., Canada

paleosurface. Of these elements, W, Sn and Tl enrichment can be attributed, at least partially, to increased concentrations in muscovite and illite, which are also enriched in alkali and alkali earth elements (Cs, Rb, Ba). The pattern of Li enrichment can be attributed to increased concentrations in chlorite and to differences in wall-rock lithology above 1 km depth. Zinc, Mn, Co and Ni are depleted in altered rock below, lateral to, and above the ore zone by both magmatic-hydrothermal ore fluids and by circulating sedimentary brines as a results of destruction of igneous mafic minerals (hbl, px, biot, mag) by both potassic and sericitic alteration as well as sodic-calcic alteration. Magmatic fluids deposit anomalous Zn±V±Mn in some chlorites in the <2 km depth environment. Non-magmatic brines transport metals (Mn, V, Zn) to distal/upper propylitic alteration zones as verified by gradients in chlorite compositions. Chalcophile elements Mo, As, Te, Se, Bi are rarely detected in white mica/illite or chlorite in concentrations greater than 1 ppm and more than 50% of analyses are commonly below detection.

3.2 Introduction

Ore deposit exploration has used the zonation of metals (e.g. Cu, Au, Ag) and closely associated trace elements (e.g. Hg, As) in bulk rock chemistry as a vector for mineralization since the 1920s. Emmons (1918) identified a common sequence of metal distribution observed in hydrothermal ore deposits that was refined by Guilbert and Park (1986) where Mo, W and Sn precipitate at deeper levels followed by Cu, As, Sb, Zn, Pb, Mn, Ag moving toward the paleosurface and volatile metals Au, Sb and Hg enriched in the shallow epithermal environment. This model applies best at deposits where metals are transported in the hydrothermal fluid as metal-sulfide complexes. If transport occurs by metal-chloride complexes then the sequence Cu, Ag, Pb, Zn is often observed (Barnes, 1975). Although these patterns apply as broad generalizations, factors controlling metal precipitation are complex and vary depending on many factors including the metal content and composition of fluids, fluid temperature and redox conditions.

In the last decade, analytical techniques for measuring trace element concentrations in bulk rock samples have dramatically improved prompting researchers to reexamine classic zonation patterns. Until recently, the measurement of trace metal contents in rock compositions at quantities below, or near, crustal abundances of

elements that occur in low concentrations in the earth's crust (Te, Se, Bi, Sb, Tl <0.5 ppm) was nearly impossible and prohibitively expensive on a district scale. Due to advances in analytical technology, most trace elements can now be detected at concentrations less than crustal abundances (<0.1 ppm) allowing for study of subtle changes in wall-rock trace metal chemistry associated with ore deposit formation.

In order to correctly interpret changes in the trace element chemistry of rocks that have seen multiple alteration events, mineral hosts must be determined. Hydrothermal phyllosilicates such as biotite, muscovite and chlorite are common alteration minerals associated with porphyry-type deposits and essential for identifying and interpreting alteration. Biotite is a common igneous mineral and hydrothermal biotite is an index mineral for potassic alteration that often occurs in zones of Cu(Mo)-sulfide enrichment. Due to its association with ore, variations in the trace metal contents (Cu, Zn, Ni, Co, Pb) of biotite have been studied at several porphyry copper centers (Ford, 1978) including the Ann-Mason porphyry-Cu(Mo) deposit at Yerington, Nevada (Dilles and Proffett, 1995). Trace element analyses of chlorite and white mica from the literature on porphyry-type deposits are rare (Ford, 1978) and there are no publications focused solely on the trace element contents of these minerals.

Trace element contents of muscovite and chlorite have been studied in other ore systems. Variations in the trace element composition of muscovite have been determined in research on rare earth element mineralization in pegmatites (Van Lichtervelde et al., 2008) and chlorite and interstratified clay minerals have been identified as trace metal hosts in the regolith of massive sulfide deposits (Le Gleuher et al., 2008).

This research contributes to the existing literature by studying gradients in the trace metal chemistry in altered rocks and common hydrothermal alteration minerals (muscovite, illite and chlorite) to link trace element anomalies detected by bulk rock analyses to alteration formed by the magmatic hydrothermal plume surrounding the Ann-Mason porphyry-Cu(Mo) deposit in the Yerington district, Nevada. The Yerington district, Nevada, provides a natural laboratory to examine trace element zonation associated with porphyry-Cu systems since Basin and Range extension and tilting has exposed a crustal cross section from ~ the bear surface to ~6 km paleodepth (Proffett, 1977; Proffett and Dilles, 1984). In addition, wall-rock alteration and the hydrothermal

system at have been well-studied (Dilles, 1987; Dilles and Einaudi, 1992; Dilles et al., 2000) and a model for the origin and sequence of observed alteration assemblages has been developed based on field mapping, petrology, fluid inclusion data and stable isotopes (Dilles et al., 2000) (see Chapter 1 for more detail).

The purpose of this study is to (1) determine and compare the distribution of trace elements in altered rock and minerals (muscovite, illite, pyrophyllite and chlorite) from samples surrounding the Ann-Mason porphyry-Cu(Mo) deposit, (2) evaluate contributions from muscovite and chlorite to rock chemistry using a simplified mass balance method and (3) compare trace elements gradients in rock and minerals to confirm anomalous elements in rock chemistry track the magmatic plume. This study is an extension of preliminary research conducted by coauthors John Dilles, Richard Tosdal and Scott Halley.

3.3 Methods

3.3.1 Sample collection

A set of 568 surface samples and 50 drill core chip samples were collected from exposures surrounding the Ann-Mason porphyry-Cu(Mo) deposit and from drill core provided by PacMag Metals Ltd and the Anaconda Mining Company. Thirty-four surface samples and five drill core samples were selected for mineral analysis. Sample collection focused on altered rocks throughout the exposed crustal column. Samples were described and assigned lithologies in the field based on Proffett and Dilles (1984) and Dilles (1987). All samples are igneous rocks of similar composition (SiO_2 = 54 to 68 wt.%) taken from the Middle Jurassic Yerington batholith and closely related Artesia Lake and Fulstone Spring Volcanics (Dilles, 1987).

Sample locations are plotted on a simplified geology map in Figure 3.1 and on a reconstructed Jurassic cross-section in Figure 3.2. Data from previous reconstructions by Proffett (1977), Proffett and Dilles, (1984) and Dilles et al., (2000) were used to restore sample locations to their relative position in the Jurassic cross section (Figure 3.2). In summary, each fault block was restored to remove tilting 70-90° W and sample coordinates in the Blue Hill fault block were adjusted to remove displacement along the Blue Hill and Singatse faults. In addition, the Blue Hill and Ann-Mason fault blocks

were restored to their original positions by matching geologic features including the location of the Ann-Mason dike swarm and the contact between the batholith and the overlying Artesia Lake volcanics. The section in the Buckskin Range was shortened to ~ 1 km thick and placed arbitrarily on top of the Blue Hill fault block.

Samples were collected from the Ann-Mason, Blue Hill and central Buckskin Range fault blocks. The Ann-Mason fault block contains exposures representing ~1 to 5.5 km paleodepth and hosts most of the Ann-Mason Cu(Mo) deposit (Dilles and Einaudi, 1992). At Ann-Mason deposit, the ore zone is concealed beneath 200 m of Tertiary volcanic rocks that lie in the hanging wall of the Singatse Fault and can only be sampled in drill core. Exposures in the Blue Hill fault block represent ~0.5 to 3 km paleodepth that have been mapped by Dilles (unpublished, 1:12,000). Samples from the central Buckskin Range represent the shallow epithermal environment from the surface to 1 km paleodepth as mapped by Lipske (2002). It is important to note that exposures in the Buckskin Range are 1-2 km further west than the predicted location of the epithermal environment related to the Ann-Mason porphyry center and likely represent the upper ~ 1km of a different porphyry center in the western Yerington district.

The same mineral sample set was analyzed by electron microprobe analysis (EMPA) and LA-ICP-MS. Sample locations for mineral analyses are shown as yellow circles on the simplified geologic map in Figure 3.1 and in the reconstructed paleocross-section in Figure 3.2. In some cases, one mineral grain was used for both analytical techniques. In other examples, due to the fine-grain nature of the hydrothermal micas, different mineral grains from the same hand sample were analyzed by each technique. Samples with white mica were selected from D-vein selvages (Gustafson and Hunt, 1976) in the zone of sericitic alteration that records the pathway of magmatic fluids. Samples with chlorite were selected from sericitic-chloritic alteration (chl-musc-hem and chl-musc-py assemblages) attributed to alteration by fluids with a magmatic component. Distal to the ore zone, chlorite samples were selected from propylitic alteration with assemblages where actinolite and epidote are added.

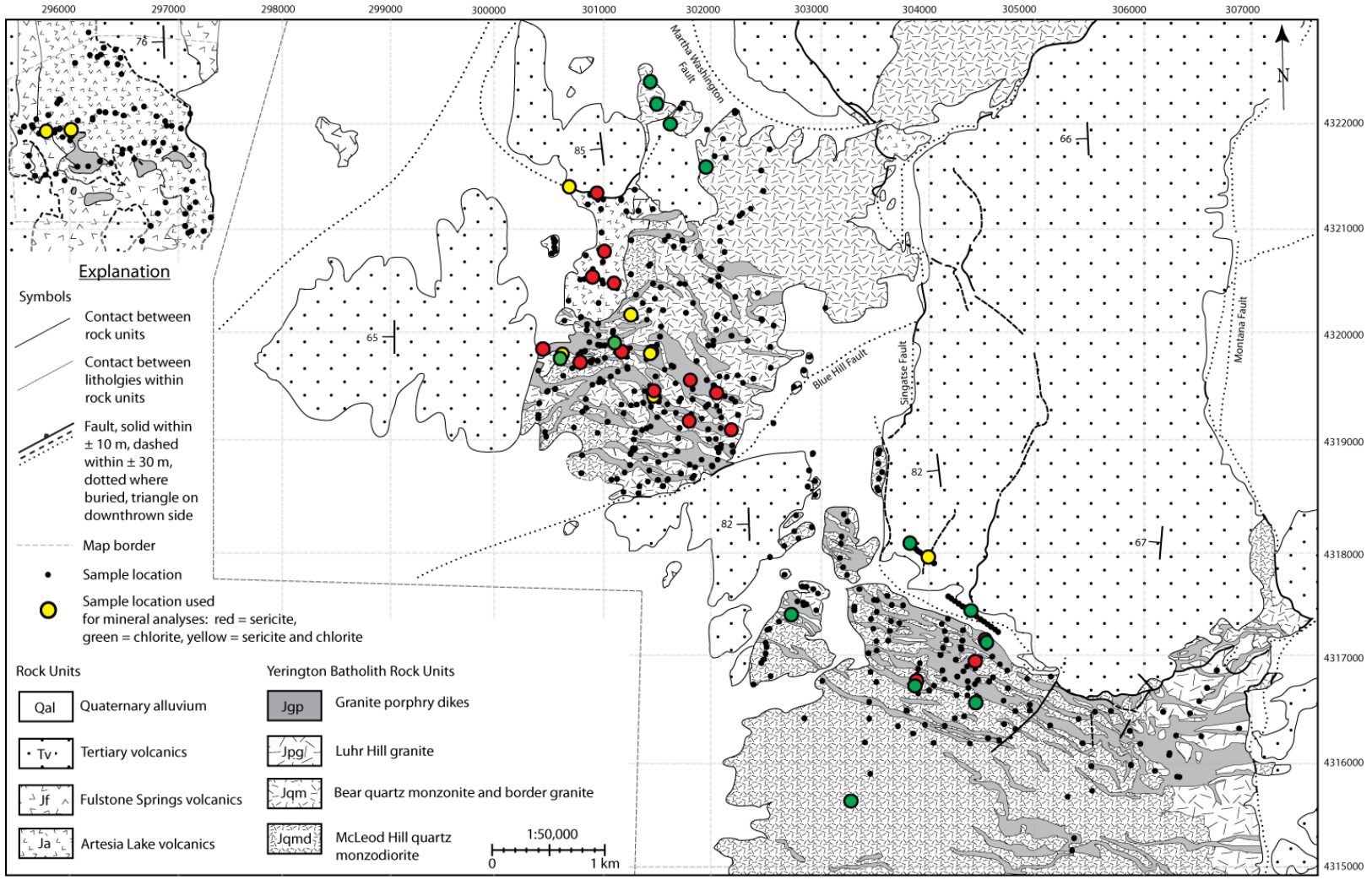

Figure 3.1. Simplified geologic map of the study area modified from Proffett and Dilles (1984) and Lipske (2002). Sample locations are shown as circles, colored circles represent samples used in mineral analyses.

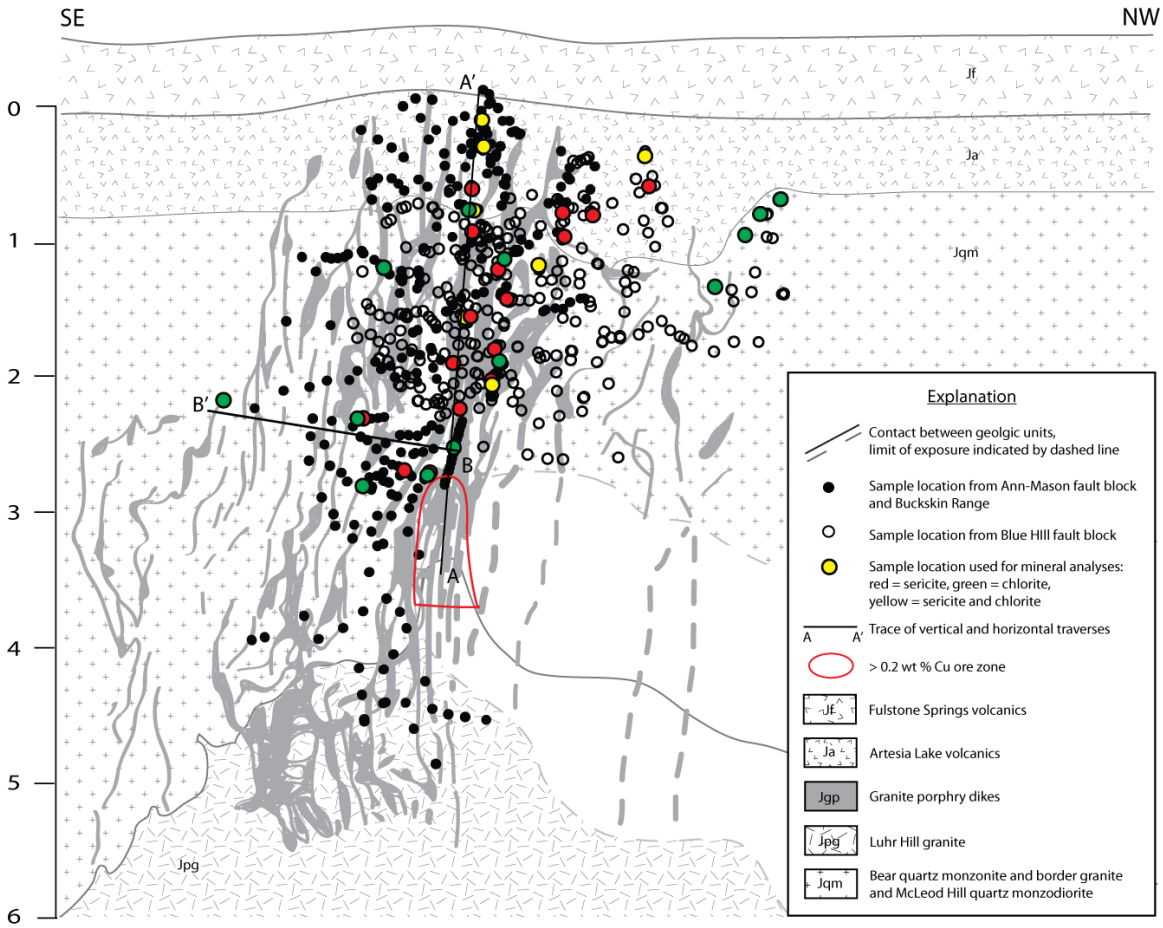

Figure 3.2. Cartoon Jurassic cross-section through Ann-Mason porphyry-Cu deposit modified from Dilles (1987). Sample locations (black and hollow circles) are shifted to approximate position within the paleo cross-section. Colored circles represent samples used in mineral analyses. The red outlined region represents boundary of 0.2 wt % Cu sulfide ore. Lines from A to A' and B to B' show the trace of horizontal and vertical traverses used to describe mineral trace element spatial gradients.

3.3.2 Inductively coupled plasma-mass spectrometry and inductively coupled plasma-atomic emission spectroscopy

Major and trace element concentrations of 48 elements (9 major, 39 trace) for 618 rock samples were determined using inductively coupled plasma-mass spectrometry (ICP-MS) and inductively coupled plasma-atomic emission spectroscopy (ICP-AES) with 4-acid digest (ME-MS61) by ALS Chemex in Reno, Nevada. This method analyzes the

solution produced by 4-acid digest by both methods for major, minor and selected trace elements and ICP-MS for remaining trace elements. This technique was used because it returns data for a wide range of trace elements at low limits of detection including Li (< 0.2 ppm), which was of interest in this study. Zirconium concentrations are low (average 32 ppm) in this data set compared to previously published data from Dilles (1987) using x-ray fluorescence (average 143 ppm) suggesting 4-acid digest is incomplete for zircon and other refractory phases and elements such are hafnium (Hf) are underreported in this data set. Lower and upper limits of detection for ICP-MS/AES can be found in Appendix B.

3.3.3 Laser ablation-inductively coupled plasma-mass spectrometry

Trace element concentrations in minerals were obtained at the W.M. Keck Collaboratory for Plasma Spectrometry at Oregon State University using a NewWave DUV 193 nm ArF Excimer laser on a VG PQ ExCell quadrupole ICP-MS. A summary of the analytical technique is described in Kent et al. (2004). Trace element concentrations of 26 elements were measured for 39 samples. A total of 370 analyses were taken with 10-15 mineral grains analyzed per sample. A 100 μm diameter laser spot size with 40-45 s dwell time was used for analysis. NIST-610, NIST-612 and GSE-1G served as calibration standards and GSD-1G as a secondary standard. Data were processed using in-house LaserTRAM software (Kent et al., 2004). Silica was used as an internal standard in combination with measured SiO_2 wt % from electron microprobe analysis (EMPA). Details on limits of detection can found in Appendix B.

During LA-ICP-MS analysis and data reduction, each LA-ICP-MS spot was assessed for data quality and assigned a value of 0, 1.0, 1.5, 2.0, 2.5 or 3.0, depending on the likelihood of contamination by inclusions and the overall data quality as determined by the number of elements with low variance (<5%) according to the LaserTRAM software. Only analyses with a data quality value ≥ 2.0 are presented in this study. A total of 181 LA-ICP-MS analyses with data quality ≥ 2.0 were obtained for white mica/illite. A total of 186 LA-ICP-MS analyses with data quality ≥ 2.0 were obtained for chlorite. All data can be found in Appendix F. For data presentation and interpretation,

one isotope was selected as representative for elements where more than one isotope was measured (Cu^{63}, Zn^{66}, Ba^{138}, Se^{77}).

3.3.4 Contribution of inclusions to LA-ICP-MS data

To achieve low limits of detection, a 100 μm beam diameter was used in LA-ICP-MS analysis, which is often larger than the grain size of hydrothermal white mica and chlorite (~10-100 μm) in the sample. In addition, the conversion of biotite to muscovite or chlorite results in the formation of rutile, which often occurs as inclusions with, or interstitial between, fine-grained sheet silicate sheaves. Other fine-grained accessory minerals such as apatite, zircon, tourmaline, hematite, goethite or jarosite also occur as inclusions within hydrothermal phyllosilicates. Elements common in inclusions are Ti (rutile), P (apatite), Cu (chalcopyrite or glassy limonite), other chalcophile elements such as Mo, As, Se, Bi and Pb that are commonly present in sulfides and would likely be present in Fe oxide or hydroxide weathering products. Time-resolved counts per second data were screened for spikes in these elements to identify analytical spots that may contain more than one mineral. Those data were given a low data quality value (<2.0) and discarded. Titanium, P and B were plotted against other trace elements to identify correlations with inclusion phases such as rutile, apatite and tourmaline that could confuse data interpretation. No correlations were found.

In order to account for the effect of inclusions and heterogeneities in the remaining data, high and low outliers were determined by Turkey or box and whisker plots and excluded from the results. Turkey outliers are determined by calculating the median and dividing data into quartiles. High and low outliers are identified as analyses that are greater than one and a half times the limit of the upper or lower quartile range. For Ti and Mn, which were analyzed by both EMPA and LA-ICP-MS and present in micas in concentrations greater than the limit of detection in EMPA (~100 ppm), data collected by each method were plotted against each other to evaluate the effects of inclusions on the data (Figure 3.3). For Mn, the EMPA and LA-ICP-MS give similar concentrations and most points lie near a 1:1 line despite the difference in spatial resolution. For Ti, ~30% of analyses from LA-ICP-MS lie off the 1:1 and indicate

contamination by rutile inclusions. Using ioGAS^{TM} software, Ti data were selected that lie near or below the 1:1 line and only these data are included in the results section.

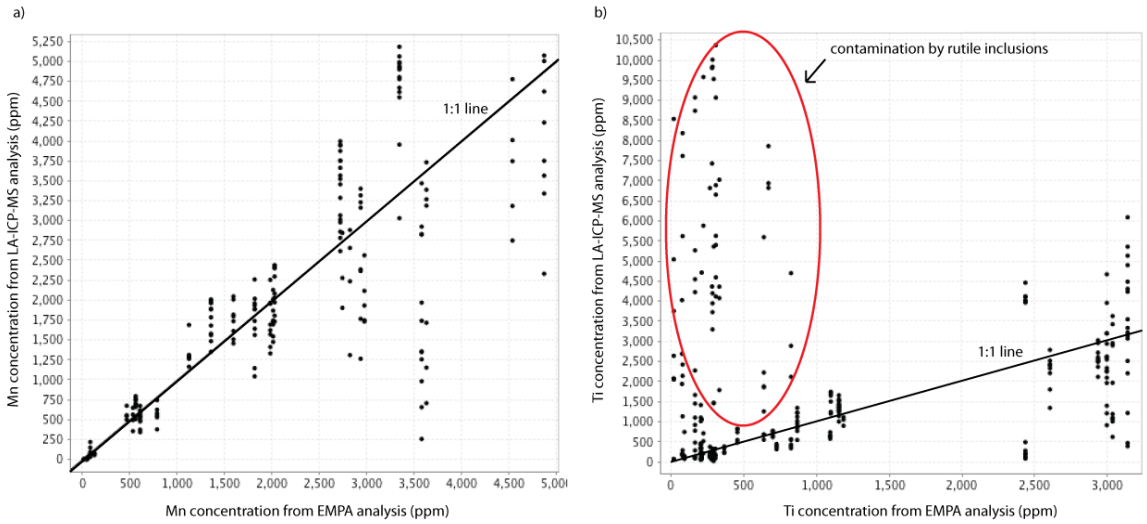

Figure 3.3. Mineral trace element concentrations (ppm) determined by LA-ICP-MS plotted against average concentrations determined by EMPA: a) Mn, b) Ti.

3.3.5 Estimation of alteration types using rock chemistry

In order to determine hydrothermal alteration types for samples used in mineral analyses, mineralogy was determined through detailed petrography of samples in thin section (Chapter 2). This type of detailed analysis was not done for the entire buck rock sample set (618 samples). Instead, using the lithogeochemical data, samples were assigned estimated mineralogy. General proportions of alkali and alkali-earth silicate and aluminous minerals within each sample (feldspars, sheet silicates) were estimated by comparing the molar proportions of alkali, alkaline earth elements and aluminum (Figure 3.4b) to molar ratios (K/Al, Na/Al, Ca/Al) of ideal mineral compositions (Figure 3.4a) (Appendix G). The estimated mineralogy of each sample was plotted spatially and crosschecked against published hydrothermal alteration maps of the region (Dilles and Einaudi, 1992). The estimated mineralogy of a sample corresponds to a predicted hydrothermal alteration type from Chapter 2 or other published literature (Dilles and Einaudi, 1992; Lipske, 2002) and, henceforth, in this study, is referred to by alteration type. Figure 3.5 is an illustration of the positions of alteration types relative to the ore body in cartoon cross-section at the Ann-Mason deposit.

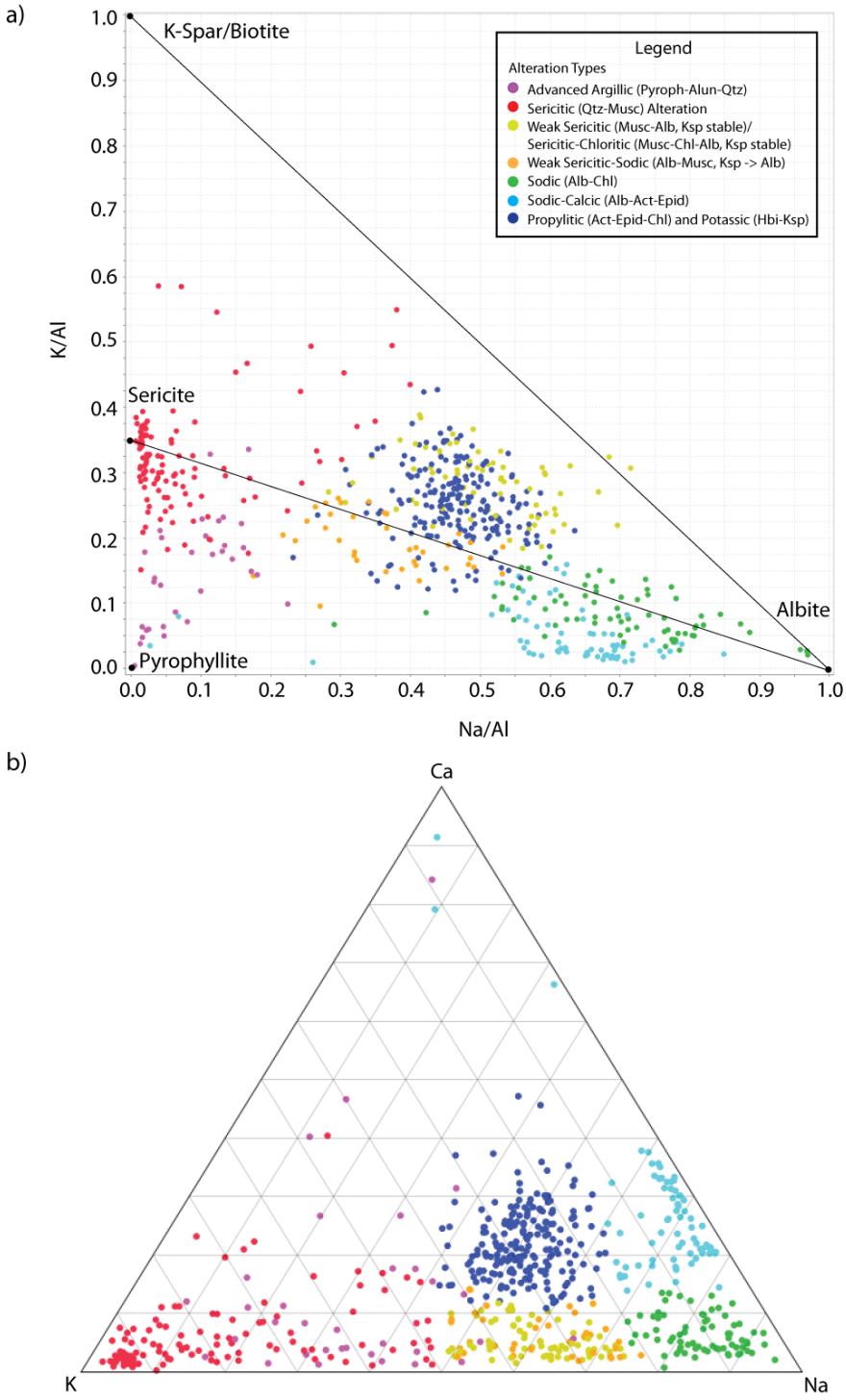

Figure 3.4. Plots of molar proportions from lithogeochemical data used to designate alteration types. a) K/Al versus Na/Al, b) Ca-Na-K ternary diagram. Color code used in legend correlates with alteration types from Chapter 2 or Dilles and Einaudi (1992).

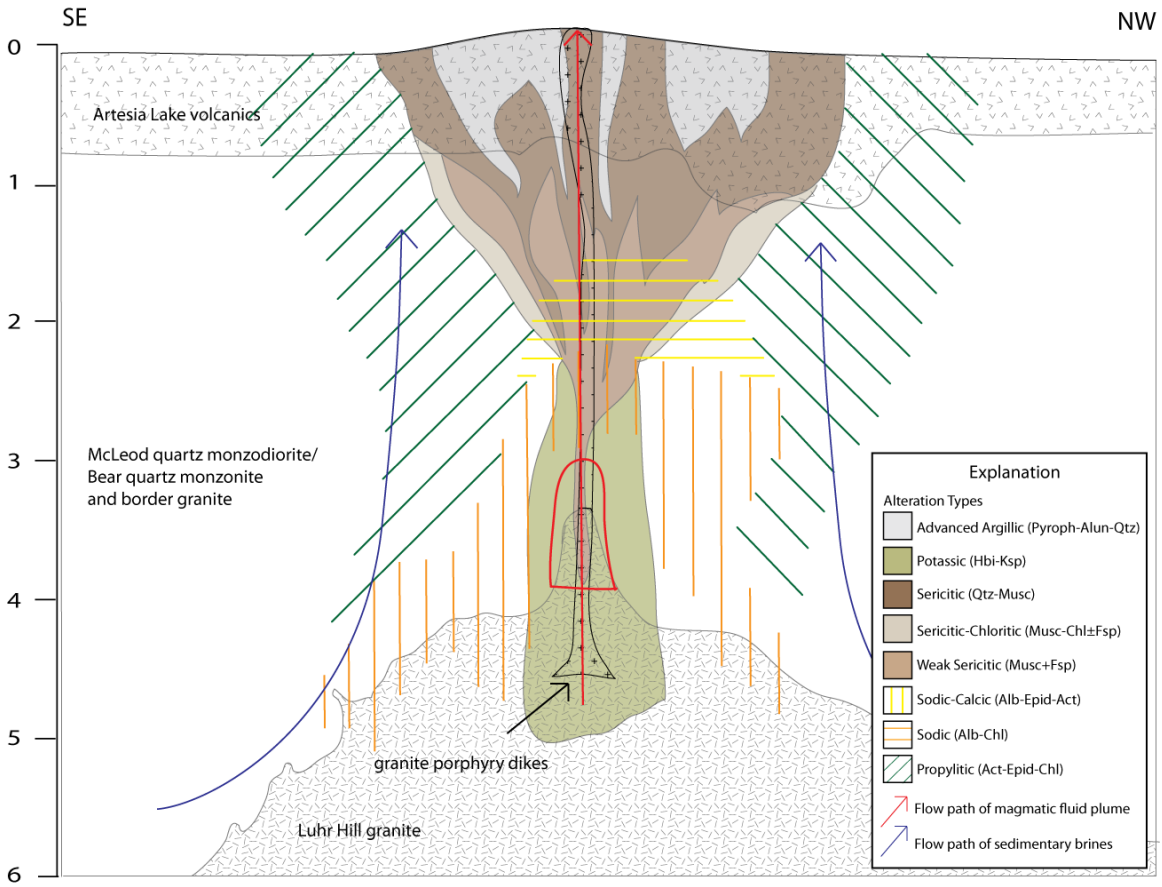

Figure 3.5. Illustration of zoned alteration types and their position relative to the ore body in a cartoon cross-section of the Ann-Mason deposit, Nevada (modified from Dilles et al., 2000). Colors and patterns indicate alteration types and arrow show general flow path of magmatic and non-magmatic fluids. The ore zone is outlined in red.

3.4 Results

3.4.1 Rock composition

A summary of data from ICP-MS/AES analyses organized by alteration type is presented in Table 3.1. Rock compositions of different alteration types are compared using probability plots. To create a probability plot, the assay value of an element (X) is plotted against the N score for each sample. The N score is defined as:

$$N = (concentration\text{-}mean)/standard\ deviation$$

Samples of each alteration type are plotted as a colored symbol on the probability plot, which allows the viewer to see, at a glance, in which alteration type each trace element is most abundant (Figure 3.6).

In the following discussion, elements are considered "anomalous" if their concentration in the top 10% of values (90-100%) and is more than 500% greater than unaltered rocks. Elements are termed "enriched" if values are 200-500% greater (Table 3.2). To compare altered to fresh rock, average unaltered rock values from units of the Yerington batholith were compiled from previously published data (Dilles, 1987; Dilles and Proffett, 1995).

Trace elements are divided into three groups: (1) chalcophile elements (Cu, Mo, As, Sb, Se, Te, Bi), (2) lithophile elements (Li, Rb, Sr, Cs, Ba, Sn, W, Tl) and (3) transition metals (Cr, Mn, Co, Zn, Sc, V, Ti). These are modified groupings based on general geochemical behavior of elements within this system as determined by rock and mineral analyses and combine the affinities defined by Goldschmidt (1937) and groupings of elements within the periodic table. For example, Zn and Cu are both transition metals and chalcophile. During the crystallization of the Yerington batholith, however, Zn behaves compatibly and is incorporated into amphibole and biotite. Copper behaves incompatibly and is enriched in the melt, incorporated in the magmatic volatile phase and, eventually, deposited by the ore fluid in sulfide minerals (bornite and chalcopyrite) (Dilles and Proffett, 1995). It is the chalcophile behavior that defines the distribution of Cu and, since Zn behaves as a lithophile, its distribution is better described by its position in the periodic table as a transition metal. These modified groupings may not apply to all porphyry-Cu environments since the geochemical affinity of an element varies depending on a number of variables including the initial melt composition, depth of magma emplacement, volatile content of the magma and the composition of the magmatic volatile phase including fluid salinity and composition, redox conditions and pH.

Table 3.1. Summary of rock trace element concentration by ICP-MS/AES organized by alteration type.

	Advanced Argillic (Pyroph-Qtz-Alun) (n=33)			Sericitic (Qtz-Musc) (n=111)			Weak Sericitic (Musc-Ab-Ksp) (n=70)			Sodic Alteration (Ab-Chl) (n=71)			Sodic-Calcic (Act-Epid-Ab) (n=71)			Propylitic (Act-Epid-Chl) (n=104)		
Element (ppm)	Median	Mean	σ[1]	Median	Mean	σ	Median	Mean	σ	Median	Mean	σ	Median	Mean	σ	Median	Mean	σ
As	6.4	11	13	6.20	11	16	6	9	10	4.5	6.3	7.9	1.7	3.7	8.3	3.0	3.3	2.4
Ba	260	434	437	930	1155	998	1760	1788	632	320	460	359	240	350	357	1310	1401	442
Bi	0.49	0.85	1.0	0.53	0.99	1.4	0.38	0.51	0.78	0.24	0.35	0.34	0.11	0.31	0.77	0.12	0.18	0.17
Co	0.50	2.0	5.5	0.90	2.5	4.9	1.3	2.8	3.9	1.3	3.8	4.8	2.2	4.0	3.7	6.0	7.9	5.7
Cr	22	27	18	10	18	17	9.0	11	10	10	12	9.6	12	13	4.6	12	14	11
Cs	0.16	0.28	0.33	1.4	1.6	1.1	1.0	1.2	0.59	0.68	0.77	0.58	0.52	0.63	0.44	0.90	1.13	0.77
Cu	16	21	17	36	202	787	59	319	1036	85	596	1241	81	1968	11291	75	162	258
Li	1.0	6.9	16	5.4	7.1	7.8	3.6	4.7	3.6	4.7	5.6	3.8	3.3	4.0	2.6	4.3	4.5	2.3
Mn	22	50	95	51	96	120	60	97	97	53	92	111	113	181	250	233	327	220
Mo	2.3	4.3	5.5	2.4	4.7	6.7	2.2	6.4	20	1.7	4.3	11	0.97	4.6	14	1.2	1.4	0.8
Na	0.44	0.46	0.36	0.23	0.46	0.56	3.0	3.1	0.52	4.15	4.12	0.70	3.9	3.7	0.86	3.0	3.0	0.3
Ni	1.7	3.4	5.5	2.4	5.8	10	2.8	4.9	4.86	5.8	8.1	11	8.4	9.2	6.5	11	12	9.4
P	1280	1492	1174	550	679	503	455	578	442	570	640	334	830	992	783	905	1040	390
Pb	26	38	34	5.4	12	30	5.4	5.9	3.4	3.2	4.8	7.4	4.1	4.5	2.6	6.2	7.1	3.8
Rb	7.6	19	22	111	111	42	86	86	21	30	32	14	9.3	17	16	69	72	25
Sb	2.7	3.90	3.2	1.9	3.3	3.4	0.80	1.3	2.1	0.60	1.1	2.0	0.57	1.1	1.9	0.93	1.3	1.1
Sc	4.4	5.09	3.8	6.8	7.1	4.0	4.8	5.4	2.2	5.0	5.6	2.8	6.0	7.6	7.3	6.6	7.8	3.1
Se	3.0	3.36	2.1	2.0	3.4	3.1	2.0	2.6	1.8	2.0	2.6	2.8	2.0	2.8	8.3	1.0	1.4	0.7
Sn	1.0	1.08	0.53	1.1	1.5	1.4	0.70	0.96	0.65	0.90	1.0	0.69	1.0	1.2	0.64	1.0	1.0	0.4
Sr	1050	1199	914	128	307	469	477	501	208	398	466	240	1030	1033	253	939	932	188
Te	0.41	0.53	0.45	0.31	0.75	1.10	0.20	0.47	1.1	0.19	0.29	0.41	0.06	0.14	0.31	0.05	0.06	0.14
Th	5.8	6.9	5.0	7.4	8.6	5.9	7.8	9.6	6.7	7.2	8.2	4.1	8.4	10	7.9	7.8	9.3	4.2
Ti	0.27	0.30	0.14	0.23	0.24	0.10	0.22	0.23	0.08	0.20	0.21	0.09	0.26	0.27	0.10	0.29	0.32	0.09
Tl	0.29	0.55	0.81	0.74	1.1	1.3	0.46	0.48	0.19	0.13	0.17	0.17	0.07	0.09	0.07	0.28	0.30	0.11
U	1.9	2.2	2.0	2.8	3.2	1.9	3.7	4.1	2.2	2.9	3.3	1.8	2.9	4.6	12	3.2	3.5	1.2
V	116	119	62	89	92	50	50	60	32	53	61	34	56	69	44	67	84	37
W	1.1	1.5	1.5	1.8	2.5	2.4	1.60	2.21	1.86	2.0	2.9	2.4	0.80	2.5	5.7	0.95	1.3	2.1
Zn	1.0	11	49	6.0	13	20	7.00	11.4	12.0	5.0	13	24	10	14	12	18	28	24

[1] σ refers to one standard deviation.

Table 3.2**.** Summary of rock trace element concentrations from ICP-MS/AES divided into lower 50%, 50-75%, 75-90%, 90-95% and 95-100% of values and compared to unaltered rocks from the Yerington batholith and average crustal abundance.

Element (ppm)	Percentage of values					Range of average content in Yerington batholith rocks **	Average crustal abundance ***
	<50%	50 – 75%	75 – 90%	90 – 95%	95 – 100%		
Cu	<100	100-200	200-1000	**1000-5000**	5000-15000	5-80	55
Mo	<2	2-3	3-7	**7-20**	20-900	<0.2-1.1	1.5
As	<4	4-7	7-14	**14-20**	20-150	0.3-0.9	1.8
Ba	<1000	1000-1500	1500-2000	2000-2400	2400-6000	1300-1750	425
Bi	<0.2	0.2-0.5	0.5-1.0	**1.0-1.8**	1.8-10	0.02-0.1	0.17
Co	<2	2-6	6-12	12-15	15-50	7-55	25
Cs	<1	1.0-1.5	1.5-2.0	2.0-2.8	2.8-6.6	1.5-4.2	3
Li*	<5	5-7	7-10	10-15	15-80	3.2-5.7	20
Mn	<100	100-200	200-400	400-500	500-1500	230-650	1000
Pb	<5	5-8	8-15	**15-30**	30-900	1.5-7	12.5
Rb	<70	70-95	95-120	120-140	140-230	80-150	90
Sb	<1	1-2	2-4	**4-6**	6-18	0.1-0.4	0.2
Sc	<6	6-9	9-12	12-13	13-65	5-9	22
Se	<1	1-2	2-4	**4-6**	6-70	<0.05-3.0	0.05
Sn*	<0.9	0.9-1.3	1.3-1.8	1.8-2.5	2.5-10	0.6-1.2	2
Sr	<725	725-1000	1000-1150	1150-1300	1300-4500	700-1200	375
Te*	<0.1	0.1-0.4	0.4-0.8	**0.8-1.3**	1.3-8.8	<0.05	0.002
Ti	<2500	2500-3200	3200-4300	4300-4650	4650-6600	3300-5150	4400
Tl*	<0.3	0.3-0.5	0.5-0.9	**0.9-1.5**	1.5-12	0.2-0.3	0.45
V	<60	60-110	110-135	135-160	160-450	50-140	135
W*	<1	1-2	2-5	**5-7**	7-200	0.2-1.2	1.5
Zn	<10	10-20	20-40	40-65	65-280	18-40	70

*Previously published data were unavailable for these elements and concentrations from the least-altered rocks in current data set were used.
**Compositions from unaltered rocks of the Yerington batholith compiled from Dilles (1987) and Dilles and Proffett (1995).
***Average crustal abundances (1:1 basalt to rhyolite) from Taylor (1964).

3.4.1.1 Trace elements gradients in altered rocks

3.4.1.1.1 Chalcophile elements

Copper is anomalous in altered rock relative to fresh rock in drill holes that sample the > 0.2 wt % Cu sulfide ore zone and enriched in potassic alteration above the ore zone from 2.5 – 2.0 km paleodepth (Figure 3.6a/3.7a). Above ~ 2.0 km, Cu is not enriched in altered rocks with the exception sporadic anomalous Cu values. Anomalous Mo values (> 2 ppm) form a broad halo with significant enrichment in rocks from drill core that samples the ore zone and from nearby exposures (~2.3 to 2.5 km). Erratic anomalous values of Mo extend vertically from for 1 to 2.5 km paleodepth and laterally ~

1 km (Figure 3.6b/3.7b). Tellurium, Se, Bi, Sb, and As are anomalous or enriched in rocks from sericitic and advanced argillic alteration. Selenium forms a long narrow anomaly (>4 ppm) from just below the paleosurface (~0.3 km) to 2.5 km depth that runs along the axis of magmatic hydrothermal fluid flow and is enriched in drill core that samples the ore zone. Tellurium has a slightly broader enrichment pattern (> 0.8 ppm) than Se that begins above the ore zone at ~2.5 km and extends to just below the paleosurface (~0.3 km). Tellurium is barely anomalous in drill core (>0.1 ppm). Anomalous Bi values (> 1 ppm) are concentrated from ~ 2 km paleodepth, above the zone of potassic alteration, to the paleosurface. The Sb anomaly (>4 ppm) forms a broad lateral halo at shallow depths from ~ 1km to the paleosurface. Arsenic enrichment forms a funnel-shaped anomaly (>14 ppm) that extends from the ore zone at ~ 3.5 km depth to 0.5 km from the paleosurface. Arsenic is not enriched in samples from drill core. Lead is enriched in advanced argillic alteration only and forms a weak anomaly (>28 ppm) near the paleosurface above ~ 1km.

3.4.1.1.2 Lithophile elements

Neither Cs nor Rb is enriched in altered rocks compared to fresh rock values and Rb is depleted in rocks affected by sodic or sodic-calcic alteration. Barium forms a broad, weak enrichment (>2400 ppm) from ~ 1 – 2 km paleodepth (Figure 3.6c) in sericitic alteration and weak sericitic alteration where K-feldspar is preserved. Lithium is relatively evenly distributed throughout alteration types but slightly higher in sericitic alteration. Anomalous Li values (>15 ppm) are concentrated in the upper ~ 1 km and form a broad halo at shallow depths (Figure 3.6d/3.7c). Thalium and tin are enriched in samples from sericitic alteration relative to fresh rock values. Thalium enrichment (>1.5 ppm) is virtually restricted to rocks from the Artesia Lake volcanic unit and is focused in laterally broad but vertically narrow zone from ~ 0.8 km to the paleosurface (Figure 3.6e/3.7d). Tin enrichment (>2.5 ppm) is relatively weak (2x average fresh rock) and forms a cross-shaped anomaly centered on the porphyry dike swarm and narrow (<0.5 km) from the ore zone to the paleosurface and with a broader zone (~ 1 km wide) from ~1.5 to 2.0 km depth. Anomalous W values (> 5 ppm) occur in rocks affected by sericitic and sodic alteration and form a wedge-shaped anomaly above the ore body from ~2 – 2.5

km with sporadic anomalous values at ~ 1km paleodepth (Figure 3.6f/3.7e). Stronium is depleted in rocks from sericitic and advanced argillic alteration and weakly enriched (>1500 ppm) in zones of sodic-calcic alteration from ~ 2.5 – 4 km paleodepth compared to fresh rock values (~ 1000 ppm).

3.4.1.1.3 Transition metals

Zinc, Mn, Ni and Co are depleted from the ore zone and the surrounding region of hydrothermal alteration and are most abundant in the least altered rocks (Figure 3.6g/3.7f). Vanadium and scandium concentrations are highly dependent on the silica content of the unaltered lithologies and appear to be relatively immobile during alteration. Titanium is also immobile with highest concentrations of Ti in the least-altered rocks.

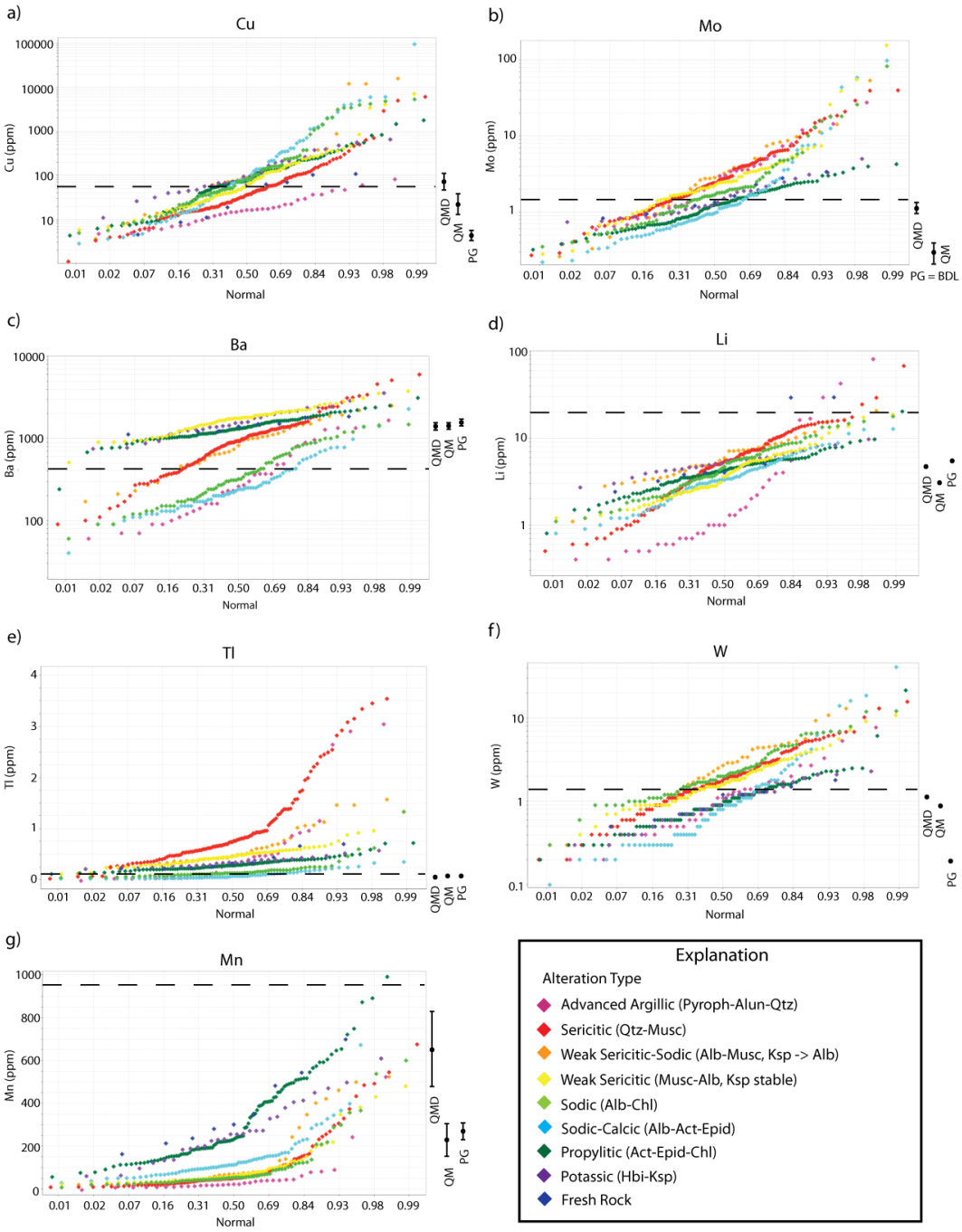

Figure 3.6. Probability plots of trace element concentrations (ppm) from lithogeochemistry for selected elements: a) Cu, b) Mo, c) Mn, d) Tl, e) W, f) Li and g) Ba. Colors represent alteration types. Dashed line is the average crystal abundance (Taylor, 1964). On the right side of each plot, mean (dot) and standard deviation (error bars) from unaltered McLeod quartz monzodiorite (QMD), Bear quartz monzonite (QM) and Luhr Hill granite (GP) samples are shown for reference.

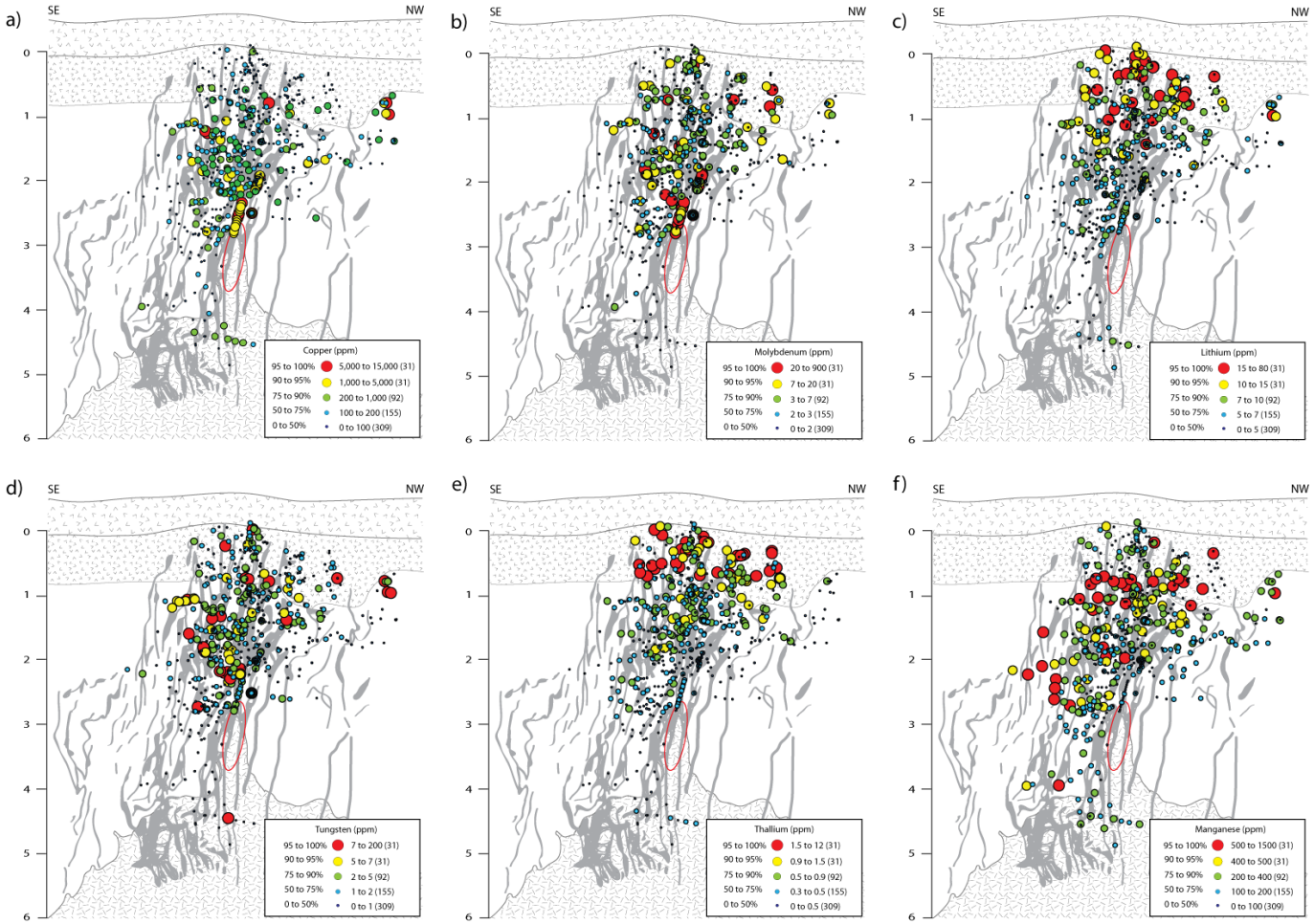

Figure 3.7. Trace element gradients in rock chemistry presented on cartoon Jurassic paleo-cross section (Figure 3.2) where each circle represents a sample and the size and color represents the relative concentration of the specified element (ppm) as shown by the scale on the right: a) Cu, b) Mo, c) Li, d) W, e) Tl, f) Mn.

Table 3.3. Summary of trace element concentrations in analyzed minerals by LA-ICP-MS.

	Chlorite (n=168)			Muscovite and Illite (n=149)			Muscovite-Paragonite (n=20)			Pyrophyllite (n=11)		
Element (ppm)	Median	Mean	σ	Median	Mean	σ	Median	Mean	σ	Median	Mean	σ
Li	48	47	13	7.4	7.9	3.5	15	15	10	1.4	1.9	1.6
B	2.0	2.5	1.5	47	52	33	27	27	4.4	8.7	7.3	3.2
P*	44	65	51	105	151	121	81	81	25	797	784	350
Sc	3.4	5.0	3.9	10	13	8.9	2.6	2.6	0.93	5.3	4.9	1.4
Ti	144	284	611	1268	1616	1200	46	143	139	18	52	65
V	154	208	134	197	220	149	81	94	32	117	111	14
Cr	32	43	37	16	29	29	32	32	20	7.3	7.5	1.2
Mn	1932	2175	1313	38	51	43	0.92	2.0	1.9	6.1	6.3	3.4
Co	21	31	27	0.47	0.58	0.41	0.14	0.14	0.08	0.21	0.26	0.16
Cu	235	276	251	4.5	10.0	11	2.4	2.3	1.0	6.1	8.2	6.3
Zn	218	215	93	7.8	8.7	5.2	1.7	1.9	0.95	3.2	4.2	2.8
As**	0.55	0.71	0.49	0.52	0.57	0.37	1.5	1.5	0.82	4.6	4.6	2.7
Se***	0.73	0.85	0.48	1.4	1.53	0.81	1.1	1.1	0.34	1.9	2.3	0.95
Rb	3.0	8.2	11	287	286	107	41.23	86	71	0.97	0.88	0.37
Sr	4.9	11	14	28	35	23	1.2	2.6	3.9	85	78	75
Mo**	0.17	0.21	0.16	0.30	0.66	0.76	0.95	4.1	7.1	14	16	15
Sn*	0.27	0.33	0.21	3.2	4.7	4.2	0.81	0.87	0.39	0.25	0.26	0.12
Te***	0.10	0.16	0.17	0.23	0.31	0.25	0.32	0.51	0.52	0.30	0.47	0.43
Cs	0.56	0.81	0.81	2.4	2.4	1.1	0.68	0.97	0.72	0.15	0.18	0.06
Ba	7.0	20	29	1257	1452	1014	3.7	16	18	17	20	17
W*	0.26	0.72	1.0	1.8	2.9	2.7	0.03	0.05	0.04	0.20	0.23	0.17
Pb*	1.0	1.8	1.9	0.44	0.65	0.52	1.2	6.9	10	1.5	2.4	2.3
Bi**	0.03	0.06	0.07	0.05	0.09	0.09	0.05	0.08	0.09	0.06	0.06	0.05
Th**	0.15	0.32	0.38	0.12	0.41	0.57	BDL	BDL	BDL	3.2	4.6	4.6
U**	0.14	0.47	0.63	0.15	0.26	0.29	0.01	0.02	0.02	0.17	0.17	0.09
Tl	0.03	0.13	0.17	1.51	1.6	0.80	1.6	2.0	1.1	BDL	BDL	BDL

* 5 – 20% of analyses are below the limit of detection

** 20 – 50% of analyses are below the limit of detection

*** 50 - 90% of analyses are below the limit of detection

Table 3.4. Summary of trace element concentrations in muscovite and illite by LA-ICP-MS grouped by alteration type.

	Muscovite from sericitic alteration (n=87)			Muscovite from sericitic-chloritic alteration (n=14)			Illite from illitic alteration (n=44)			Illite from illitic-chloritic alteration (n=5)		
Element (ppm)	Median	Mean	σ	Median	Mean	σ	Median	Mean	σ	Median	Mean	σ
Li	7.3	7.5	2.5	6.8	7.0	4.5	7.4	8.0	3.9	16.0	17.1	2.9
B	45	53	30	44	61	48	34	47	33	67	65	3.2
P	89	128	102	37	38	6.4	201	214	118	36	38	4.9
Sc	9.0	11.1	7.2	9.0	15	12	17	18	11	11	11	0.8
Ti	2161	2105	1212	352	453	325	1073	913	522	739	682	159
V	154	182	114	238	303	263	328	279	197	278	283	31
Cr	13	20	18	6.9	14	19	43	46	33	7.5	8.5	1.5
Mn	28	28	18	82	108	54	57	52	28	160	165	25
Co**	0.5	0.49	0.30	3.2	2.2	1.5	0.36	0.50	0.31	1.2	1.3	0.3
Cu	4.3	9.1	9.3	1.7	1.6	0.77	5.1	12	12	17	43	52
Zn	7.1	7.0	4.3	15	21	13	8.9	9.3	4.5	24	29	12
As***	0.6	1.0	1.6	0.30	4.2	9.1	0.63	2.3	4.5	0.40	0.36	0.18
Se***	1.5	1.4	0.70	4.0	18	33	1.3	1.6	0.83	1.2	1.2	0.0
Rb	283	271	64	266	221	93	242	254	139	539	550	35
Sr	29	29	12	28	127	165	27	50	48	51	49	22
Mo***	0.24	0.66	0.80	0.14	0.14	0.001	0.35	0.71	0.74	0.35	0.35	0.20
Sn	4.1	6.3	5.1	1.1	1.7	1.3	2.8	3.5	2.6	1.1	1.1	0.1
Te***	0.27	0.32	0.22	NaN	NaN	NaN	0.21	0.31	0.33	0.10	0.10	0.0
Cs	2.3	2.2	1.0	3.2	3.6	1.8	2.3	2.1	0.91	5.0	4.9	0.5
Ba	1301	1533	1150	1543	1634	1196	1302	1360	765	649	645	19
W	2.3	3.9	3.3	0.81	1.1	1.2	1.5	1.7	1.2	3.1	3.1	0.33
Pb**	0.39	0.46	0.28	1.2	1.2	0.51	0.41	0.64	0.55	0.43	0.52	0.32
Bi***	0.05	0.08	0.07	0.08	0.08	0.05	0.06	0.12	0.16	0.02	0.02	0.01
Th***	0.15	0.38	0.47	0.08	0.36	0.59	0.11	0.82	1.3	BDL	BDL	BDL
U**	0.16	0.29	0.29	0.05	0.07	0.04	0.18	0.56	0.73	0.11	0.20	0.18
Tl	1.5	1.6	0.5	1.2	1.8	1.3	1.2	1.5	1.1	2.9	3.0	0.16

* 5 – 20% of analyses are below the limit of detection

** 20 – 50% of analyses are below the limit of detection

*** 50 - 90% of analyses are below the limit of detection

Table 3.5. Summary of trace element concentrations in chlorite grouped by alteration type.

	Chlorite from propylitic alteration (n=109)			Chlorite from illitic-chloritic alteration (n=16)			Chlorite from sericitic-chloritic alteration (n=44)		
Element (ppm)	Median	Mean	σ	Median	Mean	σ	Median	Mean	σ
Li	45	45	12	53	53	11	56	68	30
B	1.8	1.9	0.90	2.7	4.6	3.6	3.9	4.1	2.5
P*	37	54	40	96	292	383	62	89	75
Sc*	2.6	3.5	2.1	2.2	2.4	0.78	7.0	14	15
Ti**	113	180	242	170	202	141	159	425	1018
V	217	225	127	91	97	22	142	256	232
Cr	31	37	27	54	250	373	66	65	45
Mn	2030	2443	1325	1960	2168	743	1274	1401	887
Co	20	25	20	15	12	8.2	23	33	29
Cu	222	234	186	461	439	106	37	331	549
Zn	207	208	83	251	260	45	245	329	232
As**	0.54	0.80	0.91	1.1	1.6	1.1	1.1	3.3	5.2
Se***	0.71	0.82	0.46	0.79	0.89	0.26	0.71	0.91	0.60
Rb	2.5	7.0	11	20	20	2.4	3.1	11	15
Sr	9.7	23	32	7.0	7.9	4.2	3.4	5.6	5.8
Mo**	0.13	0.14	0.09	0.34	0.45	0.32	0.24	0.32	0.21
Sn**	0.25	0.28	0.14	0.26	0.27	0.14	0.34	0.47	0.44
Te***	0.10	0.10	0.05	2.5	2.8	1.0	0.26	0.37	0.32
Cs	0.41	0.70	0.77	0.86	1.1	0.90	1.1	1.2	0.93
Ba	5.3	29	46	8.5	9.0	5.0	11	24	38
W*	0.25	0.69	0.98	0.22	0.46	0.55	0.29	0.79	1.0
Pb	1.7	2.5	2.3	0.56	0.70	0.56	0.60	0.89	0.93
Bi**	0.03	0.07	0.07	0.02	0.04	0.05	0.03	0.08	0.11
Th**	0.14	0.31	0.37	0.05	0.49	0.88	0.29	0.39	0.35
U**	0.14	0.47	0.62	0.12	0.54	0.75	0.52	1.5	2.0
Tl	0.03	0.15	0.21	0.11	0.11	0.02	0.09	0.15	0.16

* 5 – 20% of analyses are below the limit of detection

** 20 – 50% of analyses are below the limit of detection

*** 50 - 90% of analyses are below the limit of detection

3.4.2 Mineral composition

Generally, muscovite and illite are enriched in lithophile elements whereas chlorites are enriched in transition metals (Figure 3.8). Chalcophile elements are rarely detected in concentrations greater than 1 ppm. Mineral trace element concentrations are presented in Table 3.3-3.5.

3.4.2.1 Muscovite and illite

The most abundant trace elements in muscovite and illite are Ti (average 1600 ppm), Ba (average 1450 ppm), Rb (average 300 ppm) and V (average 200 ppm) and P (average 100 ppm) (Table 3.3). Boron, Mn, Sr and Cr are detected in muscovite and illite at 20-50 ppm, Sc, Cu, Zn and Li at 5 – 20 ppm and Sn, W, Cs, Tl and Se at concentrations between 1 – 5 ppm. Cobalt, As, Mo, Te, Pb, Bi, Th and U are detected at less than 1 ppm levels and are commonly below detection. Compared to chlorite and pyrophyllite, muscovite and illite have higher concentrations of lithophile elements (B, Rb, Ba, Cs, Tl, W, Sn) and the transition metals Sc and Ti (Figure 3.8/3.10).

Muscovite and illite occur in several alteration assemblages and trace element contents vary slightly by alteration type (Table 3.4). Muscovite from sericitic alteration has the highest concentrations of W, Sn and Ti (Figure 3.9a). Muscovite and illite from assemblages with chlorite have higher concentrations of Mn, Zn and V (Figure 3.9a), likely related to their higher Fe+Mg (apfu) contents described in Chapter 2.

3.4.2.2 Intergrowths of muscovite and paragonite

Muscovite is found intergrown with paragonite in one sample from advanced argillic (musc-qtz-alun assemblage) and one from sericitic alteration (qtz-musc assemblage) (see Chap. 2 for more detail). These intergrowths are on the < 5 μm scale and, since the LA-ICP-MS spot size was 100 μm, both minerals were analyzed in each LA-ICP-MS spot. The same set of trace elements are most abundant in the LA-ICP-MS analyses of the muscovite-paragonite mixture as in muscovite and illite (V, P, Ti, Rb) with the exception of Ba (average 16 ppm) and the overall concentrations are ~50 – 90% lower (Table 3.3). Lead (average 1.2 ppm) and Li (average 15 ppm) concentrations are higher in mixtures of muscovite-paragonite than in other white micas (Figure 3.8).

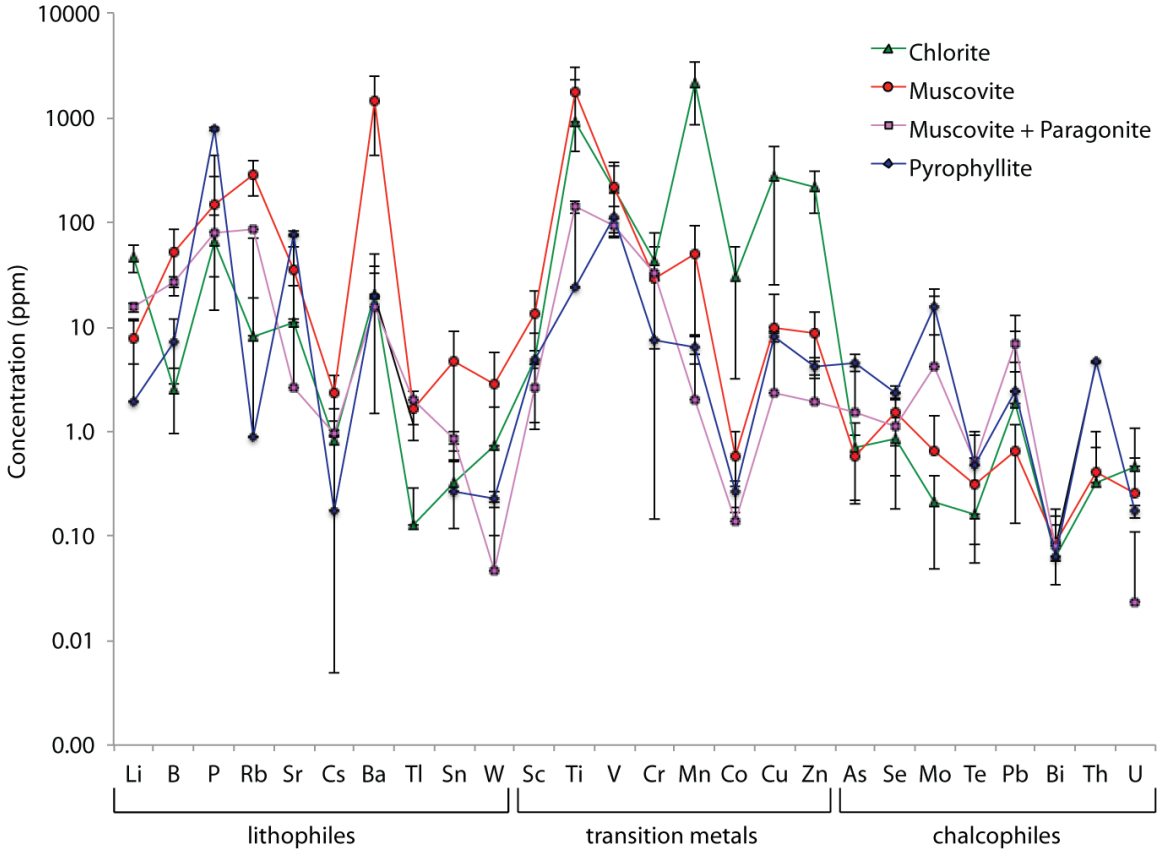

Figure 3.8. Comparison of chlorite, muscovite and illite, mixed muscovite-paragonite, pyrophyllite trace element compositions (ppm) from LA-ICP-MS analyses. Data also presented in Table 3.3. Colored symbols represent mean value and bars represent one standard deviation.

3.4.2.3 Pyrophyllite

Pyrophyllite from one sample of advanced argillic (pyroph-qtz assemblage) alteration was analyzed. Trace element concentrations are generally lower in pyrophyllite compared to muscovite except for P (average 780 ppm), Sr (average 78 ppm), Mo (average 16 ppm), As (average 5 ppm), Th (average 5 ppm) and Se (average 2 ppm), which are most abundant in pyrophyllite (Figure 3.8/3.10, Table 3.3).

3.4.2.4 Chlorite

The most abundant trace elements in chlorite are Mn (average 2200 ppm), Cu (average 280 ppm), Zn (average 220 ppm), V (average 210 ppm) and Ti (average 280 ppm). Trace elements in concentrations from 20-50 ppm include P, Li, Cr and Co. Overall, chlorites have the highest concentrations of Li and transition metals (Mn, Cu, Zn, Co, Cr) (Figure 3.8/3.10, Table 3.3). A comparison of chlorite from different alteration types (Figure 3.9b and Table 3.5) shows chlorite from propylitic alteration has the highest concentrations of Sr and Pb while chlorite from sericitic-chloritic alteration, has the highest Li, Co, Sc and Zn contents. Chlorite from illitic-chloritic alteration has higher P, Rb, Cr and Cu.

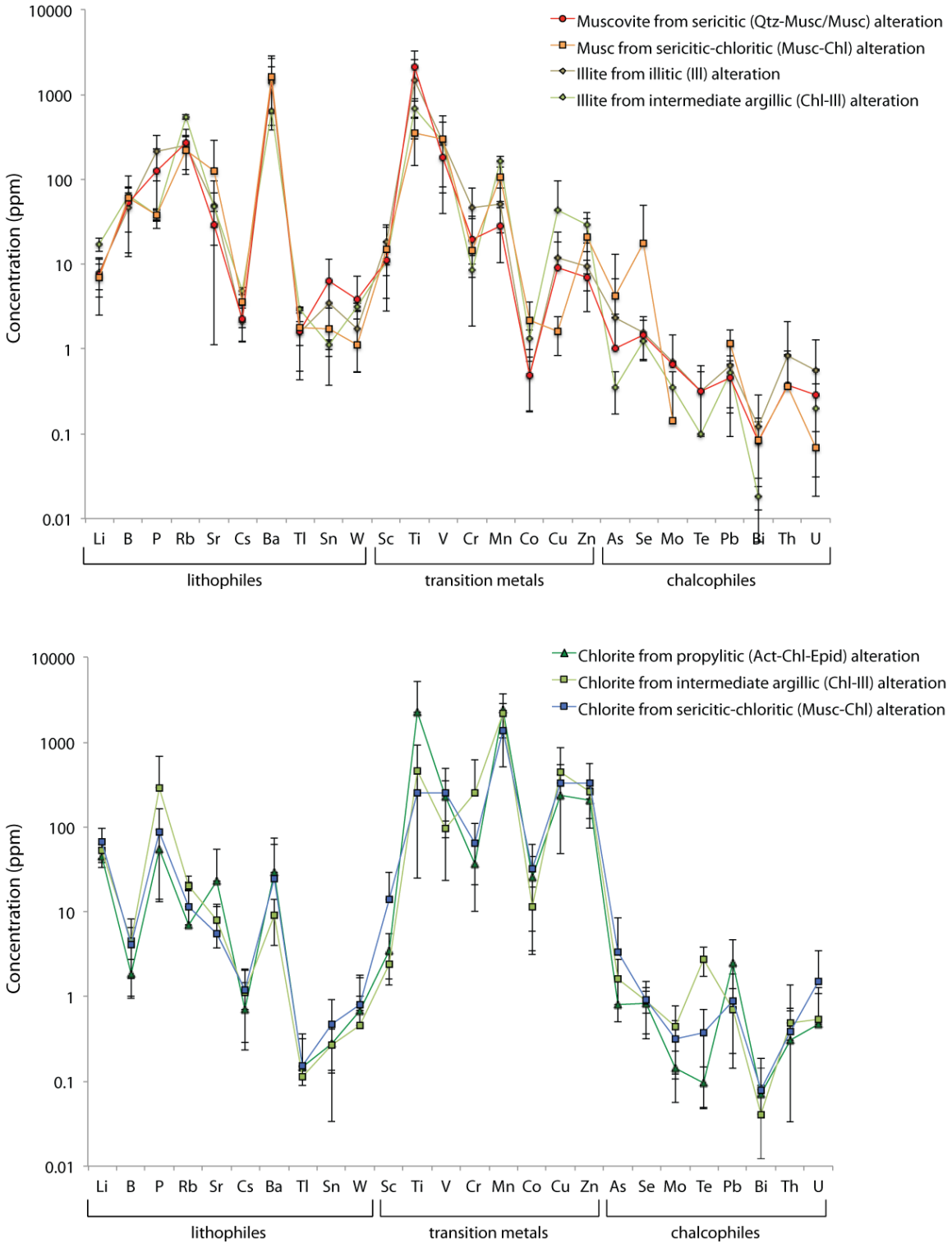

Figure 3.9. Comparison of mineral trace element compositions from different alteration assemblages: a) muscovite and illite alteration types, b) chlorite alteration types. Colored symbols represent mean value and bars represent one standard deviation.

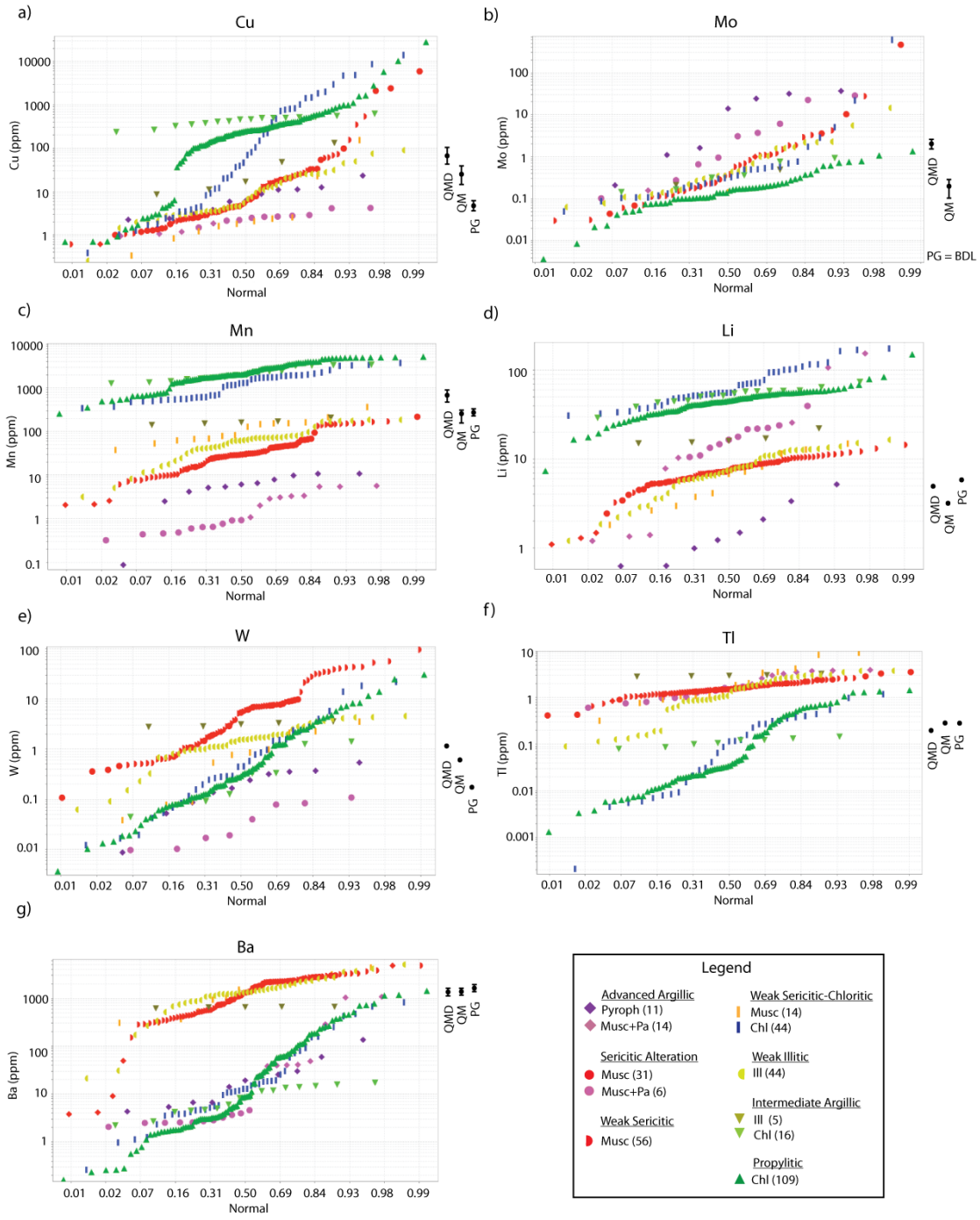

Figure 3.10. Probability plots of trace element concentrations (ppm) in micas and chlorite for selected elements: a) Cu, b) Mo, c) Mn, d) Li, e) W, f) Tl and g) Ba. Colors represent mineral type and shapes represent mineral assemblages. On the right side of each plot, mean (dot) and standard deviation (error bars) from unaltered McLeod quartz monzodiorite (QMD), Bear quartz monzonite (QM) and Luhr Hill granite (GP) samples are shown for reference.

3.4.3 Comparison between mineral and rock trace element gradients

Copper, Mo, Te, Se, Bi, Sb, As, W, Sn, Li and Tl occur in anomalous concentrations in altered rock from the zone of potassic, sericitic and shallow-level advanced argillic alteration that represents the near-vertical pathway or plume of magmatic-hydrothermal fluids as identified by previous geologic, rock alteration, and geochemical studies (Dilles and Einaudi, 1992; Dilles et al., 2000a; Lipske and Dilles, 2000). Of these elements, W, Sn and Tl are found in concentrations of 1-5 ppm in most muscovite/illite grains analyzed and Li is enriched in chlorite (average 50 pm). Copper is also detected in chlorites but at levels (average 280 ppm) that are too low to contribute significantly to the observed Cu anomaly in rock (>1000 ppm). Chalcophile elements Mo, As, Te, Se, Bi are rarely detected in white mica/illite or chlorite in concentrations greater than 1 ppm and commonly greater than 50% of analyses are below the detection limit.

Trace element gradients in altered rocks generally mimic gradients in mineral trace element compositions. Traverse plots were constructed by plotting the estimated sample depth versus the trace element content of minerals and corresponding rock analyses (Figure 3.11-3.13). Paleodepth was estimated using the relative position samples within the reconstructed cross section (Figure 3.2). Two traverses are plotted: a vertical traverse moving ~N70° W from above the ore zone at ~ 3 km depth to 0.2 km below the approximate paleosurface and a lateral traverse at ~ 2.5 km paleodepth moving ~S20° W from the ore zone to outlying exposures ~ 2 km away (Figure 3.2).

3.4.3.1 Trace element gradients in muscovite and illite

Rubidium and cesium are detected in muscovite and illite throughout the system but do not show strong spatial gradients in mineral or rock chemistry. Barium in muscovite and illite is slightly enriched in muscovite and illite from ~ 2.5 to 2 km and in muscovite at < 1 km paleodepth. Thallium is enriched in muscovite and illite throughout the system but anomalous in only one sample from the mineral and rock data set from the top of the section at < 0.3 km paleodepth. Tungsten and tin are strongly enriched in muscovite from 1.8 – 2.2 and 1.5 – 2.0 km paleodepth, respectively and corresponding rock samples reflect this pattern (Figure 3.11).

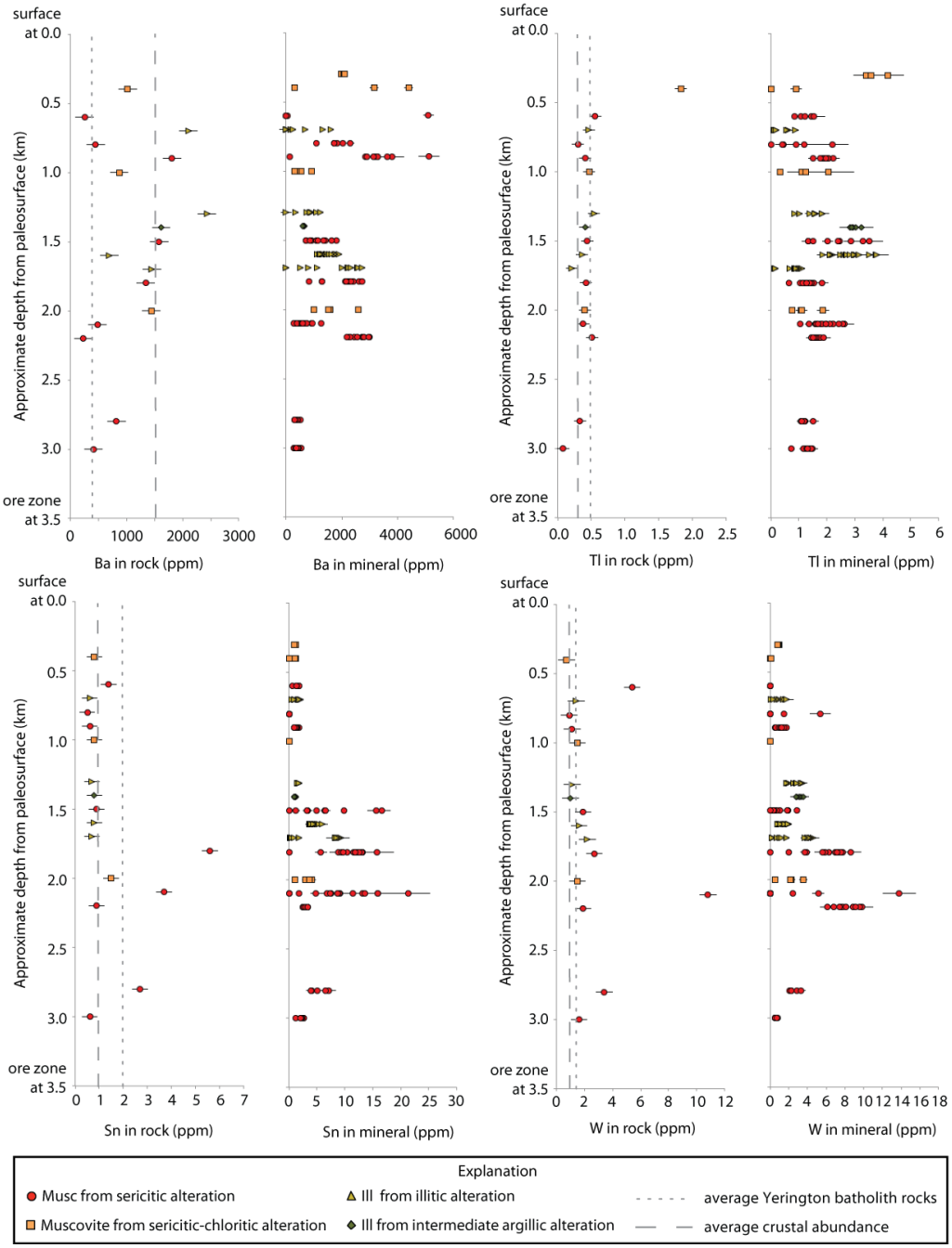

Figure 3.11. Vertical traverse plots of rock and muscovite and illite trace element contents (ppm) from ore zone at 3.5 km (A) to paleosurface (A') along the pathway of the magmatic fluid plume (Figure 3.2). Colors and symbols represent alteration type; error bars show standard error for ICP-MS/AES and standard error including uncertainty in calibration standard from LA-ICP-MS. Dashed lines represent average composition of Yerington batholith rocks and dotted line represents average crustal abundance.

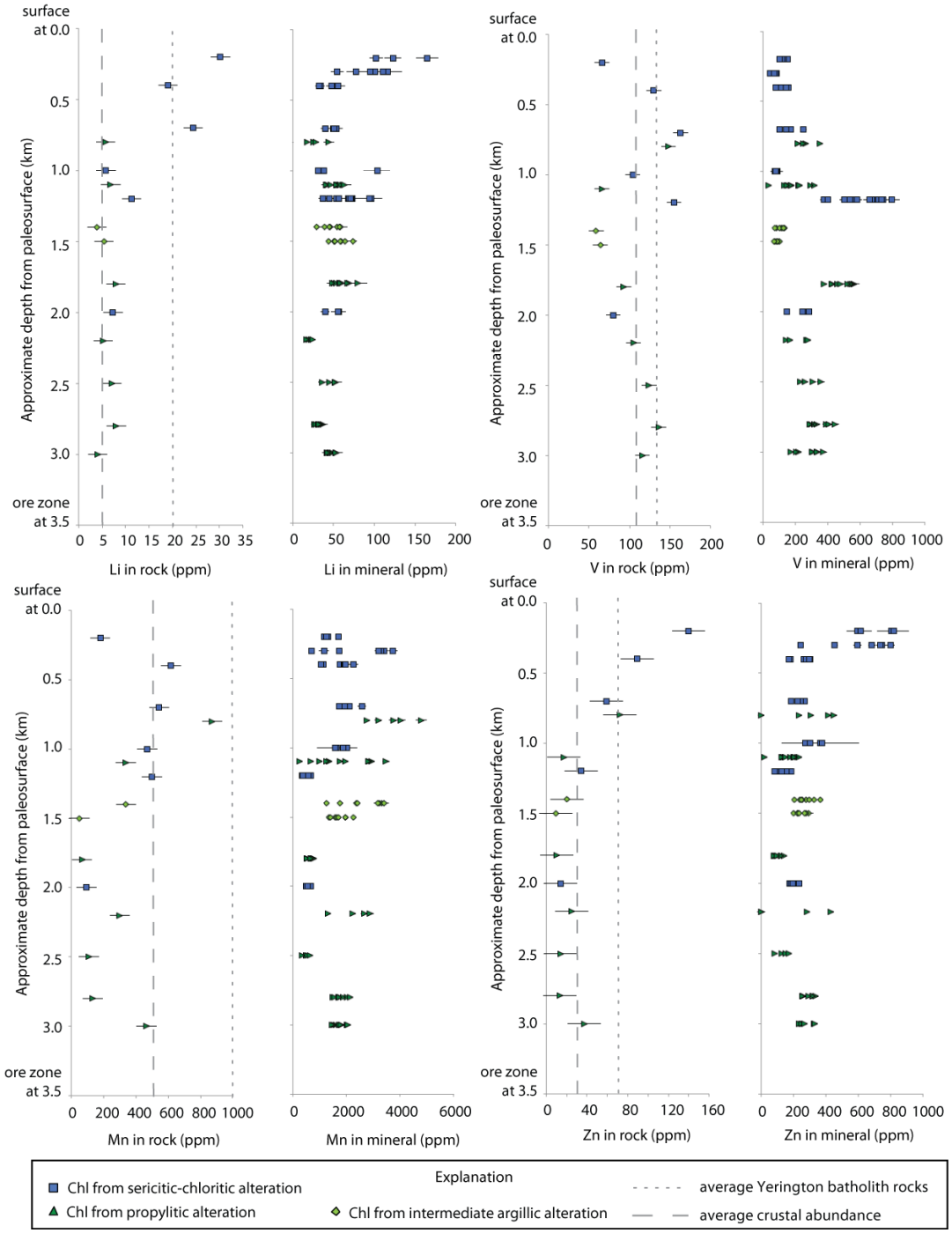

Figure 3.12. Vertical traverse plots of rock and chlorite trace element contents (ppm) from ore zone at 3.5 km (A) to paleosurface (A') along the pathway of the magmatic fluid plume (Figure 3.2). Colors and symbols represent alteration type; error bars show standard error for ICP-MS/AES and standard error including uncertainty in calibration standard from LA-ICP-MS. Dashed lines represent average composition of Yerington batholith rocks and dotted line represents average crustal abundance.

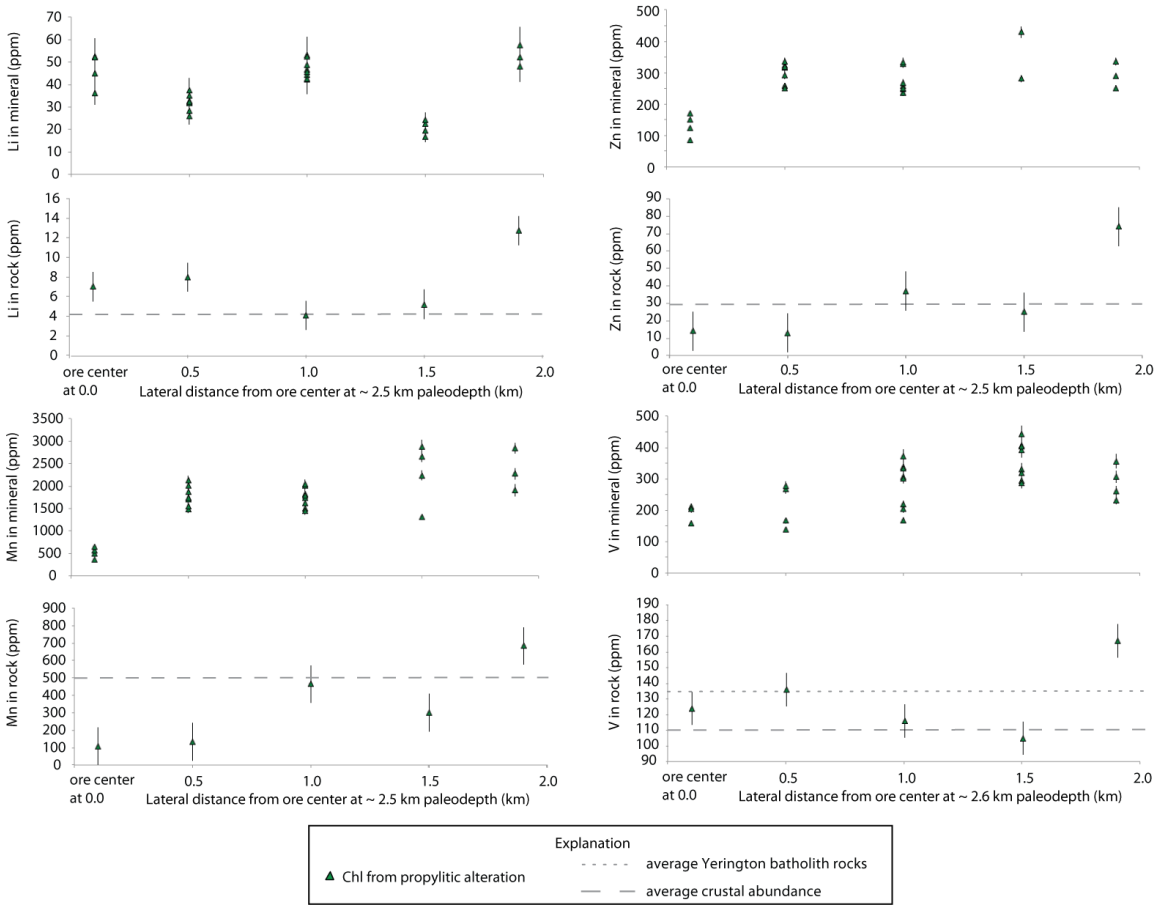

Figure 3.13. Lateral traverse plots of rock and chlorite trace element contents (ppm) at 2.5 km paleodepth from ore zone (B) to 2.0 km away (B') (Figure 3.2). All samples are from propylitic alteration, error bars show standard error for ICP-MS/AES and standard error including uncertainty in calibration standard from LA-ICP-MS. Dashed lines represent average composition of Yerington batholith rocks and dotted line represents average crustal abundance.

3.4.3.2 Trace element gradients in chlorite

Moving vertically away from the ore zone along the path of the magmatic fluid plume, Li and Zn are removed from rocks near the ore zone and enriched in chlorites and corresponding samples at <1 km paleodepth compared to samples from deeper exposures, average unaltered rock concentrations from the Yerington batholith and average crustal abundance (Table 3.2). Manganese is slightly higher in chlorite and rocks from samples located above ~1.5 km and several chlorite and rock samples between 1 and 2 km are

enriched in V (Figure 3.12). Moving laterally away from the ore center at ~ 2.5 km paleodepth, V, Zn and Mn increase in chlorite and corresponding rock samples and are lowest in the sample from drill core. Lithium content is equal in distal and proximal samples (Figure 3.13).

3.4.4 Mass balance

A simplified mass balance method is used to quantitatively compare mineral trace element concentrations to whole rock composition. Three samples are used, one from sericitic (qtz-musc) alteration (YD08-21), one from propylitic (chl-act-epid) alteration (YD01-04) and one from sericitic-chloritic (chl-musc-hem) alteration (YD01-13A). Relative mineral proportions by volume (vol $frac_{min}$) were estimated by petrography (Chapter 2). Mineral mass fractions (mass $frac_{min}$) for each sample were determined by multiplying mineral volume fraction by mineral density (ρ_{min}) (Deer et al., 1992) and renormalizing to the total calculated mass. For sericitic alteration, where muscovite is the only aluminum-bearing phase, proportions were crosschecked by comparing the Al_2O_3 content (wt. %) in the whole rock to the average Al_2O_3 content of muscovite determined by EMPA multiplied by the estimated muscovite mass fraction.

Once mineral mass fractions of each mineral in the sample were calculated, average trace element concentrations from LA-ICP-MS analyses for muscovite or chlorite were multiplied by the mineral mass fraction to calculate the contribution by muscovite or chlorite of each trace element to the whole rock composition as shown in equation (1). For example, a sample containing 50% muscovite by mass (mass $frac_{musc}$ = 0.5) and an average concentration of Ba in muscovite of 1000 ppm ($[Ba]_{musc}$ = 1000 ppm), yields a predicted contribution of Ba by muscovite to the whole rock composition of 500 ppm ($[Ba]_{rock}$ = 500 ppm).

(1) $$[X_{rock},ppm] = [X_{mineral},ppm] \bullet [MassFrac_{mineral\ in\ rock}]$$

Mineral mass fractions multiplied by mineral trace element concentrations are plotted versus whole rock trace element concentrations in Figure 3.14. These plots show relative trace element abundances within a sample, the estimated amount of a given trace element contributed by muscovite or chlorite and the estimated contribution of trace elements by other minerals within a sample (Figure 3.14).

There are several significant sources of error in this analysis including the accuracy of the estimated volume fractions by petrographic analysis and sampling error due to the difference in scale between rock and mineral analyses. Other sources of error include analytical error from LA-ICP-MS analyses of the minerals and ICP-MS/AES analyses of the whole rock. Taking these errors into account, mass balance plots can be used to approximate the contribution by muscovite and/or chlorite to the whole rock trace element chemistry.

In the sample from strong sericitic alteration (YD08-21), muscovite contribution (0.26 mass fraction$_{musc}$) can account for all of Rb, V and Ba and greater than 50% of the Tl and Sc measured in the whole rock chemistry (Figure 3.14a). Titanium, Cu, P concentrations in the whole rock analysis cannot be attributed to muscovite. Titanium is likely contributed by rutile, P by apatite, which is a common trace phase, and the anomalous Cu values may be due to chrysocolla, a supergene Cu-silicate noted in hand sample. Approximately 25% of W, Cs, Co and Li contents and less than 10% of Mn, Zn, Cr, Co and Sr concentrations detected in rock analyses can be attributed to muscovite and these elements must also substitute into another mineral such as one of the trace phases mentioned above. Elements below detection levels in muscovite but above the detection limit in the rock analysis include the chalcophile and ore metals As, Se, Mo, Pb, Bi and Sn that were most likely originally contained in hypogene sulfides and are sequestered in oxide phases in the supergene environment. Uranium and thorium in muscovite were not measured for this sample.

For the sample from propylitic alteration (YD01-04), chlorite (0.10 mass fraction) contribution can account for all the Zn, Mn, Li and Co in the sample and greater than 50% of the Co and Cu. Approximately 25% of V, Cr, Rb and Tl concentrations from the rock analyses can be attributed to chlorite. All other trace elements (Ti, P, Ba, Pb, Cr, As, Th, U, W, Sn, Mo, Bi, Te) lie between the 1:10 and 1:100 lines indicating less than 10% of their whole rock concentrations can be accounted for by chlorite (Figure 3.14b). Titanium, P, Pb, Th, U, Cr, As, Te, Bi, W, Sn and Mo are likely contained in similar trace phases as in YD01-21 (rutile, apatite and Fe-oxides). Barium and strontium are probably hosted in feldspars or calcic phases actinolite or epidote.

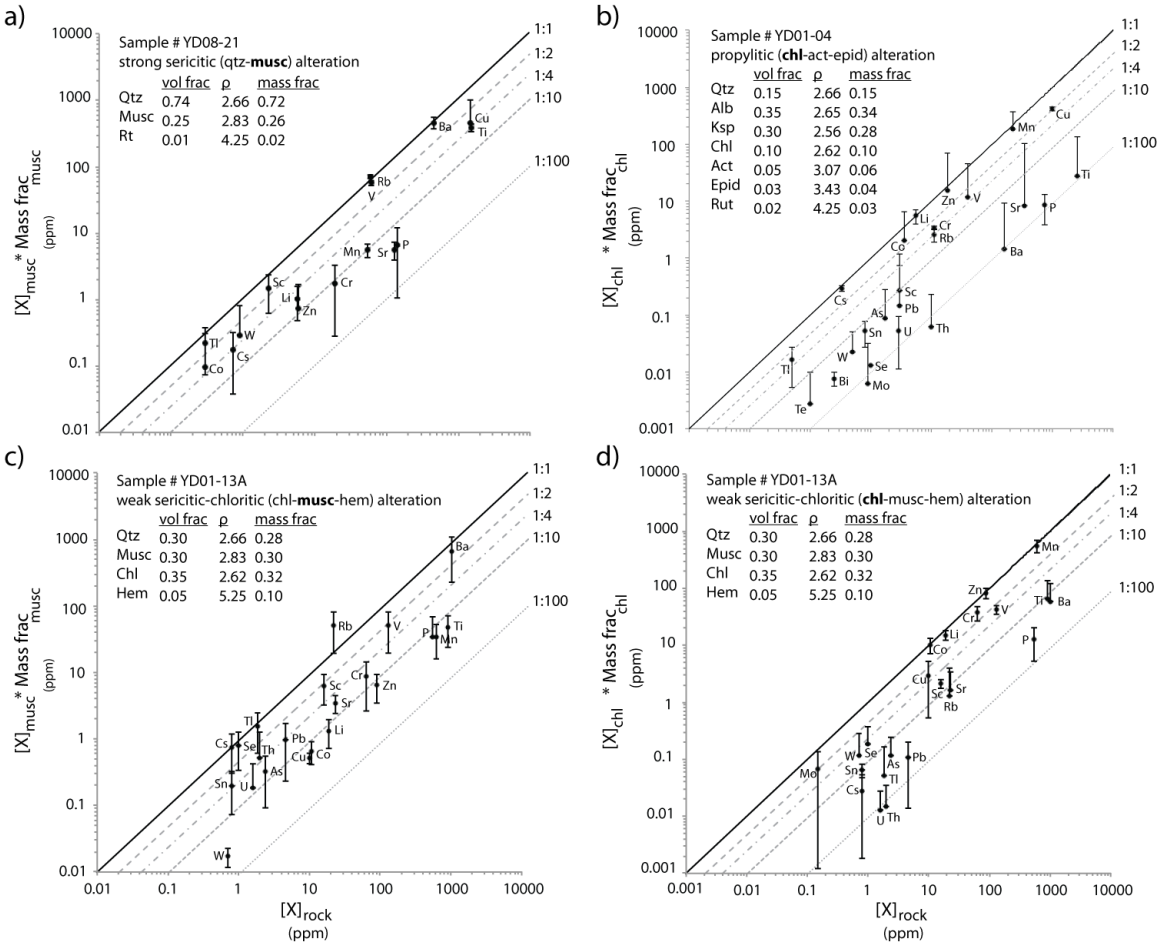

Figure 3.14. Mass balance plots for selected samples: a) muscovite from YD08-21, b) chlorite from YD01-04, c) muscovite from YD01-13A and d) chlorite from YD01-13A. Dots represent mean values and error bar lengths are equal to ± 1 standard deviation of all spots analyzed for each samples with data quality ≥ 2.0. The solid line represents the 1:1 ratio where the mineral contribution accounts for all (100%) of the trace element concentration measured in the rock. The dashed lines represent decreasing ratios [1:2 (50%), 1:4(25%), 1:10(10%), 1:100 (1%)].

The simplified mass balance results for muscovite from the sample with sericitic-chloritic alteration (YD01-13A) are similar to the results for muscovite from strong sericitic alteration. Muscovite contribution (0.30 mass fraction$_{musc}$) can account for all Ba, Tl, Se and Cs and greater than 50% of the V, Sn and Sc measured in the whole rock geochemistry (Figure 3.14c). Rubidium for this sample lies above the 1:1 ratio line and is disregarded due to error. Tellurium and bismuth concentration are below the limit of

detection in the whole rock and muscovite analyses. Trace element concentration in chlorite from the sample with sericitic-chloritic alteration (0.32 mass fraction) can account for all measured Zn, Mn, Co and >80% of Li in the sample and greater than 50% Cr. Between 25 – 50 % of Mo, Cu and V concentrations in rock can be accounted for by the mass fraction of chlorite (Figure 3.14d).

To compare the contributions of muscovite to chlorite within the sample from sericitic-chloritic alteration, the trace element concentration in muscovite multiplied by the mass contributions of muscovite and chlorite for each trace element are normalized to the whole rock concentration of the element for sample YD01-13A (Figure 3.15). Figure 3.15 illustrates which elements prefer muscovite to chlorite, vice versa or another phase in the sample. Chlorite dominates contributions (>80%) of Li, Mn, Zn and Co whereas muscovite contributes > 80% of Cs, Tl, Se and ~ 65% of Ba. Muscovite and chlorite contribute equal fractions of V (~40%). Scandium, Cr, Cu and Mo concentrations can be partly attributed to muscovite and/or chlorite but must also be hosted in another phase such as hematite in order to account for their concentration in the rock analysis. Elements that lie close to origin are present in low amounts (< 20 %) in muscovite and chlorite and must primarily be hosted in other minerals such as rutile, apatite, hematite or supergene oxides. Bismuth and tellurium are below detection in both mineral and rock analyses.

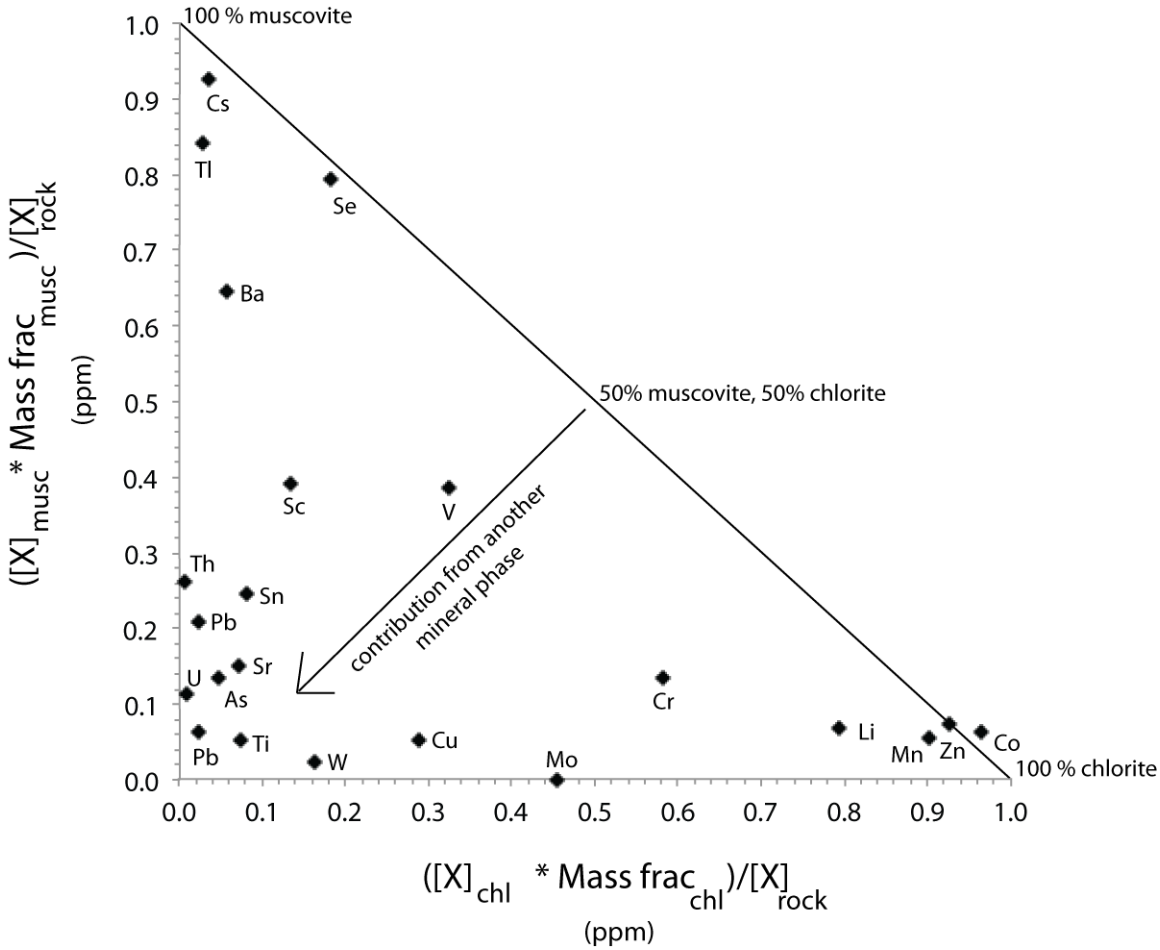

Figure 3.15. Mass balance plot comparing the contributions of muscovite and chlorite to whole rock trace element content of sample YD01-13A. Symbols represent mean values.

3.5 Discussion

3.5.1 Summary of trace element gradients in rocks and minerals

Copper, Mo, W, Sn, Se, Te, Bi, Sb, Li and Tl are enriched in rock sampled along the zone of potassic, sericitic and advanced argillic alteration that represents the near-vertical pathway of the magmatic hydrothermal plume extending from above the ore zone at ~3.5 km depth upward to the surface environment (Figure 3.16). Of these elements, W, Sn and Tl are found in muscovite and Li in chlorite from samples of sericitic alteration. In addition, mineral and rock concentrations vary along similar gradients confirming W, Sn, Tl and Li anomalies in rock chemistry record the pathway of the magmatic fluid plume (Figure 3.17).

Manganese, Co and Ni are depleted in altered rock near the ore zone and redistributed to distal alteration zones outside the studied area (Figure 3.15). Zinc is also depleted from alteration near the ore zone (<40 ppm) but is enriched (80-140 ppm) in samples from less than 1 km paleodepth. This relative enrichment of Zn is likely redistributed Zn removed from igneous mafic silicates such as biotite and hornblende during alteration.

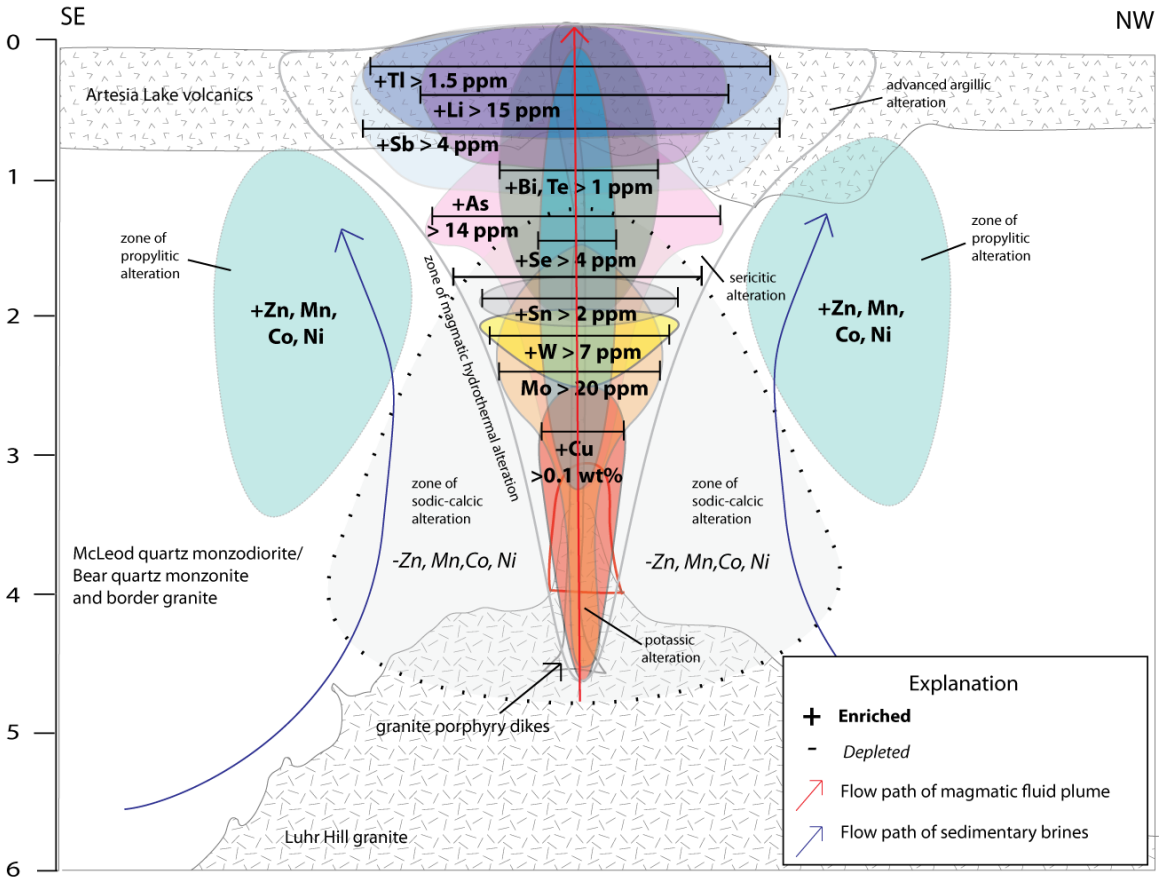

Figure 3.16. Summary figure showing distribution of trace elements as measured in rock chemistry on a cartoon cross-section through the Ann-Mason porphyry copper deposit. Colored shapes represent the spatial extent of trace element anomalies (Table 3.2). The red arrow indicates the path of the magmatic fluid plume while the blue arrow indicates the path of circulating sedimentary brines.

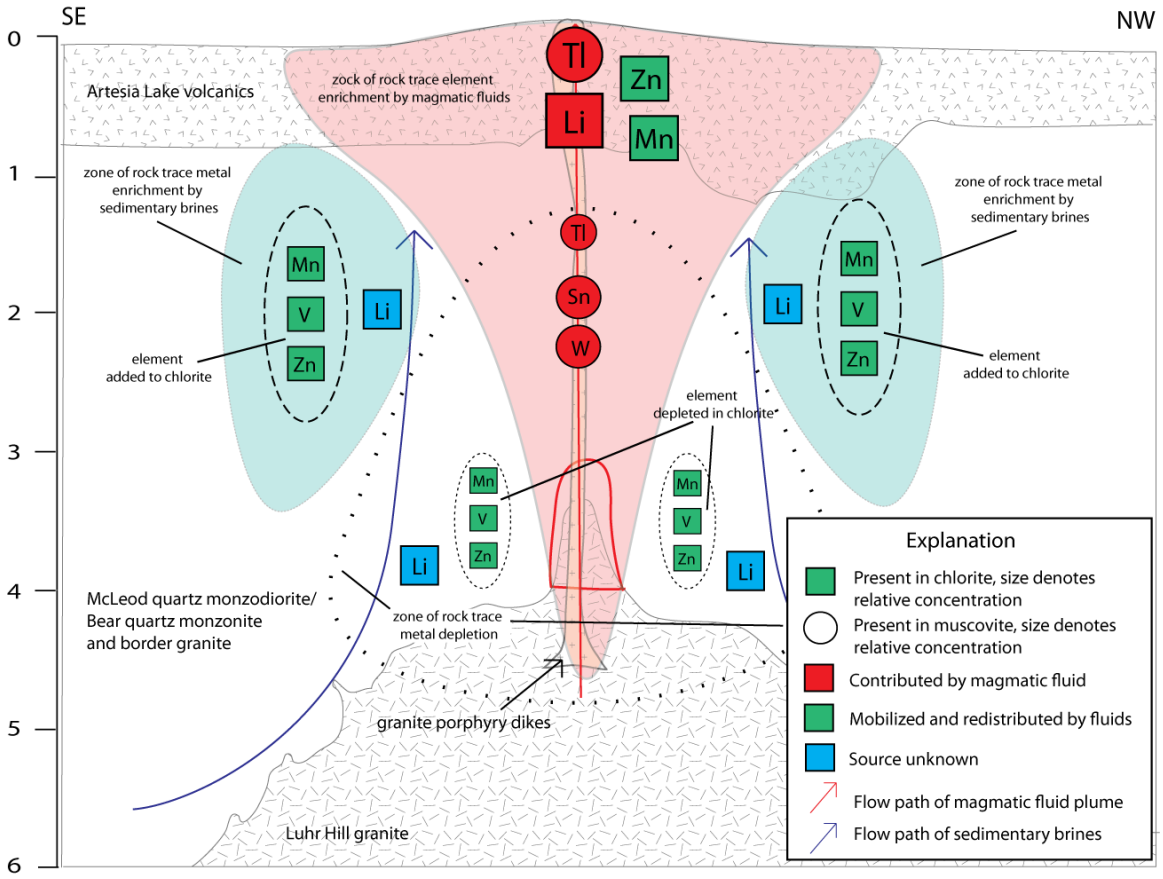

Figure 3.17. Summary of trace element gradients in white mica and chlorite displayed on a cartoon paleo cross-section of Ann-Mason porphyry copper deposit. Elements enclosed in squares are detected in chlorite while elements encircled are found in muscovite. The size of the symbol indicates the relative abundance and the color distinguishes elements added by magmatic fluids from elements mobilized and redistributed by sedimentary brines. Shaded areas outline zones of magmatic and non-magmatic hydrothermal alteration. Arrows indicate fluid flow paths.

In the simplified mass balance calculations previously described, Tl contents in muscovite can account for all Tl measured in the rock chemistry for both samples containing muscovite. Thallium, as a +1 cation (Tl^{+}), has a similar atomic radius in 12-fold coordination (1.70 Å) to K^{+} (1.64 Å) (Shannon, 1976) and can substitute into the interlayer cation site in muscovite. The positive correlation of Tl and Rb concentrations in muscovite and illite is evidence for this type of substitution since previous research

(e.g. Armbrust et al, 1977) has demonstrated Rb substitutes for K in muscovite and K-feldspar (Figure 3.18).

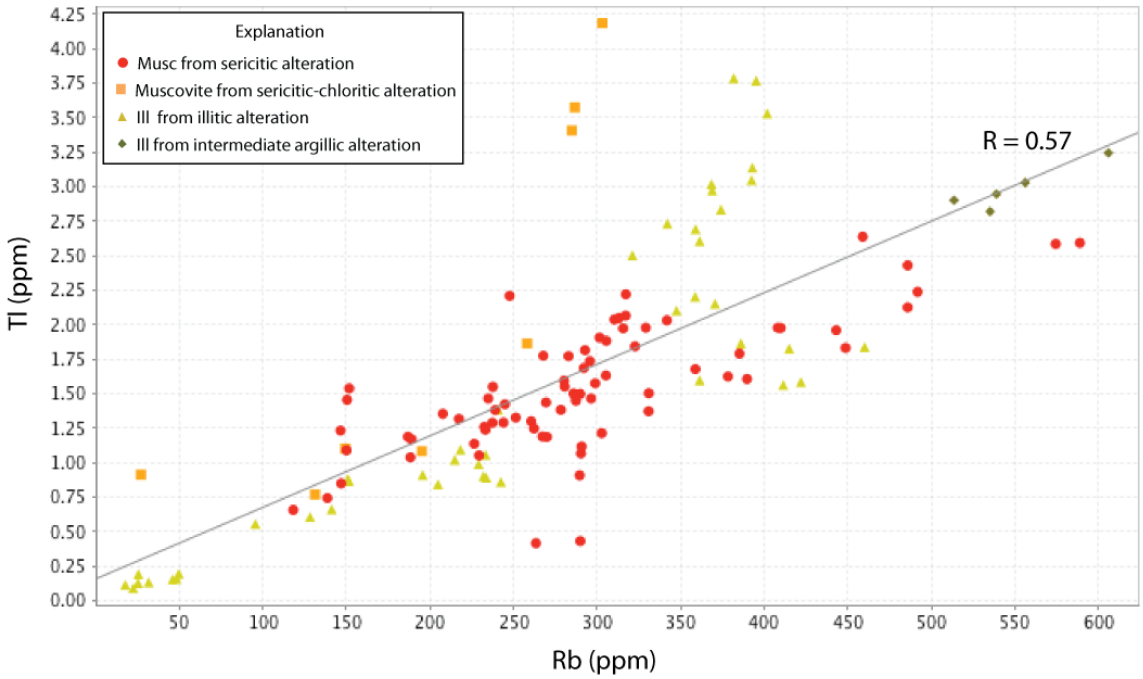

Figure 3.18. Plot of Tl concentrations (ppm) versus Rb concentations (ppm) in muscovite and illite determined by LA-ICP-MS.

Although chalcophile behavior for Tl is commonly observed in the partitioning of Tl into sulfide melts and Tl enrichment in sulfide minerals from magmatic and hydrothermal environments (Heinrichs et al., 1980; Shaw, 1952), lithophile behavior and the substitution of Tl^{+} into K-bearing minerals has also been recently documented in sericitic and argillic alteration from porphyry-Cu deposits in the Collahuasi Formation in Northern Chile (Baker et al., 2010) and historically documented in muscovite from ore deposits of the Caucasus region in Eastern Europe (Wedepohl, 1978). Thallium is found in all muscovite and illite analyzed and, in the samples used for the mass balance, at concentrations that can account for all of the Tl in the rock. This suggests the Tl anomaly in the upper 1 km of the hydrothermal system at Yerington, Nevada could be explained entirely by Tl enrichment in muscovite. This does not exclude the possibility that Tl is

also enriched in pyrite. Pyrite was not analyzed and neither of the samples from the mass balance calculations contained relic sulfide or abundant goethite.

Tungsten and tin concentrations in rock could only partially be attributed to muscovite in the samples analyzed by the mass balance method suggesting W and Sn distributions are complicated and not hosted solely in muscovite. Tungsten is commonly found in trace amounts in micas (5 - 50 ppm) and is present in muscovites in altered granites near tungsten deposits in concentrations as high as 500 ppm (Wedepohl, 1978). Tetrahedral-coordinated $W^{6+(iv)}$(0.42 Å) could substitute into the muscovite structure and replace $Al^{(iv)}$ (0.39 Å) or octahedral-coordinated $W^{6+(vi)}$ (0.60 Å), a slightly larger ion, may replace $Al^{(vi)}$ (0.54 Å) (Shannon, 1976). Either substitution would have to be coupled to maintain neutral charge within the mineral.

$Tin^{4+(vi)}$ (0.71 Å) preferentially substitutes for $Ti^{4+(vi)}$ (0.68 Å) or $Fe^{3+(vi)}$ (0.64 Å) in rutile, biotite and hornblende (Ahrens, 1952). Fine-grained muscovite replacing biotite in in rare metal deposits in granite massifs of central Kazakstan was found to have higher Sn (1240 ppm) than coarse-grained igneous muscovite (580 ppm) (Ganeev et al., 1961). These Sn concentrations are two orders of magnitude higher than those found in muscovite from our study (1-5 ppm) but muscovite replaces biotite and hydrobiotite in sericitic alteration so the mechanism for Sn enrichment may be similar.

Lithium, as octahedral-coordinated $Li^{+(vi)}$ (0.76 Å), substitutes for $Mg^{2+(vi)}$ (0.72 Å) (Shannon. 1976) in chlorite via a coupled substitution with Al^{3+} ($Li^{+} + Al^{3+} <-> 2Mg^{2+}$). All minerals, including chlorites, become more aluminous through alteration with acidic fluids as demonstrated in Chapter 2. Therefore, it was hypothesize Li concentrations would increase with the Al content of chlorites and would be highest in chlorites from sericitic-chloritic alteration. Although Li concentrations are slightly higher (~20 ppm) in chlorite from sericitic-chloritic alteration than chlorite from propylitic alteration (Table 3.4), Li is present in all chlorite analyzed at highly anomalous concentrations greater than 40 ppm.

The relative enrichment of Li in rock chemistry (up to 90 ppm) at the paleosurface may be due to an increase in the chlorite proportion in alteration assemblages as a result of changes in wall-rock lithology. The primary rock unit in the upper portion of Blue Hill and in the Buckskin Range is the Artesia Lake volcanics, a suite of extrusive

volcanic and volcanoclastic rocks, that are more mafic (~51 wt% SiO2 in Artesia Lake basalt) than the rocks of the Yerington batholith (~58 – 69 wt% SiO2) (Dilles, 1987) with higher modal abundances of mafic minerals. These rocks alter to a chlorite-muscovite-hematite assemblage during sericitic alteration with ~ 35 vol % chlorite. This is significantly greater than the 5-20 vol % chlorite typical of propylitic alteration. Therefore, the pattern of Li enrichment could be due to a combination of higher Li concentrations in more aluminous chlorites and an overall increase the abundance of chlorite due to differences in wall-rock lithology.

3.5.2 Controls on trace element gradients in altered rocks and minerals

Research has demonstrated that some metals (e.g. Mo, Zn, Mn) are transported as metal chloride complexes in porphyry copper ore fluids and the ability of an element to segregate into the magmatic volatile phase is largely based on Cl^- affinity (Candela and Holland, 1986; Holland, 1972). Trace element gradients in the zone of magmatic hydrothermal alteration may be partially explained by changes in the Cl^- concentration of the magmatic plume due to vapor-brine separation during fluid ascent. Elements such as Sn^{4+} and W^{6+} form polyatomic chloride complexes and require high Cl^- activities for efficient transport. These elements are likely transported in high salinity magmatic brines. Volatile elements such as Li^+ and Tl^+ can form Cl-complexes at lower Cl^- activities and could be transported in a low salinity vapor phase. In one scenario, the magmatic volatile phase released from the top of the Luhr Hill granite cupola at 3.5 km paleodepth (~1.2 kbars) and 700°C ascends, crosses the critical curve (Bodnar et al., 1985) and undergoes vapor-brine separation. Volatile elements (e.g. Li, Tl) are segregated into the vapor phase while highly charged cations (e.g. W, Sn) remain in the brine. This could be one explanation for the observed enrichment of W and Sn in alteration 1-2 km away from the ore zone (~1.5 – 2 km) and the Li and Tl anomalies greater 2.5 km from the top of the granite cupola and confined near the paleosurface at <1 km depth.

3.6 Conclusion

Trace metal contents of white mica, illite and chlorite from magmatic-hydrothermal alteration can be use to link gradients in rock chemistry to the pathway of ore-forming fluids. In this study, the compositions of altered wall-rock surrounding the Ann-Mason porphyry-Cu(Mo) deposit at Yerington, Nevada were determined by ICP-MS/AES and trace element concentrations in muscovite, illite, mixed muscovite-paragonite, pyrophyllite and chlorite were measured in situ by LA-ICP-MS. Copper, Mo, Te, Se, Bi, Sb, As, W, Sn, Li and Tl are enriched rocks from the zone of potassic, sericitic and/or shallow-level advanced argillic alteration that represents the path of magmatic fluid from the ore zone (3.5 km depth) to the paleosurface. Zinc, Mn, Co and Ni are depleted in altered rock in and adjacent to the ore zone and mobilized by magmatic and non-magmatic hydrothermal fluids. These elements are fixed in the distal propylitic alteration and in the near surface environment.

Mineral trace element concentrations are quantitatively compared to whole rock compositions using a simplified mass balance method. Findings show chlorite contributes Li, Mn, Zn and Co while muscovite contributes Ba, Rb and Tl. Of the elements anomalous in rock affected by sericitic and advanced argillic alteration, W, Sn and Tl enrichment can be attributed, at least partially, to muscovite and illite. The enrichment of Li in rock chemistry near the paleosurface (< 1 km depth) may be due to a combination of increased Li content in chlorite and an increase in the proportion of chlorite in alteration due to differences in wall-rock lithology. Copper is detected in chlorites but at levels (average 280 ppm) that are too low to contribute significantly to the observed Cu anomaly in rock (>1000 ppm). Chalcophile elements Mo, Te, Se, Bi are rarely detected in white mica/illite or chlorite in concentrations greater than 1 ppm and commonly more than 50% of analyses are below detection.

3.7 References

Armbrust, G.A., Oyarzun, J., Arias, J., 1977, Rubidium as a guide to ore in Chilean porphyry copper deposits: Economic Geology, v. 72, p.1086-1100.

Ahrens, L. H., 1952, The use of ionization potentials. Part 1. Ionic radii of the elements.: Geochimica et Cosmochimica Acta, v. 2, p. 155-169.

Bailey, S., 1984, Micas, Chelsea, Mineralogical Society of America, Reviews in Mineralogy.

Baker, R. G. A., Rehkämper, M., Ihlenfeld, C., Oates, C. J., and Coggon, R., 2010, Thallium isotope variations in an ore-bearing continental igneous setting: Collahuasi Formation, northern Chile: Geochimica et cosmochimica acta, v. 74, no. 15, p. 4405-4416.

Barnes, H. L., 1975, Zoning of ore deposits: types and causes.: Transactions of the Royal Society in Edinburgh, v. 69, p. 295-311.

Bodnar, R. J., Burnham, C. W., and Sterner, S. M., 1985, Synthetic fluid inclusions in natural quartz. III Determination of phase equilibrium properties in the system H2O-NaCl to 1000 C AND 1500 bars: Geochimica et Cosmochimica Acta, v. 49, p. 1871-1873.

Candela, P., and Holland, H., 1986, A mass transfer model for copper and molybdenum in magmatic hydrothermal systems; the origin of porphyry-type ore deposits: Economic Geology, v. 81, no. 1, p. 1.

Dilles, J. H. and Einaudi, M., 1992, Wall-rock alteration and hydrothermal flow paths about the Ann-Mason porphyry copper deposit, Nevada; a 6-km vertical reconstruction: Economic Geology, v. 87, no. 8, p. 1963.

Dilles, J. H., and Proffett, J. M., 1995, Metallogenesis of the Yerington batholith, Nevada: Arizona Geological Society Digest, v. 20, p. 306-315.

Dilles, J. H., Solomon, G., Taylor, H., and Einaudi, M., 1992, Oxygen and hydrogen isotope characteristics of hydrothermal alteration at the Ann-Mason porphyry copper deposit, Yerington, Nevada: Economic Geology, v. 87, no. 1, p. 44.

Dilles, J. H., Einaudi, M. T., Proffett, J. M., and Barton, M. D., 2000a, Overview of the Yerington porphyry copper district: magmatic and non-magmatic sources of hydrothermal fluids, their flow paths, alteration affects on rocks, and Cu-Mo-Fe-Au ores: Society of Economic Geologist Guidebook Series, v. 32, p. 55-66.

Dilles, J. H., Proffett, J. M., and Einaudi, M. T., 2000b, Magmatic and hydrothermal features of the Yerington batholith with emphasis on the porphyry Cu(Mo) deposit in the Ann-Mason area: Society of Economic Geologist Guidebook Series, v. 32, p. 67-89.

Dilles, J. H., 1987, Petrology of the Yerington Batholith, Nevada; evidence for evolution of porphyry copper ore fluids: Economic Geology, v. 82, no. 7, p. 1750.

Emmons, W. H., 1918, The Principles of Economic Geology, York, The Maple Press Compony.

Ford, J., 1978, A chemical study of alteration at the Panguna porphyry copper deposit, Bougainville, Papua New Guinea: Economic Geology, v. 73, no. 5, p. 703.

Guilbert, J. M., and Park, C. F., 1986, The Geology of Ore Deposits, Long Grove, Waveland Press, Inc.

Gustafson, L., and Hunt, J., 1975, The porphyry copper deposit at El Salvador, Chile: Economic Geology, v. 70, no. 5, p. 857.

Heinrichs, H., Schulz-Dobrick, B., and Wedepohl, K., 1980, Terrestrial geochemistry of Cd, Bi, Tl, Pb, Zn and Rb: Geochimica et cosmochimica acta, v. 44, no. 10, p. 1519-1533.

Holland, H. D., 1972, Granites, solutions and base metal deposits: Economic Geology, v. 67, p. 281-301.

Kent, A. J. R., Jacobsen, B., Peate, D. W., Waight, T. E., and Baker, J. A., 2004, Isotope Dilution MC-ICP-MS Rare Earth Element Analysis of Geochemical Reference Materials NIST SRM 610, NIST SRM 612, NIST SRM 614, BHVO-2G, BHVO-2, BCR-2G, JB-2, WS-E, W-2, AGV-1 and AGV-2: Geostandards and Geoanalytical Research, v. 28, no. 3, p. 417-429.

Le Gleuher, M., Anand, R. R., Eggleton, R. A., and Radford, N., 2008, Mineral hosts for gold and trace metals in regolith at Boddington gold deposit and Scuddles massive copper-zinc sulphide deposit, Western Australia: an LA-ICP-MS study: Geochemistry: Exploration, Environment, Analysis, v. 8, no. 2, p. 157.

Lipske, J., 2002, Advanced argillic and sericitic alteration in the Buckskin Range, Nevada: a product of ascending magmatic fluids from the deeper yerington porphyry copper environment [M.S.: Oregon State University.

Lipske, J., and Dilles, J., 2000, Advanced argillic and sericitic alteration in the subvolcanic environment of Yerington Porphyry Copper System, Buckskin Range, Nevada: Part I. Contrasting Styles of Intrusion-Associated Hydrothermal Systems, v. 32, p. 91-99.

Proffett, J., 1977a, Cenozoic geology of the Yerington District, Nevada, and implications for nature and origin of Basin and Range faulting: Geological Society of America Bulletin, v. 88, no. 2, p. 247-266.

Proffett, J. M., and Dilles, J. D., 1984, Geologic map of the Yerington District, Nevada, Nevada Bureau of Mines and Geology.

Shannon, R. D., 1976, Revised effective ionic radii and systematic studied of interatomic distances in halides and chalcogenides: Acta Cryst., v. 32, p. 751-767.

Shaw, D. M., 1952, The geochemistry of thallium: Geochimica et cosmochimica acta, v. 2, no. 2, p. 118-154.

Van Lichtervelde, M., Gregoire, M., Linnen, R. L., Beziat, D., and Salvi, S., 2008, Trace element geochemistry by laser ablation ICP-MS of micas associated with Ta mineralization in the Tanco pegmatite, Manitoba, Canada: Contributions to Mineralogy and Petrology, v. 155, no. 6, p. 791-806.

Wedepohl, K., 1978, Handbook of Geochemistry, New York, Springer.

Chapter 4: Conclusion

The goal of this research is to improve understanding in the relationship between results from large-scale ore deposit exploration techniques and the expression of ore deposit formation in wall-rock and alteration minerals in order to improve exploration methods and identify their limitations. Two broad sampling techniques are explored, (1) short wave infrared (SWIR) spectroscopy and (2) bulk rock sampling to identify geochemical anomalies. The Ann-Mason porphyry copper deposit at Yerington, NV was chosen as a study location because it is easy to determine the position of sample locations relative to the ore body due to the exposure, in cross-section, of a porphyry copper center from the batholith to the volcanic environment.

SWIR spectra from rock samples are compared to the composition of white mica, illite and chlorite from magmatic hydrothermal alteration zones. The results of this study show SWIR spectroscopy can be used to identify variations in the aluminum content of white micas, which may be used as to map fluid pH gradients. Chlorite compositional variations could not be identified in SWIR and were likely obscured by coexisting highly reflective clays and micas.

Trace metal enrichments measured in rock chemistry and white mica, illite and chlorite are compared to test if rock anomalies can be linked to ore fluids. Enrichments of W, Sn and Tl and Li in altered rock from magmatic hydrothermal alteration zones were confirmed in white mica, illite and chlorite, respectively. Chalcophile element (Mo, Se, Te, Bi, Sb and As) anomalies were also detected in rock chemistry but not in white mica, illite or chlorite.

Several next steps in research relating to these two methods are identified below. For SWIR spectroscopy, illite overprint on high temperature muscovite complicates identification of hydrothermal mineral assemblages. A method to distinguish illite from muscovite must be determined in order to use SWIR to approximate temperature gradients. For rock anomalies, mineral hosts for chalcophile elements must be confirmed. Trace metal gradients in pyrite, another common alteration mineral deposited by ore fluids, should be determined to verify the relationship between the rock chemistry and ore deposit formation.

Bibliography

Ahrens, L. H., 1952, The use of ionization potentials. Part 1. Ionic radii of the elements.: Geochimica et Cosmochimica Acta, v. 2, p. 155-169.

Anthony, E., and Titley, S., 1994, Patterns of element mobility during hydrothermal alteration of the Sierrita poyphyry copper deposit, Arizona: Economica Geology, v. 89, p. 185-192.

Bailey, S., 1984, Micas, Chelsea, Mineralogical Society of America, Reviews in Mineralogy. Baker, R. G. A., Rehkämper, M., Ihlenfeld, C., Oates, C. J., and Coggon, R., 2010, Thallium isotope variations in an ore-bearing continental igneous setting: Collahuasi Formation, northern Chile: Geochimica et cosmochimica acta, v. 74, no. 15, p. 4405-4416.

Barnes, H. L., 1975, Zoning of ore deposits: types and causes.: Transactions of the Royal Society in Edinburgh, v. 69, p. 295-311.

Bodnar, R. J., Burnham, C. W., and Sterner, S. M., 1985, Synthetic fluid inclusions in natural quartz. III Determination of phase equilibrium properties in the system H2O-NaCl to 1000 C AND 1500 bars: Geochimica et Cosmochimica Acta, v. 49, p. 1871-1873.

Candela, P., and Holland, H., 1986, A mass transfer model for copper and molybdenum in magmatic hydrothermal systems; the origin of porphyry-type ore deposits: Economic Geology, v. 81, no. 1, p. 1.

Carrillo-Rosua, J., Morales-Ruano, S., Esteban-Arispe, I., and Hach-Ali, P. F., 2009, Significance of Phyllosilicate Mineralogy and Mineral Chemistry in an Epithermal Environment. Insights from the Palai-Islica Au-Cu Deposit (Almeria, Se Spain): Clays Clay Miner., v. 57, no. 1, p. 1.

Carten, R., 1986, Sodium-calcium metasomatism; chemical, temporal, and spatial relationships at the Yerington, Nevada, porphyry copper deposit: Economic Geology, v. 81, no. 6, p. 1495.

Changyun, L., Ge, Z., and Chunhua, Y., 2005, Application of SWIR reflectance spectroscopy to the Pulang porphyry copper deposit, Yunnan, China: Mineral Deposits (Kuangchuang Dizhi), v. 24, no. 6, p. 621-637.

Clark, R. N., Swayze, G. A., Wise, R. A., Livo, K. E., Hoefen, T. M., Kokaly, R. F., and Sutley, S. J., 2007, USGS digital spectral library splib06a, Reston, U. S. Geological Survey, U. S. Geological Survey Data Series.

Deer, W. A., Howie, R. A., and Zussman, J., 1992, An introduction to the rock-forming minerals, Essex, Pearson Education Limited.

Di Tommaso, I., and Rubinstein, N., 2007, Hydrothermal alteration mapping using ASTER data in the Infiernillo porphyry deposit, Argentina: Ore Geology Reviews, v. 32, no. 1-2, p. 275-290.

Dilles, J. H., 1987, Petrology of the Yerington Batholith, Nevada; evidence for evolution of porphyry copper ore fluids: Economic Geology, v. 82, no. 7, p. 1750.

Dilles, J. H., and Wright, J. E., 1988, The chronology of early Mesozoic arc magmatism in the Yerington District of western Nevada and its regional implications: Geological Society of America Bulletin, v. 100, no. 5, p. 644-652.

Dilles, J. H., and Einaudi, M., 1992, Wall-rock alteration and hydrothermal flow paths about the Ann-Mason porphyry copper deposit, Nevada; a 6-km vertical reconstruction: Economic Geology, v. 87, no. 8, p. 1963.

Dilles, J. H., Proffett, J. M., and Einaudi, M. T., 2000, Magmatic and hydrothermal features of the Yerington batholith with emphasis on the porphyry Cu(Mo) deposit in the Ann-Mason area: Society of Economic Geologist Guidebook Series, v. 32, p. 67-89.

Dilles, J. H., Einaudi, M. T., Proffett, J. M., and Barton, M. D., 2000a, Overview of the Yerington porphyry copper district: magmatic and non-magmatic sources of hydrothermal fluids, their flow paths, alteration affects on rocks, and Cu-Mo-Fe-Au ores: Society of Economic Geologist Guidebook Series, v. 32, p. 55-66.

Dilles, J. H., and Proffett, J. M., 1995, Metallogenesis of the Yerington Batholith, Nevada: Arizona Geological Society Digest, v. 20, p. 306-315.

Dilles, J. H., Solomon, G., Taylor, H., and Einaudi, M., 1992, Oxygen and hydrogen isotope characteristics of hydrothermal alteration at the Ann-Mason porphyry copper deposit, Yerington, Nevada: Economic Geology, v. 87, no. 1, p. 44.

Dilles, J. H., 1987, Petrology of the Yerington Batholith, Nevada; evidence for evolution of porphyry copper ore fluids: Economic Geology, v. 82, no. 7, p. 1750.

Dilles, J. H., and Gans, P. B., 1995, The chronology of Cenozoic volcanism and deformation in the Yerington area, western Basin and Range and Walker Lane: Geological Society of America Bulletin, v. 107, no. 4, p. 474-486.

Dilles, J. H., and Wright, J. E., 1988, The chronology of early Mesozoic arc magmatism in the Yerington District of western Nevada and its regional implications: Geological Society of America Bulletin, v. 100, no. 5, p. 644-652.

Duke, E., 1994, Near infrared spectra of muscovite, Tschermak substitution, and metamorphic reaction progress: Implications for remote sensing: Geology, v. 22, no. 7, p. 621.

Einaudi, M., 1977, Petrogenesis of copper-bearing skarn at Mason Vally Mine, Yerington District, Nevada: Economic Geology, v. 72, no. 5, p. 769-795.

Emmons, W. H., 1918, The Principles of Economic Geology, York, The Maple Press Compony, 194-197 p.:

Ford, J., 1978, A chemical study of alteration at the Panguna porphyry copper deposit, Bougainville, Papua New Guinea: Economic Geology, v. 73, no. 5, p. 703.

Guilbert, J. M., and Park, C. F., 1986, The Geology of Ore Deposits, Long Grove, Waveland Press, Inc.

Gustafson, L., and Hunt, J., 1975, The porphyry copper deposit at El Salvador, Chile: Economic Geology, v. 70, no. 5, p. 857.

Hauff, P., 2002, Identification of illite polytype zoning in disseminated gold deposits using reflectance spectroscopy and X-ray diffraction-potential for mapping with imaging …: Geoscience and Remote Sensing.

Hauff, P. L., Kruse, F. A., and Madrid, R. J., 1989, Gold Exploration Using Illite Polytypes Defined By X-Ray Diffraction and Reflectance Spectroscopy: World Gold, p. 76-82.

Heinrichs, H., Schulz-Dobrick, B., and Wedepohl, K., 1980, Terrestrial geochemistry of Cd, Bi, Tl, Pb, Zn and Rb: Geochimica et cosmochimica acta, v. 44, no. 10, p. 1519-1533.

Herrmann, W., Blake, M., Doyle, M., Huston, D., Kamprad, J., Merry, N., and Pontual, S., 2001, Short wavelength infrared (SWIR) spectral analysis of hydrothermal alteration zones associated with base metal sulfide deposits at Rosebery and Western Tharsis, Tasmania, and Highway-Reward, Queensland: Economic Geology, v. 96, no. 5, p. 939.

Herrmann, W., Green, G. R., Barton, M. D., and Davidson, G. J., 2009, Lithogeochemical and stable isotopic insights into submarine genesis of pyrophyllite-altered facies at the Boco Prospect, western Tasmania: Economic Geology, v. 104, no. 6, p. 775.

Holland, H. D., 1972, Granites, solutions and base metal deposits: Economic Geology, v. 67, p. 281-301.

Hunt, G. R., and Ashley, R. P., 1979, Spectra of altered rocks in the visible and near infrared: Economic Geology, v. 74, no. 7, p. 1613.

Jones, S., Herrmann, W., and Gemmell, J. B., 2005, Short Wavelength Infrared Spectral Characteristics of the HW Horizon: Implications for Exploration in the Myra Falls Volcanic-Hosted Massive Sulfide Camp, Vancouver Island, British Columbia, Canada: Economic Geology, v. 100, no. 2, p. 273.

Kent, A. J. R., Jacobsen, B., Peate, D. W., Waight, T. E., and Baker, J. A., 2004, Isotope Dilution MC-ICP-MS Rare Earth Element Analysis of Geochemical Reference Materials NIST SRM 610, NIST SRM 612, NIST SRM 614, BHVO-2G, BHVO-2, BCR-2G, JB-2, WS-E, W-2, AGV-1 and AGV-2: Geostandards and Geoanalytical Research, v. 28, no. 3, p. 417-429.

Kruse, F. A., and Hauff, P. L., 1991, Identification of illite polytype zoning in disseminated gold deposits using reflectance spectroscopy and X-ray diffraction-potential for mapping with imaging spectrometers: Geoscience and Remote Sensing, IEEE Transactions on, v. 29, no. 1, p. 101-104.

Le Gleuher, M., Anand, R. R., Eggleton, R. A., and Radford, N., 2008, Mineral hosts for gold and trace metals in regolith at Boddington gold deposit and Scuddles massive copper-zinc sulphide deposit, Western Australia: an LA-ICP-MS study: Geochemistry: Exploration, Environment, Analysis, v. 8, no. 2, p. 157.

Lipske, J., 2002, Advanced argillic and sericitic alteration in the Buckskin Range, Nevada: a product of ascending magmatic fluids from the deeper yerington porphyry copper environment [M.S.: Oregon State University.

Lipske, J., and Dilles, J., 2000, Advanced argillic and sericitic alteration in the subvolcanic environment of Yerington Porphyry Copper System, Buckskin Range, Nevada: Part I. Contrasting Styles of Intrusion-Associated Hydrothermal Systems, v. 32, p. 91-99.

Lowell, J., and Guilbert, J., 1970, Lateral and vertical alteration-mineral zoning in porphyry ore deposits: Economic Geology, v. 65, no. 4, p. 373-408.

Martinez-Alonso, S., 2000, Study of the infrared spectra of phyllosilicates through direct measurements, quantum mechanical modeling, and analysis of AVIRIS imaging spectrometer data: Relationships with environment of mineralization [PhD: University of Colorado, 1-232 p.

Merry, N., and Pontual, S., 1999, Rapid alteration mapping using portable infrared spectrometers: PACRIM '99 Bali, Indonesia, p. 693-698.

Meyer, C., and Hemley, J. J., 1967, Wall Rock Alteration: Geochemistry of Hydrothermal Ore Deposits (Book), p. 166-235.

Newman, A., 1987, Chemistry of Clays and Clay Minerals, New York, John Wiley & Sons, Mineralogical Society Monograph.

Paulick, H., and Bach, W., 2006, Phyllosilicate alteration mineral assemblages in the active subsea-floor Pacmanus hydrothermal system, Papua New Guinea, ODP Leg 193: Economic Geology, v. 101, no. 3, p. 633.

Pontual, S., Merry, N., and Cocks, T., 1995, Field-based alteration mapping using the PIMA: PACRIM Congress 1995 : Auckland, New Zealand, 19-22 November 1995 : proceedings of the 1995 PACRIM Congress.

Post, J. L., and Noble, P. N., 1993, The near-infrared combination band frequencies of dioctahedral smectites, micas, and illites: Clay Clay Miner, v. 41, p. 639-639.

Pouchou, L. J., and Pichoir, F., 1984, New model quantitative x-ray microanalysis, Application to the analysis of homogeneous samples: Research in Aerospace, v. 3, p. 13-38.

Proffett, J., 1977, Cenozoic geology of the Yerington District, Nevada, and implications for nature and origin of Basin and Range faulting: Geological Society of America Bulletin, v. 88, no. 2, p. 247-266.

-, 1979, Ore deposits of the western United States: a summary: Nevada Bureau of Mines, IAGOD 5th Quadrennial Symposium, Geology Report 33, Proceedings, v. 11, p. 13-32.

Proffett, J. M., and Dilles, J. D., 1984, Geologic map of the Yerington District, Nevada, Nevada Bureau of Mines and Geology.

Rose, A. W., 1970, Zonal relations of wallrock alteration and sulfide distribution at porphyry copper deposits: Economic Geology, v. 65, no. 8, p. 920.

Seedorff, E., Dilles, J. H., Proffett, J. M., Jr., Einaudi, M. T., Zurcher, L., Stavast, W. J. A., Johnson, D. A., and Barton, M. D., 2005, Porphyry deposits; characteristics and origin of hypogene features: Economic Geology 100th Anniversary Volume, p. 251-298.

Serratosa, J. M., and Bradley, W. F., 1958, Determination of the orientation of OH bond axes in layer silicates by infrared absorption: The Journal of Physical Chemistry, v. 62, no. 10, p. 1164-1167.

Shaw, D. M., 1952, The geochemistry of thallium: Geochimica et cosmochimica acta, v. 2, no. 2, p. 118-154.

Stubican, V., and Rustum, R., 1961, Isomorphous substitution and infra-red spectra of the layer lattice silicates: American Mineralogist, v. 46, p. 32-51.

Sun, Y., Seccombe, P. K., and Yang, K., 2001, Application of short-wave infrared spectroscopy to define alteration zones associated with the Elura zinc-lead-silver deposit, NSW, Australia: Journal of Geochemical Exploration, v. 73, no. 1, p. 11-26.

Swayze, G. A., 1997, The hydrothermal and structural history of the Cuprite mining district, southwestern Nevada; an integrated geological and geophysical approach [Doctoral: University of Colorado, Boulder.

Thompson, A. J. B., Hauff, P. L., and Robitaille, A. J., 1999, Alteration Mapping in Exploration: Application of Short-Wave Infrared (SWIR) Spectroscopy: SEG Newsletter, v. 39, p. 1-13.

Tschermak, G., 1890, Die chloritgruppe, I. Theil, Sitzungsber.: Akad. Wiss. Wien, Math-naturwiss, Kl., v. 1, no. 99, p. 174-278.

-, 1891, Die chloritgruppe, II. Theil, Sitzungsber.: Akad. Wiss. Wien, Math-naturwiss, Kl., v. 1, no. 100, p. 29-107.

Tuddenham, W., and Lyon, R., 1960, Infrared techniques in the identification and measurement of minerals: Analytical Chemistry, v. 32, no. 12, p. 1630-1634.

Van Lichtervelde, M., Gregoire, M., Linnen, R. L., Beziat, D., and Salvi, S., 2008, Trace element geochemistry by laser ablation ICP-MS of micas associated with Ta mineralization in the Tanco pegmatite, Manitoba, Canada: Contributions to Mineralogy and Petrology, v. 155, no. 6, p. 791-806.

Vedder, W., 1964, Correlations between infrared spectrum and chemical composition of mica: The American Mineralogist, v. 49, no. May-June, p. 736-768.

Vedder, W., and McDonald, R., 1963, Vibrations of the OH ions in muscovite: The Journal of Chemical Physics, v. 38, p. 1583.

Wedepohl, K., 1978, Handbook of Geochemistry, New York, Springer.

Yang, K., Browne, P., Huntington, J., and WALSHE, J., 2001, Characterising the hydrothermal alteration of the Broadlands-Ohaaki geothermal system, New Zealand, using short-wave infrared spectroscopy: Journal of Volcanology and geothermal research, v. 106, no. 1-2, p. 53-65.

Appendices

Appendix A. Sample coordinates, lithology and mineralogy

Table A1. Sample locations, lithologies and mineral assemblages

Sample #	N (NAD 83 11N)	E (NAD 83 11N)	Fault Block	Lithology	Alteration Type
H437113	300315	4320066	Blue Hill	Granite Porphyry	advanced argillic
YD02-02	300891	4320971	Blue Hill	Artesia Lake Andesite Lava	advanced argillic
YD08-19C	300777	4320734	Blue Hill	Artesia Lake Andesite Lava	advanced argillic
H437199	300818	4321301	Blue Hill	Artesia Lake Andesite Lava	sericitic
YD08-21	300978	4320672	Blue Hill	Artesia Lake Andesite Lava	sericitic
ANN006002.018	303783	4316991	Ann Mason	Granite Porphyry	sericitic
G909173_spot1 (qtz-musc-py vein)	304420	4317368	Ann Mason	Granite Porphyry	sericitic
YD09-06	301352	4319674	Blue Hill	Granite Porphyry	sericitic
ANN007006.017	303894	4318135	Ann Mason	Granite Porphyry	sericitic-chloritic
99017 (Bu-647)	296680	4321435	Central Buckskin	Granite Porphyry	sericitic-chloritic
G909165	300499	4320017	Blue Hill	Artesia Lake Andesite Lava	sericitic-chloritic
YD01-13A	300564	4321569	Blue Hill	Artesia Lake Andesite Lava	sericitic-chloritic
YD08-22	301133	4320383	Blue Hill	Mafic Dike	sericitic-chloritic
YTD 23 2008	295940	4322101	Central Buckskin	Granite Porphyry	sericitic-chloritic
H437269	302537	4317593	Ann Mason	McLeod Quartz Monzodiorite	sericitic-chloritic
G909152	301931	4319654	Blue Hill	Granite Porphyry	weak sericitic
G909154	302069	4319314	Blue Hill	Granite Porphyry	weak sericitic
G909155_spot1	301675	4319397	Blue Hill	Granite Porphyry	weak sericitic
G909160	301050	4320041	Blue Hill	Granite Porphyry	weak sericitic
G909173_spot2 (vein selvage)	304420	4317368	Ann Mason	Granite Porphyry	weak sericitic
G909173_spot3 (outside vein selvage)	304420	4317368	Ann Mason	Granite Porphyry	weak sericitic
G909176	304326	4317165	Ann Mason	Granite Porphyry	weak sericitic
G909153	301685	4319773	Blue Hill	Granite Porphyry	illitic
G909155_spot2 (illite veinlet)	301675	4319397	Blue Hill	Granite Porphyry	illitic
G909157	301328	4320041	Blue Hill	Granite Porphyry	illitic
G909163	300660	4319941	Blue Hill	Granite Porphyry	illitic
G909158	301314	4320019	Blue Hill	Granite Porphyry	illitic-chloritic
YD09-04	301347	4319629	Blue Hill	Granite Porphyry	illitic-chloritic
80JD-94D	301829	4321752	Blue Hill	Granite Porphyry	propylitic
81JD-94B	301497	4322150	Blue Hill	Bear Quartz Monzonite	propylitic
ANN006001.045	304289	4317634	Ann Mason	McLeod Quartz Monzodiorite	propylitic
ANN006002.023	303769	4316936	Ann Mason	McLeod Quartz Monzodiorite	propylitic
ANN007006.057	303727	4318264	Ann Mason	McLeod Quartz Monzodiorite	propylitic
G909166	300478	4319976	Blue Hill	McLeod Quartz Monzodiorite	propylitic
G909168	300982	4320120	Blue Hill	Granite Porphyry	propylitic
G909172	304437	4317344	Ann Mason	McLeod Quartz Monzodiorite	propylitic
G909174	304333	4316786	Ann Mason	McLeod Quartz Monzodiorite	propylitic
Y-727	302279	4315589	Ann Mason	McLeod Quartz Monzodiorite	propylitic
YD01-01C	301375	4322336	Blue Hill	Bear Quartz Monzonite	propylitic
YD01-04	301316	4322544	Blue Hill	Bear Quartz Monzonite	propylitic

Table A1. Sample locations, lithologies and mineral assemblages (continued)

Sample #	Added Minerals*	Relic Minerals	Minerals Analyzed	White mica classification	Main Fe trace phase
H437113	Pyroph+Qtz(+Py)		Ser	pyrophyllite	Py
YD02-02	Musc+Pa+Alun+Qtz(+Rt+Py)		Ser	muscovite-paragonite	Py
YD08-19C	Musc+Qtz+Pyroph(+Rt+Py)		Ser	muscovite	Py
H437199	Musc+Pa+Qtz(+Py+Rt)		Ser	Na-illite	Py
YD08-21	Qtz+Musc(+Rt+Py)		Ser	muscovite	Py
ANN006002.018	Musc+Qtz(+Tm+Py+Cp+Rt)		Ser	muscovite	Py(+Cp)
G909173_spot1 (qtz-musc-py vein)	Qtz+Musc(+Tm+Py+Rt)		Ser	muscovite	Py(+Cp)
YD09-06	Qtz+Musc(+Tm+Py+Rt)		Ser	muscovite	Py(+Cp)
ANN007006.017	Chl+Musc+Qtz+Calc(+Py+Rt)	Ab+Ksp+Biot(+Sph)	Chl+Ser	phengitic muscovite	Py
99017 (Bu-647)	Chl+Musc+Qtz(+Hem+Rt)	Ab+Ksp+Biot(+Mgt+Sph)	Chl+Ser	phengitic muscovite	Spec Hem
G909165	Chl+Ser+Qtz(+Hem+Rt)	(+Mgt+Sph)	Chl	-	trace Hem+Mag
YD01-13A	Chl+Musc+Qtz(+Hem+Rt)	(+Mgt+Sph)	Chl+Ser	phengitic muscovite	Spec Hem
YD08-22	Chl+Musc+Calc(+Hem+Py+Rt)	Ab(+Mgt+Sph)	Chl+Ser	phengitic muscovite	trace Hem+Mag
YTD 23 2008	Qtz+Chl+Ser(+Hem+Rt)	Ab+Ksp+Biot(+Mgt+Sph)	Chl	-	Spec Hem
H437269	Chl+Ab+Ser(+Hem+Py)	Olg/And+Ksp(+Sph+Mgt)	Chl	-	trace Hem+Py
G909152	Musc+Ill(+Py+Rt)	Ab+Ksp	Ser	illite	Py
G909154	Musc(+Py+Rt+Cp)	Ab+Ksp	Ser	low-K muscovite	Py(+Cp)
G909155_spot1	Musc(+Py+Rt)	Ab+Ksp	Ser	low-K muscovite	Py
G909160	Musc(+Py+Rt)	Ab	Ser	low-K muscovite	Py
G909173_spot2 (vein selvage)	Musc(+Py+Tm+Rt)	Ab+Ksp	Ser	muscovite	Py
G909173_spot3 (outside vein selvage)	Musc(+Py+Rt)	Ab+Ksp	Ser	phengitic muscovite	Py
G909176	Musc(+Py+Rt)	Ab+Ksp(+Sph)	Ser	muscovite	Py
G909153	Ill(+Py+Rt)	Ab+Ksp	Ser	illite	Py
G909155_spot2 (illite veinlet)	Ill(+Py+Rt)	Ab+Ksp	Ser	illite	Py
G909157	Ill(+Py+Rt)	Ab+Ksp(+Sph)	Ser	illite	Py
G909163	Ill(+Py+Rt)	Ab+Ksp(+Sph)	Ser	illite	Py
G909158	Chl+Ill(+Py+Rt)	Ab+Ksp+Epid(+Sph)	Chl+Ser	illite	Py
YD09-04	Chl+Ser(+Py+Rt)	Ab+Ksp+Epid+Biot(+Sph)	Chl	-	Py
80JD-94D	Chl+Epid(+Ser+Rt)	Olg/And+Ksp+Biot(+Sph+Mgt)	Chl	-	trace Hem+Mag
81JD-94B	Chl+Epid(+Hem+Ser+Rt)	Olg/And+Ksp(+Sph+Mgt)	Chl	-	trace Hem+Mag
ANN006001.045	Chl(+Py+Cp+Rt)	Olg/And+Ksp+Biot+Biot(+Sph+Mgt)	Chl	-	Py(+Cp)
ANN006002.023	Act+Chl(+Ser+Py+Rt)	Olg/And+Ksp+Biot(+Sph+Mgt)	Chl	-	Mag
ANN007006.057	Act+Chl(+Ser+Py+Cp+Rt)	Olg/And+Ksp+Biot(+Sph+Mgt)	Chl	-	Py(+Cp)
G909166	Act+Chl(+Ser+Rt+Py)	Olg/And+Ksp(+Sph+Mgt)	Chl	-	Mag
G909168	Epid+Chl(+Py+Rt)	Olg/And+Ksp+Biot+Biot(+Sph+Mgt)	Chl	-	trace Hem+Mag
G909172	Act+Chl+Epid(+Rt+Hem)	Olg/And+Ksp+Biot(+Sph+Mgt)	Chl	-	Mag
G909174	Act+Epid+Chl+Ab(+Hem+Rt)	Ab+Biot(+Mgt+Sph)	Chl	-	Mag
Y-727	Act+Chl(+Hem)	Olg/And+Ksp+Biot(+Sph+Mgt)	Chl	-	Mag
YD01-01C	Chl+Ab+Epid(+Ser+Rt+Py+Hem)	Olg/And+Ksp(+Sph+Mgt)	Chl	-	trace Hem+Mag
YD01-04	Chl+Epid+Act+Ab(+Hem+Py)	Olg/And+Ksp+Biot(+Sph+Mgt)	Chl	-	trace Hem+Mag

*Mineral abbreviations are available in Table 2.1 *The term sericite (Ser) refers to white mica or clay of unknown composition

Appendix B. Methods

Table B1. Limits of Detection (LOD) and Standards for EMP analysis

Major Oxide	Standard*	LOD** (ppm)	LOD (% oxide)
SiO2	Flourophlogopite (FLOG-1)	210	0.04
TiO2	Basalt glass (BASL)	140	0.02
Al2O3	Labradorite (LABR)	190	0.07
FeO	Olivine (FO83)	520	0.07
MnO	Pyroxmangite (PYMN)	450	0.06
MgO	Augite (KAUG)	160	0.03
V2O3	Vanadanite (VANA)	260	0.08
CaO	Augite (KAUG)	150	0.02
Na2O	Labradorite (LABR)	180	0.05
K2O	Flourophlogopite (FLOG-1)	240	0.06
P2O5	Apatite (FLAP)	140	0.13
SO2	Chalcopyrite (CHAL)	160	0.02
F	Flourophlogopite (FLOG-1)	1300	0.06
Cl	Tugtupite (TUGT)	150	0.03

*standards from Smithsonian (USMN) and Astimec
**average limit of detection calculated by EMP anlaysis software (n=781)

Table B2. EMP Analytical Accuracy and Precision measured using FLOG-1 standard

Major Oxide	Flourophlogopite (FLOG-1) standard	Overall Mean (n=33)	1 standard deviation (σ) (%)	Accuracy (%)
SiO_2	42.79	42.85	1.13	0.13
TiO_2		BDL		
Al_2O_3	12.1	12.31	6.04	1.75
FeO		BDL		
MnO		BDL		
MgO	28.7	28.91	3.51	0.75
V_2O_3		BDL		
CaO		BDL		
Na_2O		BDL		
K_2O	11.18	11.08	0.94	0.92
P_2O_5		BDL		
SO_2		BDL		
F	9.02	8.91	4.53	1.21
Cl		BDL		

Table B3. Limits of detection for standards used in LA-ICP-MS calculated using method by Perkins and Pearce (1995).

Isotope (ppm)	GSE-1G-5 (n=10)		GSD-1G-2(n=2)		NIST-610-2 (n=4)		NIST-612-7 (n=6)	
	mean	1σ	mean	1σ	mean	1σ	mean	1σ
7Li	0.20	0.08	0.193	0.02	0.24	0.02	0.17	0.05
11B	0.26	0.16	0.24	0.03	0.41	0.04	0.28	0.10
29Si	43	22	37.21	8.07	53	1.3	35	16
31P	1.35	0.65	0.85	0.09	1.85	0.05	0.89	0.45
45Sc	0.17	0.12	0.15	0.01	0.20	0.008	0.13	0.07
47Ti	0.63	0.35	0.53	0.02	0.56	0.14	0.53	0.25
51V	0.05	0.04	0.03	0.01	0.05	0.01	0.03	0.02
52Cr	0.42	0.38	0.21	0.01	0.69	0.02	0.24	0.14
55Mn	0.12	0.09	0.08	0.009	0.18	0.01	0.10	0.06
59Co	0.09	0.06	0.05	0.005	0.12	0.01	0.07	0.04
63Cu	0.26	0.21	0.22	0.09	0.39	0.03	0.19	0.14
65Cu	0.26	0.17	0.29	0.12	0.31	0.03	0.18	0.11
66Zn	0.14	0.14	0.11	0.01	0.23	0.03	0.12	0.07
68Zn	0.31	0.28	0.22	0.03	0.48	0.05	0.24	0.15
75As	0.17	0.12	0.11	0.01	0.33	0.03	0.20	0.10
76Se	0.10	0.02	0.01	0.0003	0.66	0.005	-	-
77Se	0.58	0.38	0.18	0.002	0.91	0.02	-	-
85Rb	0.06	0.04	0.04	0.005	0.07	0.01	0.04	0.02
88Sr	0.04	0.05	0.04	0.02	0.05	0.01	0.03	0.02
95Mo	0.10	0.11	0.05	0.008	0.16	0.02	0.08	0.05
118Sn	0.07	0.07	0.05	0.004	0.12	0.004	0.08	0.05
125Te	0.17	0.24	0.06	0.002	0.31	0.13	0.11	0.09
133Cs	0.04	0.03	0.03	0.003	0.05	0.008	0.04	0.02
137Ba	0.16	0.15	0.10	0.01	0.22	0.04	0.15	0.11
138Ba	0.03	0.04	0.02	0.008	0.04	0.02	0.02	0.01
182W	0.05	0.08	0.02	0.001	0.07	0.02	0.03	0.02
208Pb	0.03	0.06	0.01	0.0004	0.06	0.02	0.02	0.02
209Bi	0.02	0.03	0.005	0.001	0.03	0.01	0.01	0.01
232Th	0.91	1.81	0.008	0.0005	0.14	0.05	0.02	0.02
238U	0.005	0.002	0.006	0.002	-	-	0.005	0.002
205Tl	0.004	0.002	0.004	0.0004	-	-	0.003	0.001

Table B4. Upper and lower limits of detection (LOD) for ICP-MS/AES (ALS Chemex method ME-MS61).

Element	lower LOD	upper LOD	Element	lower LOD	upper LOD
Ag (ppm)	0.01	100	Na (%)	0.01	10
Al (%)	0.01	50	Nb (ppm)	0.1	500
As (ppm)	0.2	10000	Ni (ppm)	0.2	10000
Ba (ppm)	10	10000	P (ppm)	10	10000
Be (ppm)	0.05	1000	Pb (ppm)	0.5	10000
Bi (ppm)	0.01	10000	Rb (ppm)	0.1	10000
Ca (%)	0.01	50	Re (ppm)	0.002	50
Cd (ppm)	0.02	1000	S (%)	0.01	10
Ce (ppm)	0.01	500	Sb (ppm)	0.05	10000
Co (ppm)	0.1	10000	Sc (ppm)	0.1	10000
Cr (ppm)	1	10000	Se (ppm)	1	1000
Cs (ppm)	0.05	500	Sn (ppm)	0.2	500
Cu (ppm)	0.2	10000	Sr (ppm)	0.2	10000
Fe (%)	0.01	50	Ta (ppm)	0.05	100
Ga (ppm)	0.05	10000	Te (ppm)	0.05	500
Ge (ppm)	0.05	500	Th (ppm)	0.2	10000
Hf (ppm)	0.1	500	Ti (%)	0.005	10
In (ppm)	0.005	500	Tl (ppm)	0.02	10000
K (%)	0.01	10	U (ppm)	0.1	10000
La (ppm)	0.5	10000	V (ppm)	1	10000
Li (ppm)	0.2	10000	W (ppm)	0.1	10000
Mg (%)	0.01	50	Y (ppm)	0.1	500
Mn (ppm)	5	100000	Zn (ppm)	2	10000
Mo (ppm)	0.05	10000	Zr (ppm)	0.5	500

Appendix C. Example of Trench Mapping

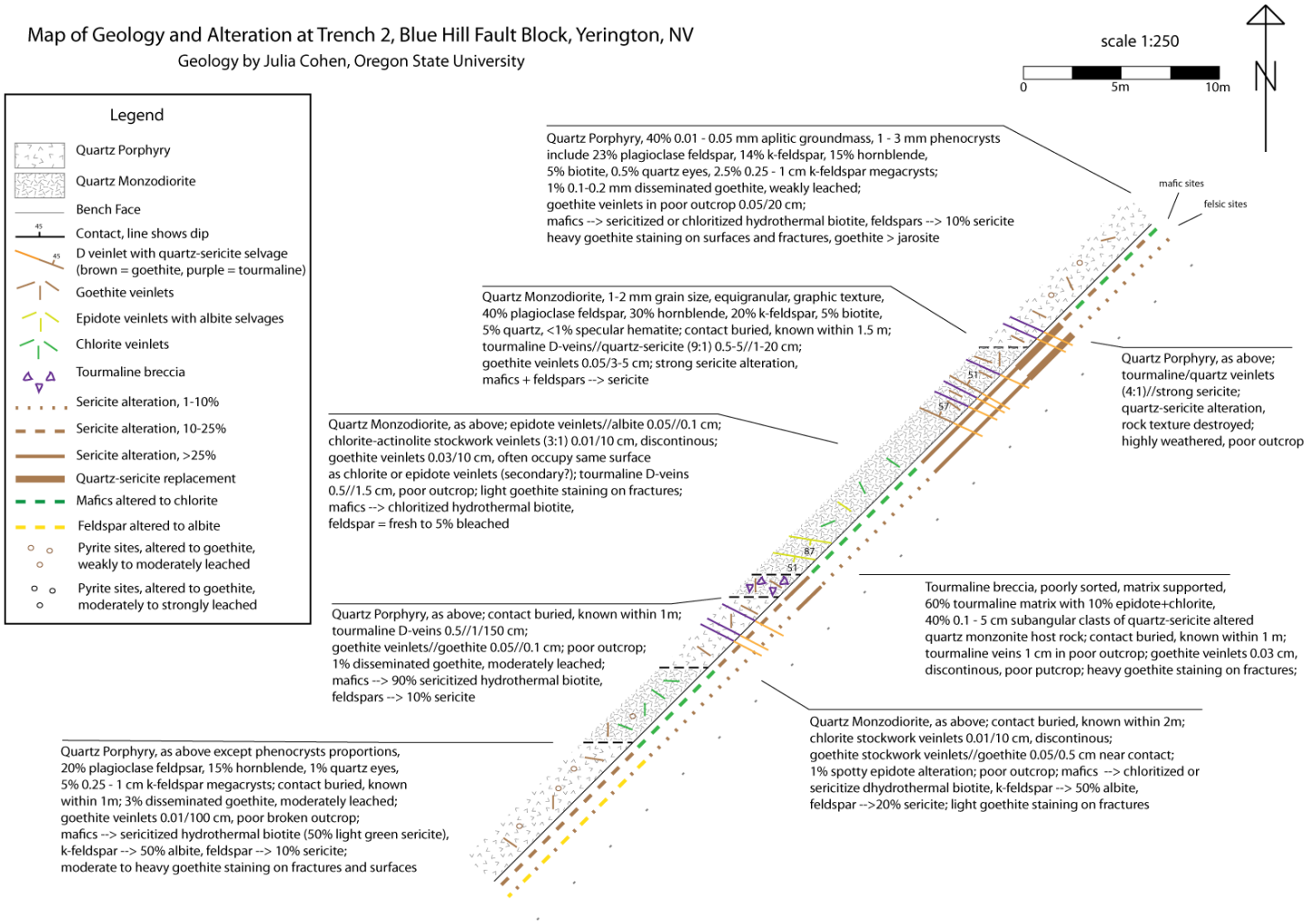

Figure C1. Digitalized trench map. Trench mapping was done using the Anaconda method (Einaudi, 1977).